Department of Precision and Microsystems Engineering

Feasibility of Using Si_3N_4 and SiC for LVFs: Comparison of a FEM Membrane Model with Experiments

Sanghati Roy

Report no	: 2024.067
Coach	: Dr.Nandini Bhattacharya
Professor	: Dr.Nandini Bhattacharya, Dr.ir.Willem Jellema, Ing.Martin Eggens, Dr.Andres Hunt
Specialisation	: Mechatronics System Design
Type of report	: MSc Thesis Report
Date	: 15-08-2024

TU Delft Delft University of Technology

Challenge the future

Feasibility of Using Si_3N_4 and SiC for LVFs: Comparison of a FEM Membrane Model with Experiments

by

Sanghati Roy

Student Name	Student Number
Sanghati Roy	5683602

Committee:	Dr. Nandini Bhattacharya,
	Dr.ir. Willem Jellema, SRON
	Ing. Martin Eggens, SRON
	Dr. Andres Hunt
Project Duration:	July, 2023 - August, 2024
Faculty:	Faculty of Mechanical Engineering, Delft

TUDelft

Acknowledgements

The year I spent working on my thesis has been quite challenging and rewarding at the same time. Apart from learning new theories and technologies, it has opened my eyes to the potential of space-borne optical instrumentation.

The success of this MSc Thesis project is attributed to my supervisors Nandini Bhattacharya from TU Delft, Willem Jellema and Martin Eggens, from SRON. Martin constantly allocated time to assist me in various aspects of the project. Additionally, Nandini's enthusiasm and positivity helped maintain my motivation. I would further like to extend my gratitude towards my colleagues at the Optics lab, for their timely insights and assistance. Without them, operating the Lynceetec would have been impossible. Lastly, I would like to thank Eveline Matroos, the track coordinator of High-Tech Engineering for making day-to-day processes seamless.

I would also like to thank my parents for their unconditional love and support. They've consistently helped me tread the path of knowledge and wisdom and I stand grateful. Huge thanks to my partner Maarten for his unflinching support and for making me see the light on the darkest of days. Thanks to all my high-tech friends, my housemates and Rick, they've constantly uplifted my morale and helped me get through the tough times. I would like to end with a memorable quote from my father:

গুম্পু বাড়ি এসো।
মায়ের সাথে জমিয়ে সি ডি পি এইচ করব।

Sanghati Roy
Delft, August 2024

Abstract

Linear Variable Filters (LVFs) are integral to future space missions aimed at measuring the spectral features of distant galaxies. Given the varying red-shifts (shift of light to longer wavelengths as an object moves away from the observer) of these galaxies, an LVF with a resolving power of approximately 10 can effectively identify, classify, and image large populations of galaxies, facilitating studies of cosmic evolution through hyperspectral imaging (HSI) techniques. HSI captures detailed spectral information across a wide range of wavelengths for each pixel in an image, enabling material identification and analysis. Since the galaxies to be studied are very faint, hyperspectral imagers need to be equipped with highly sensitive detectors, cryogenically cooled conditions, and filters with high transmission efficiency. This thesis investigates LVFs based on thin membranes, focusing on materials like silicon nitride (Si_3N_4) and silicon carbide (SiC). The primary objective is to model these thin and pre-stressed membranes using COMSOL Multiphysics to simulate the thermal expansion and mechanical behaviour of membranes in cryogenic environments. Experimental validation is conducted using Digital Holography Microscopy (DHM) and Laser Doppler Vibrometry (LDV) to ensure the accuracy and consistency of the simulations. The model enables the simulation of membranes with varying dimensions, improving the accuracy of behavioural predictions thereby eliminating the need for physical prototypes for analytical purposes, significantly reducing cost and time. Overall, this research bridges the gap between theoretical models and practical applications of LVFs in space. Enhancing the understanding of material behaviour under extreme conditions advances the development of reliable LVFs for spaceborne optical instruments, offering valuable insights into their durability and performance.

Contents

Nomenclature

List of abbreviations

Abbreviation	Definition
ALMA	Atacama Large Millimeter/submillimeter Array
AGN	Active Galactic Nuclei
BHAR	Black Hole Accretion Rates
CCD	Charge-Coupled Device
CTE	Coefficients of Thermal Expansion
DHM	Digital Holographic Microscopy
EoR	Epoch of Reionisation
FEM	Finite Element Method
FSS	Frequency-Selective Surfaces
HSI	Hyperspectral Imaging
IR	Infrared
JWST	James Webb Space Telescope
LDV	Laser Doppler Vibrometer
LVFs	Linear Variable Filters
MEMS	Microelectromechanical Systems
NLR	Netherlands Aerospace Centre
PRIMA	Probe Far Infrared Mission for Astrophysics
SFR	Star-Formation Rates
SMBH	Supermassive Black Holes
SRON	Space Research Organisation Netherlands
Si	Silicon
SiC	Silicon Carbide
Si_3N_4	Silicon Nitride
TES	Transition-Edge Sensors

1 Introduction

1.1. Overview of Spectral Imaging in Space Missions

Hyperspectral imaging extends our capacity to explore space by capturing light across a broad range of wavelengths, providing rich, detailed spectral information. The PRIMA (Probe Far Infrared Mission for Astrophysics) mission, led by NASA with contributions from SRON (Space Research Organisation Netherlands), aims to leverage hyperspectral imaging to study the far-infrared spectrum, specifically from 24 μm to 235 μm. The goal is accomplished through a wideband spectrometer and a multi-band spectrophotometric imager PRIMAger, a hyperspectral camera as shown in Fig 1.1).

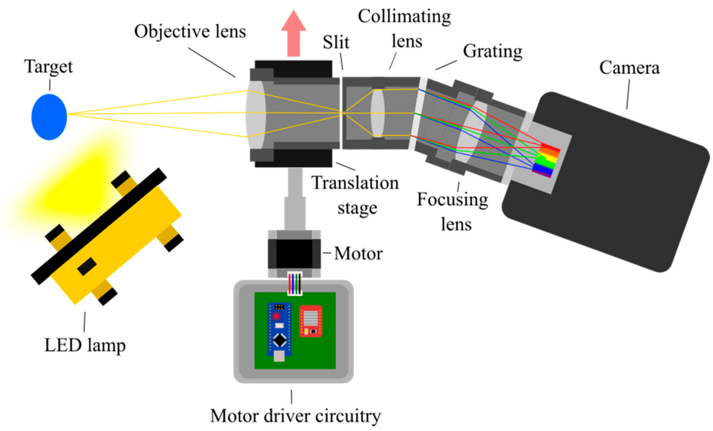

Figure 1.1: Schematic diagram of a hyperspectral imager

1.1.1. Integration with ALMA and JWST

The PRIMA mission is positioned to enhance the capabilities of two of the most advanced astronomical observatories in operation: the Atacama Large Millimeter/submillimeter Array (ALMA) and the James Webb Space Telescope (JWST). Each of these observatories plays a role in our understanding of the universe, and by bridging the gap between them, PRIMA aims to provide a more complete picture of the cosmos as shown in Fig 1.2.

- **ALMA (Atacama Large Millimeter/submillimeter Array)** focuses on the millimetre and submillimeter wavelengths, which are ideal for studying the coldest objects in space, such as molecular clouds, proto-planetary disks, and the early stages of star formation. ALMA's high resolution and sensitivity allow it to image the fine details of stellar birth and complex chemical interactions. However, ALMA's scope is limited to longer wavelengths, missing out on the richer thermal and chemical signatures that appear at shorter far-infrared wavelengths [1]–[4].

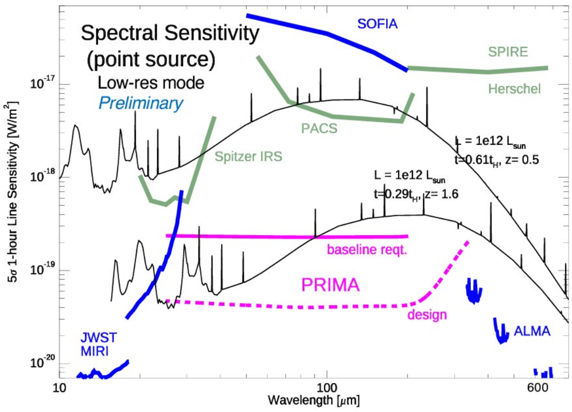

Figure 1.2: Spectral sensitivity for various astronomical instruments

- **JWST (James Webb Space Telescope)** explores a broad range of wavelengths from visible light to mid-infrared, enabling it to study the universe with unprecedented clarity and depth. JWST excels in observing high-redshift galaxies, star-forming regions, and exoplanet atmospheres. Its capabilities allow for detailed spectral analysis of distant objects, but it lacks the specific instrumentation to cover the entire far-infrared spectrum, where many critical cosmic signals reside [5]–[8].

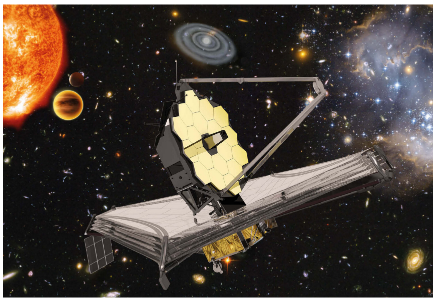

Figure 1.3: The JWST mission

Figure 1.4: The ALMA facility

Recent JWST results have revealed a crucial gap in our understanding of galaxy evolution: the widespread presence of dust and active galactic nuclei (AGN) in the early Universe. PRIMA will address this by conducting large-scale galaxy surveys using PRIMAger, which provides innovative hyperspectral narrow-band and rapid imaging with continuous coverage from 25 to 84 μm. This wavelength range bridges the gap between JWST and ALMA, enabling us to estimate dust-obscured black hole accretion rates and star-formation rates up to the epoch of reionisation through the analysis of far-infrared spectral energy distributions.

PRIMA is uniquely positioned to explore new parameter spaces and revolutionize our understanding of galaxy evolution and planet formation, with its significant sensitivity increase, exclusive wavelength range of 24 to 235 μm accessible only from space, and a dramatic enhancement in mapping speed.

1.1.2. The Importance of Far-Infrared Observations for Galaxy Evolution

Far Infrared observations (FIR) are crucial for answering fundamental questions about the evolution of galaxies and their central supermassive black holes (SMBH). By probing the far-IR spectrum, PRIMA can unveil the hidden processes of galaxy formation and evolution that are obscured by dust in other wavelengths. Here's why FIR is essential:

- **SMBH and Galaxy Co-evolution**: One of PRIMA's primary science goals is to investigate the co-evolution of SMBH and their host galaxies across cosmic time. Understanding this relationship is crucial for advancing our knowledge of galaxy evolution and cosmology, as feedback from SMBHs significantly impacts star formation and galaxy growth.

- **Unique Observational Capabilities**: PRIMA leverages far-infrared (far-IR) galaxy surveys to uniquely identify dust-obscured AGN and directly measure both black hole accretion rates (BHAR) and star-formation rates (SFR). This capability allows scientists to trace the assembly of SMBHs and stars throughout most of cosmic history, including the crucial epoch of reionisation (EoR).
- **Comprehensive Survey Coverage**: PRIMA performs both wide and deep surveys, covering large areas of the sky with unprecedented sensitivity. The wide survey spans 10 square degrees, while the deep survey covers 1 square degree at three times the depth of the wide survey. This extensive coverage enables the detection of a broad range of galaxy types and luminosities, from normal star-forming galaxies to ultra-luminous infrared galaxies, up to high redshifts.
- **Resolving Key Uncertainties**: PRIMA's surveys help resolve major uncertainties in galaxy evolution models by providing a large sample size of hundreds of thousands of galaxies. By measuring the BHAR and SFR in the same galaxy populations, PRIMA offers direct evidence of the relative growth rates of SMBHs and their host galaxies, distinguishing between different theoretical models and simulations.
- **Advantages of Far-IR Observations**: Far-IR observations are particularly suited for studying heavily dust-obscured regions, where the rapid assembly of stellar mass and SMBH mass occurs. PRIMA's hyperspectral imaging and wide wavelength coverage (from 25 to 84 μm) allows it to disentangle the contributions from AGN and star formation, providing a clearer picture of the processes driving galaxy evolution.

1.2. The Role of Linear Variable Filters in PRIMA

To achieve unprecedented spectro-photometric mapping speed in the FIR, the key enabling component will be a Linear Variable Filter (LVF). When an LVF is positioned in front of the detector focal plane, it functions as a position-dependent bandpass filter. This dispersive element segments the camera's field of view into "spectral columns", thereby converting the camera into an instrument capable of multicolour mapping [9]–[11].

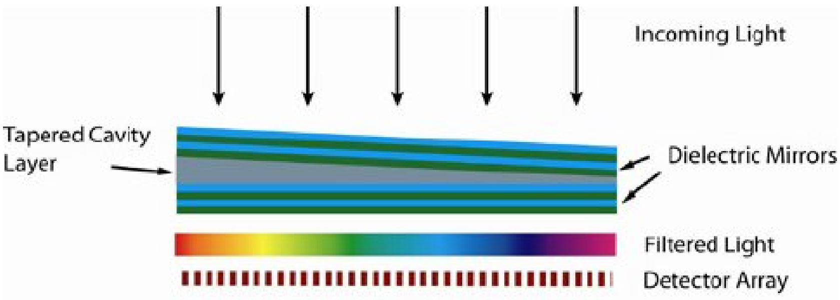

Figure 1.5: A schematic view of a tapered Fabry-Perot type of Linear-variable Optical Filter

1.2.1. Necessity of LVFs

LVFs are widely utilized in both optical and infrared (IR) applications. They are constructed using wedged substrates paired with multi-layer coatings. These coatings vary in thickness along the length of the substrate, allowing LVFs to selectively filter different wavelengths of light at different positions. This unique design enables precise spectral analysis and is particularly advantageous for applications requiring high-resolution spectral data across a broad wavelength range. However, the spectral resolving power of the LVF prototype for PRIMA is around 10, which is a moderate resolution.

The significance of LVFs in FIR observations includes:

- **Critical Wavelength Coverage**: LVFs enable PRIMA to cover the far-IR wavelength range from 25 to 84 μm, which is essential for bridging the observational gap between the JWST and the ALMA.

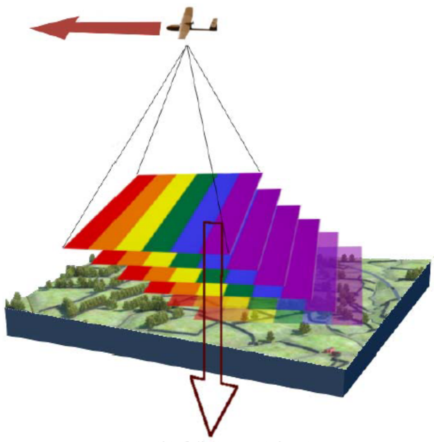

Figure 1.6: Method of acquisition using LVFs

- **Increased Mapping Speed and Sensitivity**: The incorporation of LVFs significantly boosts PRIMA's mapping speed and sensitivity. This enhancement allows PRIMA to conduct large-scale galaxy surveys with unprecedented efficiency.
- **Resolving Redshift-Dependent Phenomena**: LVFs allow PRIMA to explore redshift-dependent phenomena with greater clarity. By capturing data across a wide spectral range, PRIMA can trace the assembly of SMBHs and stellar mass from the early Universe to the present. This capability is essential for distinguishing between different models of galaxy evolution and understanding the interplay between star formation and AGN activity.
- **Overcoming Observational Challenges**: Far-IR observations face unique challenges, such as the need to penetrate thick dust clouds that obscure many astronomical objects. LVFs, with their precise filtering capabilities, enable PRIMA to overcome these challenges, allowing for detailed studies of both the dust-enshrouded regions where rapid stellar and SMBH growth occurs and the overall structure of galaxies across cosmic history.

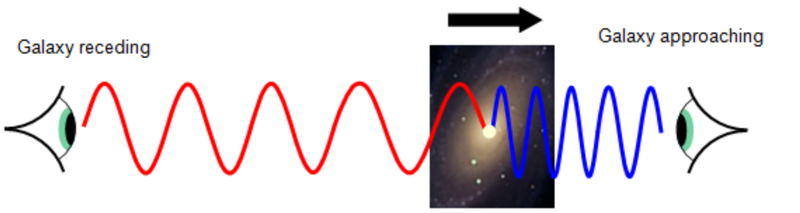

Figure 1.7: Red shift in the universe

1.2.2. Role of a Membrane in LVFs

At the heart of an LVF is a thin membrane. The membrane must be exceptionally flat and stable to ensure uniform optical properties across the LVF. Any irregularities or deformations can lead to distortions in the transmitted light, affecting the filter's spectral performance. It must also have a high transmission in the FIR range. Apart from this, the membrane needs to withstand the mechanical stresses involved in both the fabrication process and during operation. It must have a low CTE (coefficient of thermal expansion) to maintain its shape and size across varying temperatures. Efficient heat dissipation is necessary to prevent thermal distortions that could affect the filter's performance.

Integrating resonant metal mesh structures into super-thin membranes has long been a classical method for maintaining optical performance under harsh conditions. The design parameters, such as mesh-element dimensions and periodicity, determine the resonant frequencies, making them highly selective and efficient for specific wavelengths. The capacitive and inductive properties of these metal meshes form a resonant LC circuit, with capacitive grids performing low-pass operations and inductive grids performing high-pass operations. While the PRIMAger LVF will incorporate this technology, it is presented here as a recommendation for future work in my thesis [12]–[18].

1.2.3. Membrane Materials

Having established the stringent qualifications required for membranes to be suitable for an LVF application, the material properties that need to be fulfilled and available materials are discussed.

- **Precision and Stability:** The mechanical strength and thermal stability need to be ensured so that the LVF maintains its precise optical characteristics over a wide range of operating conditions.
- **Durability and Longevity:** The chemical resistance and durability of these materials extend the operational lifespan of the LVF, reducing maintenance and replacement costs.
- **Optical Performance**: High optical transparency, particularly in the infrared range, is crucial for the LVF to perform effectively with minimal signal loss. The membranes need to be manufactured to very thin limits for optimal optical performance and must be pre-stressed for high-frequency applications to maintain stability and precision.

High-performing advanced ceramic materials like alumina (Al_2O_3), zirconia (ZrO_2), silicon carbide (SiC), aluminum nitride (AlN), silicon nitride (Si_3N_4) fit most of our requirements. Among various candidates, Si_3N_4 and SiC stand out due to their combination of properties which make them well-suited for demanding applications.

The process of making Si_3N_4 membranes is highly standardized and has a set lithographic technique. During fabrication, the membrane is stretched like a drum. This stretched condition helps in maintaining a very flat membrane, which is crucial for the desired optical performance.

The ultimate tensile strength of SiC is much stronger than Si_3N_4, potentially allowing for the production of thinner membranes. Thinner membranes result in higher optical properties (reduced losses, increased transmission), which is beneficial for the overall performance of the device.

Si_3N_4: Heritage and Initial Trials

Si_3N_4 has been crucial in developing MEMS technology, prized for its mechanical robustness, thermal stability, and exceptional dielectric properties. Its versatility spans various high-tech fields, from MEMS devices to photonic circuits, where it serves as a diffusion barrier against contamination and enhances the durability of semiconductor devices [19]. The physical properties of Si_3N_4 thin films, namely low tensile stress, low thermal/electrical conductance, and its overall compatibility with other common materials have facilitated its use in the microfabrication of structures requiring mechanical support, thermal isolation, and low-loss microwave signal propagation

- **Pioneering Applications in MEMS**: Since the early 1980s, Si_3N_4 has been instrumental in creating reliable and durable MEMS devices. Its resistance to oxidation and corrosion under harsh conditions ensures the long-term durability of MEMS components. Additionally, Si_3N_4 films are typically deposited using a low-pressure chemical-vapor-deposition (LP-CVD) process optimized for low tensile stress (< 100 MPa) and a high optical index (> 2), which contributes to their reliability and performance in MEMS applications.
- **Role in Terahertz Detectors**: At institutions like SRON, Si_3N_4 is used in transition-edge sensors (TES) for applications including astronomy. Its low dielectric constant and loss tangent are crucial in minimizing energy losses at high frequencies, enhancing the sensitivity and performance of these detectors [20]–[22]. Transmission measurements of Si_3N_4 samples reveal key features in the far-IR region, with resonance peaks at 12 and 25 THz, making it highly suitable for terahertz detection.
- **Integration with Silicon Processing**: Beyond TES detectors, Si_3N_4 is extensively used in high-performance applications like photonic circuits and waveguides, thanks to its low optical loss at telecom wavelengths. Its robustness and compatibility with silicon processing make it a preferred choice for creating complex, reliable MEMS structures [23]. Furthermore, Si_3N_4 exhibits low

thermal and electrical conductance, making it suitable for applications requiring thermal isolation and low-loss microwave signal propagation. The high tensile strength and compatibility with other materials further enhance its utility in microfabrication and sensor applications.

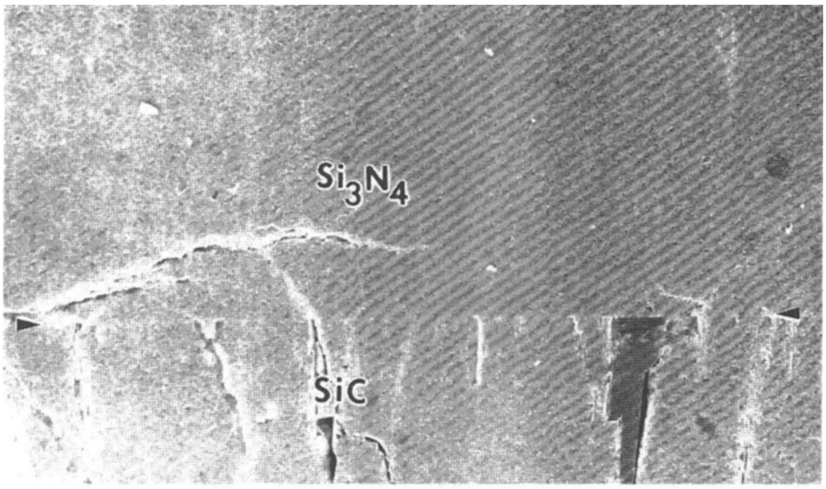

Figure 1.8: Typical cross-sectional SEM image of Si3N4/SiC interface [24]. Cracks in SiC due to its higher thermal expansion coefficient.

Emerging Availability of SiC

SiC is gaining attention as a potential replacement for Si_3N_4 due to its superior thermal conductivity, mechanical strength, and chemical stability. These properties make SiC an attractive alternative for high-performance applications [25]–[28].

Tables 1.1 and 1.2 highlight the merits and limitations of both Si_3N_4 and SiC.

Silicon Nitride (Si_3N_4)
Merits
Optical and Detector Applications Si_3N_4 excels in optical and detector applications due to its high optical transparency, particularly in the infrared range, and low thermal conductivity, making it ideal for thermal isolation in sensors. Its mechanical strength and chemical stability are beneficial for maintaining the structural integrity of thin membranes in LVFs. **Mechanical and Thermal Stability** Si_3N_4 offers excellent mechanical properties and resistance to chemical degradation, which is essential for long-term durability in harsh environments. This stability ensures that LVFs maintain their precise optical characteristics over a wide range of operating conditions.
Limitations
High Dielectric Losses and Fabrication Challenges Si_3N_4 exhibits higher dielectric losses at shorter wavelengths, limiting its effectiveness in high-frequency applications. Additionally, the fabrication of high-purity and structurally sound Si_3N_4 membranes can be complex and costly, which is a significant consideration for precision optical components like LVFs.

Table 1.1: Merits and Limitations of Silicon Nitride (Si_3N_4) in LVF and Detector Applications

Silicon Carbide (SiC)
Merits
High-Power and Detector Applications SiC's superior thermal conductivity and electrical properties make it ideal for high-power electronic applications. Its ability to handle high voltages and temperatures with lower losses is crucial for power electronics, electric vehicles, and renewable energy technologies. Additionally, SiC's mechanical strength allows for thinner membranes, enhancing optical performance in high-frequency applications. **High-Frequency and Signal Integrity** SiC's lower dielectric losses and broader bandwidth make it valuable for maintaining signal integrity at high frequencies, essential for telecommunications and radar applications. Its robustness allows for complex designs necessary for sophisticated high-frequency devices.
Limitations
Cost and Manufacturing Challenges The adoption of SiC is often hindered by its high cost, especially for substrates of the quality required for precision applications. Moreover, the manufacturing processes for creating complex SiC components are still being refined, which can restrict their immediate application in sophisticated designs necessary for advanced optical and electronic devices.

Table 1.2: Merits and Limitations of Silicon Carbide (SiC) in LVF and Detector Applications

Thus due to SiC's superior thermal stability, ability to tackle high voltages and temperatures with lower losses and broader bandwidth, it as a better alternative to Si_3N_4.

1.3. Mechanical Loads and Vibration Transmission in Instruments

usually, optical space instruments like LVFs are situated on the top side of the rocket. The mechanical loads are primarily caused by various factors, including the rocket motor, boosters, lift-off loads, acoustic loads, structural vibration loads, engine transients, wind and turbulence, stage and fairing separation loads, and manoeuvring loads. The capacity to withstand these loads must be ensured by the LVF.

1.3.1. Vibration Transmission Paths

Vibration transmission paths to the scientific instrument include:

- Mechanical transmission through the launcher structure to the spacecraft and then to the scientific instrument.
- Acoustic excitation of mechanical parts of the spacecraft, leading to mechanical transmission to the scientific instrument.
- Direct acoustic excitation of the scientific instrument.

The level of mechanical loads is generally defined in terms of acceleration $[m/s^2]$ or in gravity $[g]$, where $1\,g = 9.81\,m/s^2$. The mechanical loads depend on the applied frequency and are defined for frequency f in Hz $(1/s)$.

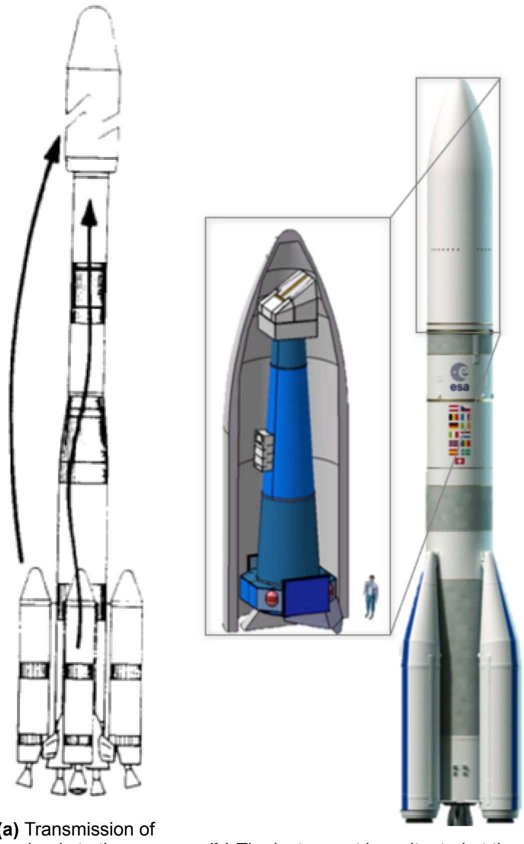

(a) Transmission of loads to the instrument bay

(b) The instrument bay situated at the upper section of the rocket

Figure 1.9: How the LVF in the instrument bay gets affected (sourced from SRON repository)

Overview of Frequency Spectrum

The frequency spectrum, depending on the whole structural system of the instrument, spacecraft, and launcher (rocket), includes:

- **Quasi-Static**: Steady-state accelerations; typically 20 – 100 g
- **Sine**: Rocket and spacecraft dynamic vibrations
  - Low frequency vibrations; typically < 100 Hz; 5 – 20 g
- **Acoustic**: Rocket engine noise transferred through air, impinging on structural panels causing vibrations in the unit
  - Mid to high frequency vibrations; typically < 2000 Hz; 20 - 100 g
- **Shocks**: Separation of rocket stages, fairing, spacecraft from rocket. Deployment of solar arrays and antennas
  - High frequency; typically < 10 kHz; 500 - 10000 g

Eigenfrequency Analysis

The relationship between acceleration a, eigenfrequency ω, and amplitude A is given by:

$$a = \omega^2 \cdot A$$

where a is the acceleration, ω is the angular frequency (eigenfrequency), A is the amplitude of the motion.

Keeping the amplitude low is essential due to space constraints or advanced design needs (like stacked filters). A higher eigenfrequency ω allows for lower amplitude at the same acceleration. Mode shapes from eigenfrequency analysis help understand stress distribution in the membrane, ensuring the structural integrity and performance of the LVF membranes.

1.4. Motivation

The motivation for this research stems from the ambition to develop thin LVF membranes for space-based HSI, specifically targeting FIR spectrum — a frequency range that has not been extensively explored. The aim is to achieve this using silicon nitride (Si_3N_4) membranes.

To date, a comprehensive thermomechanical model for LVF membranes has not been established. As a result, the primary objective is to develop such a model using COMSOL Multiphysics. This model will analyze the eigenfrequencies, mode shapes, and stress distributions of LVF membranes under both room temperature and cryogenic conditions. The aim is to create a robust and accurate simulation that faithfully replicates the physical properties of these membranes. Once this model is developed, it will minimize the reliance on physical prototypes and reduce the need for costly and time-consuming experimental cryogenic testing, offering a more efficient approach to membrane analysis and validation.

The COMSOL model allows for the simulation of membranes with different dimensions and their behaviour is more accurately predicted. The modal characteristics of the model are validated through experimental tests. The feedback from these tests are used to refine and improve the model iteratively. The objective is to achieve a fully functional and reliable model with a high degree of confidence, which can then be used to optimize the design and performance of LVF membranes for FIR HSI applications.

1.5. Project Prototype Objectives

In the final stages of SRON's project, which aims to develop a prototype for PRIMAger, there are specific objectives:

Stacked Membrane Design

The ultimate goal is to have two Si_3N_4 membranes stacked on top of each other with a few microns in between them. Ensuring that these membranes do not touch each other is critical. To achieve this, the operating frequency should be very high, resulting in low-amplitude vibrations that prevent contact.

Maintaining Flatness and Precision

The membranes must be exceptionally flat because the gap between them needs to be within a few microns. This precision is crucial for achieving high optical performance and maintaining the integrity of the device. This reduces absorption and scattering losses, enhancing the overall transparency and efficiency of the optical system.

Future Considerations for Perforations

SRON has included perforations in the membrane, yet a comprehensive thermomechanical model for such a structure has not been developed. These perforations, designed as crosses, will need to be evaluated for their impact on the structural strength and the frequencies of the membranes. It is important to determine if the perforated membranes will be strong enough to withstand operational stresses and if the introduced perforations will alter the natural frequencies of the system. Also, the stiffness of the membrane, altered by the perforations, must be carefully analyzed. Changes in stiffness can affect the overall mechanical and optical properties of the membranes, influencing their performance in the final application.

By addressing these goals and considerations, SRON aims to develop a highly precise, durable, and efficient prototype for PRIMAger that meets the stringent requirements of future astronomical observations.

1.6. Thesis Outline

Chapter 1 gives an overview of spectral imaging in space missions, discusses the integration with ALMA and JWST, and explains the role of LVFs in PRIMA. It also talks about membrane materials and their suitability. It provides a motivation and our research gap. The remaining chapters are structured as follows:

- **Chapter 2: Literature Review** - This chapter provides a brief introduction to the background concepts needed for understanding this research. It provides a comprehensive literature overview of analytical and experimental techniques.
- **Chapter 3: Research Methodology** - This chapter outlines the research design and approach, details the selection and preparation of materials, and describes the experimental setup and procedures.
- **Chapter 4: Simulation Results** - This chapter presents an overview of simulation approaches using COMSOL Multiphysics and thermomechanical modelling. It details the simulation setup and parameters and provides the results of COMSOL simulations.
- **Chapter 5: Measurement Results** - This chapter details the measurement results using LynceeTec DHM R2200 and Polytec PSV-400 Laser Doppler Vibrometer (LDV). It describes the experimental parameters and presents the results of membrane measurements, including frequency response analysis, membrane modes, and deflection measurements.
- **Chapter 6: Conclusion** - This chapter revisits the primary research questions and hypotheses, summarizes the key findings, evaluates the achievements relative to the objectives, acknowledges the limitations, and provides concluding remarks.
- **Chapter 7: Recommendations** - The final chapter offers recommendations for improving the current work and discusses potential future research directions that could build upon this study.

2 Literature preliminaries

Building on the introduction's overview, the following literature review explores the materials, techniques, and methodologies that need to be studied to address these challenges. Material properties, thermo-mechanical characteristics of membranes and finally the measurement techniques have been addressed in this chapter.

2.1. Material as Frames

The selection of materials for our membrane application has been addressed in Chapter 1. This chapter delves into the rationale behind choosing silicon as the material for the frame, highlighting its compatibility, mechanical properties, and suitability for our specific application.

1. **Material Compatibility:** Silicon (Si) is highly compatible with Si_3N_4 and other semiconductor materials commonly used in MEMS and thin-film applications. This compatibility ensures minimal interface issues and reliable integration.
2. **Thermal Expansion Coefficient:** Silicon has a well-understood CTE, which closely matches that of Si_3N_4. This minimizes thermal stress during temperature changes, reducing the risk of warping or delamination.
3. **Mechanical Properties:** Silicon offers excellent mechanical stability and strength, providing robust support for delicate membrane structures while maintaining structural integrity under operational conditions.
4. **Fabrication Processes:** Silicon is widely used in microfabrication, with well-established processes for etching, doping, and surface treatment. This allows for precise and reproducible manufacturing of complex geometries, such as the frame used in our applications.
5. **Electrical Properties:** Silicon is a semiconductor, allowing for potential integration with electronic components if needed. This adds versatility to the design, enabling the possibility of incorporating sensing or actuation elements directly onto the frame.

Silicon's unique combination of properties makes it an ideal choice for the frame, ensuring optimal performance and reliability in the filter application.

2.2. Materials as Membranes

Si_3N_4 and SiC are utilized as very thin and strong membranes in advanced optical filtering technologies. These materials are chosen for their exceptional mechanical properties, which allow them to be fabricated into ultra-thin membranes, creating an almost ”substrate-less” device. This is particularly advantageous because we can minimize substrate material to reduce electromagnetic losses.

2.2.1. Benefits of Si_3N_4 and SiC as Membranes

Si_3N_4 and SiC are favoured in this application for several reasons:

- **Ultra-Thin Fabrication**: Both materials can be made extremely thin, significantly reducing the amount of material that electromagnetic waves must traverse. This nearly "substrate-less" configuration minimizes signal loss and enhances the device's efficiency.
- **Perforation Capability**: These membranes can be perforated, further decreasing material presence and thus limiting electromagnetic energy dissipation.
- **Support Structure**: Despite their thinness, Si_3N_4 and SiC provide sufficient mechanical strength to act as carriers or support structures. This support is crucial for maintaining the integrity and functionality of the mesh.

2.2.2. Material Properties

Si_3N_4 and SiC are reasonably transparent in the far-infrared spectrum, making them suitable for minimizing energy dissipation. Their transparency ensures that they do not significantly absorb or dissipate electromagnetic energy, which is vital for maintaining the efficiency of the optical filters. Key literature references support the suitability of Si_3N_4 and SiC for these applications, highlighting their optimal properties for use in FIR filters [29], [30].

2.2.3. Thermo-Mechanical Challenges

Creating devices with such thin membranes introduces several thermo-mechanical challenges:

- **Robustness**: The membranes must be robust enough to withstand the mechanical stresses encountered during operation, including vibration loads.
- **Thermal Coupling**: Effective thermal coupling to the mounting frame (which is usually made of silicon) is necessary to manage heat dissipation and maintain stable operating temperatures.
- **Temperature Cycling**: The membranes must survive extreme temperature differences during cycling and final operating conditions without degrading. This involves maintaining structural integrity and functional performance under varying thermal conditions.

2.2.4. Analysis and Experimental Verification

The structural integrity and suitability of these materials for device applications can be studied through both analytical methods and experimental verification. Key aspects to investigate include assessing the membranes' ability to withstand mechanical stresses and vibration loads. Thermal properties also need to be studied to ensure minimum stress buildup between the membrane and frame on cryogenic cooling.

2.3. Thermo-Mechanical Characteristics

This section delves into the critical importance of effective thermal coupling between the Si_3N_4 membrane and its silicon frame. It begins by specifying the CTE differences between the materials, then explores the impact of thermal stress, and finally addresses key considerations to keep in mind during modelling.

Effective thermal coupling between the Si_3N_4 membrane and its silicon frame is crucial due to differential thermal expansion, which can introduce mechanical stresses under the temperature variations experienced in space. These stresses can potentially lead to structural failures or performance degradation.

Silicon has a CTE of approximately 2.527×10^{-6} K^{-1} at 290K, while Si_3N_4 has a CTE of about 3.17×10^{-6} K^{-1} at 290K [31]. This difference in CTE can cause significant mechanical stresses at the interface of these materials in composite structures, especially under the extreme and rapidly changing temperature gradients in space.

(a) There is no restriction on the object expanding/shrinking, no force is generated

(b) The deformation of the object expanding/shrinking is limited, stress will build in the object

Figure 2.1: Consequences of restriction on stresses developed in a body

For missions like PRIMA, where precise dimensional stability is critical, managing these differential expansions is essential. Engineers must design instruments to accommodate these discrepancies using techniques like buffer layers, compliant materials, or structural modifications [32].

2.3.1. Impact of Thermal Stress on Membrane Structures

Dynamic Factors

Spaceborne structures are also subject to dynamic stresses from operational loads such as vibrations during launch and interactions with space debris. These mechanical constraints, combined with thermal stresses, necessitate comprehensive analysis to predict the reliability and performance of structural components in space [33], [34].

(a) Layered material with high CTE on top, low CTE at the bottom at 130 °C

(b) Warpage induced in the material due to uneven shrinking at 25 °C

Figure 2.2: Consequences of CTE differences in layered materials

Predictive modelling using COMSOL Multiphysics allows for the integration of heat transfer and structural properties to provide a holistic view of membrane responses under varying thermal conditions. This helps in predicting and optimizing material combinations and configurations to mitigate thermal stress risks [35].

2.3.2. Considerations During Design and Modeling of Membranes

- **Consequences of Pre-stress**: The influence of membrane pre-stressing during fabrication on the material properties is investigated, with a specific focus on analyzing the mechanical stresses at the Si_3N_4-Si interface. Additionally, the membrane is cooled down to 50K to evaluate whether the resulting thermal stresses could be withstood by the material.
- **Membrane-Frame Shrinkage**: One of the specific concerns is the fact that the membrane is already stretched like a drum, ensuring that it is very flat. Hence, it is crucial to ensure that the frame does not shrink excessively relative to the membrane. Excessive shrinkage can exert inward force, reducing the pre-stress required for high-frequency and low-amplitude operations.
- **Multiphysics Coupled Analysis**: By integrating thermal and mechanical behaviours in a unified simulation environment, a comprehensive understanding of material performance under mission conditions is gained, ensuring the integrity and functionality of LVFs in space.

2.4. Measurement Techniques

To address the challenges of developing LVFs for far-infrared (FIR) applications, several key concepts are studied and analyzed. First, the thermal expansion behaviour of the materials is investigated to ensure they could withstand extreme temperature variations without performance degradation. Second, stress distribution within the membrane is analyzed to maintain pre-stress, crucial for high-frequency, low-amplitude operation. Finally, the membrane-frame interaction is examined to prevent warpage.

FEM is employed for detailed simulations of these behaviours, with COMSOL Multiphysics chosen for its ability to integrate heat transfer and structural mechanics in a comprehensive multiphysics environment. This allowed for accurate simulation and prediction of eigenfrequencies, mode shapes, and stress distributions.

In addition to simulations, experimental techniques are utilized to validate the models. The LyncéeTec Digital Holographic Microscopy (DHM) system is used to capture high-resolution dynamic responses and visualize eigenfrequencies. The Polytec Laser Doppler Vibrometer (LDV) further validated the results by measuring the vibration characteristics of the membranes. Combined, these methods ensured robust validation and optimization of the LVF designs, addressing the critical issues related to thermal expansion, stress distribution, and mechanical vibrations.

2.4.1. Analytical and Numerical Techniques

Literature Review on Eigenfrequency and Stress-Strain Analysis

The theoretical foundation for understanding eigenfrequencies, mode shapes, and stress-strain relationships in structural systems is well-documented. Key texts such as Rao's "Mechanical Vibrations" offer comprehensive insights into calculating eigenfrequencies and analyzing mode shapes in various structural configurations [36].

Blevins' work on structural dynamics and Roark's formulations provide essential methodologies for understanding material responses under stress and strain, especially relevant for pre-stressed membranes. These studies are crucial for predicting how pre-stresses affect membrane behaviour under operational conditions [37], [38].

Formula for Frequency Derivation:

$$f_{ij} = \frac{\lambda_{ij}}{2}\sqrt{\frac{S}{\gamma A}}, \quad \text{and} \quad \lambda_{ij} = \sqrt{i^2\frac{b}{a} + j^2\frac{a}{b}}. \tag{2.1}$$

Here, a and b are the side lengths, A is the surface area, S is the tension per unit edge, and γ is the mass per unit area.

These references form a comprehensive framework for simulating and practically applying stress and vibrational analysis in membrane technologies.

Simulation and Validation of Membrane Dynamics Using COMSOL

Building on theoretical knowledge, COMSOL Multiphysics was used to simulate the dynamic behaviour of membranes. The membrane interface in COMSOL, designed for thin structures primarily undergoing in-plane stresses, is employed to analyze eigenfrequencies and mode shapes. Initial simulations are conducted at room temperature and then the system was cooled to 50 K. We also included a material study examining differences in eigenfrequencies when using Si_3N_4 and silicon carbide SiC [39].

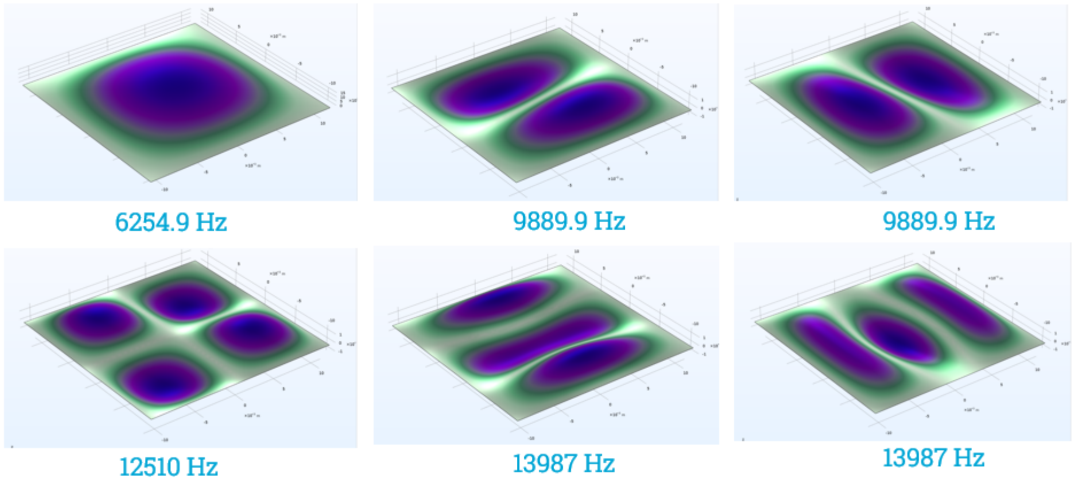

Figure 2.3: First six eigenfrequencies of silicon nitride and their corresponding mode shapes

Requirement of a Silicon Frame

The silicon frame provides structural integrity and a robust point of attachment, essential for handling and transporting the membrane assembly. Designed to minimize its influence on the vibrational characteristics of the membrane, the frame ensures durability without compromising performance.

Thermomechanical Analysis

A thermomechanical analysis is conducted, lowering the temperature to 50 K to simulate space conditions. This analysis focuses on:

1. Differential expansion or contraction between silicon and silicon nitride, affecting stress levels.
2. Stress analysis in the membrane as the system cools, is crucial for understanding structural integrity under space conditions.
3. Static analysis of end-state stress distribution post-cooling.
4. Incorporation of feedback mechanisms to enhance model predictions and design robustness.

This comprehensive analysis increases our understanding of material behaviour under simulated space environments and provides crucial validation data for refining simulation models.

2.4.2. Experimental Techniques - DHM

The core of DHM lies in capturing phase and amplitude information through the interference of light waves, enabling precise 3D imaging. The fundamentals of Digital Holographic Microscopy are rooted in optics, including principles like interference, fringe formation, intensity, and amplitude analysis.

Interference

Interference is a phenomenon where two or more light waves superpose to form a resultant wave. The principle of superposition states that the resultant intensity at any point is the sum of the intensities of the individual waves. Interference can be constructive or destructive:

- **Constructive Interference:** Occurs when the phase difference between the waves is an even multiple of π, resulting in a higher amplitude.
- **Destructive Interference:** Occurs when the phase difference is an odd multiple of π, leading to a lower or zero amplitude.

Fringe Formation

Fringes are the visible patterns resulting from the interference of light waves. In DHM, these fringes contain information about the phase and amplitude of the object wavefront. The spacing and orientation of the fringes are related to the optical path difference between the interfering waves.

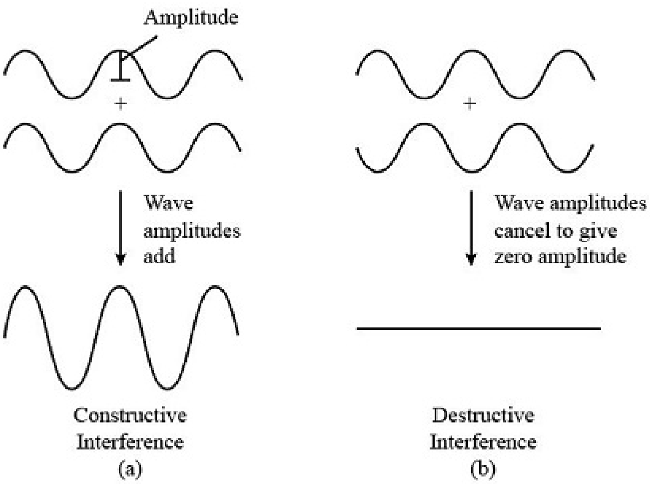

Figure 2.4: Constructive and destructive interference

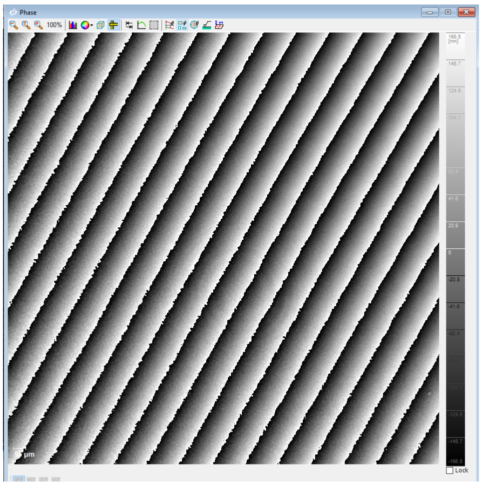

Figure 2.5: Fringes as visible on a membrane

Intensity and Amplitudes

The intensity of light in an interference pattern is given by:

$$I = I_1 + I_2 + 2\sqrt{I_1 I_2}\cos(\Delta\phi) \tag{2.2}$$

where I_1 and I_2 are the intensities of the individual waves, and $\Delta\phi$ is the phase difference between them. The amplitude A of the resultant wave is related to the amplitudes of the individual waves A_1 and A_2 by:

$$A = \sqrt{A_1^2 + A_2^2 + 2A_1A_2\cos(\Delta\phi)} \tag{2.3}$$

Moving from Optics to Data Capture

In DHM, the captured holograms encode both the amplitude and phase information of the object wavefront. By analyzing the interference fringes, the mode shapes and eigenfrequencies of an object can be determined.

Digital Holography Microscopy (DHM)

The DHM R2200 [40] uses time-resolved DHM to measure eigenfrequencies and mode shapes, capturing dynamic responses to stimuli like vibrations or acoustic pressure waves. It records multiple holograms in quick succession, providing a detailed snapshot of an object's deformation over time. These holographic images contain both amplitude and phase information, revealing the object's mode shapes and eigenfrequencies through sophisticated phase variation analysis.

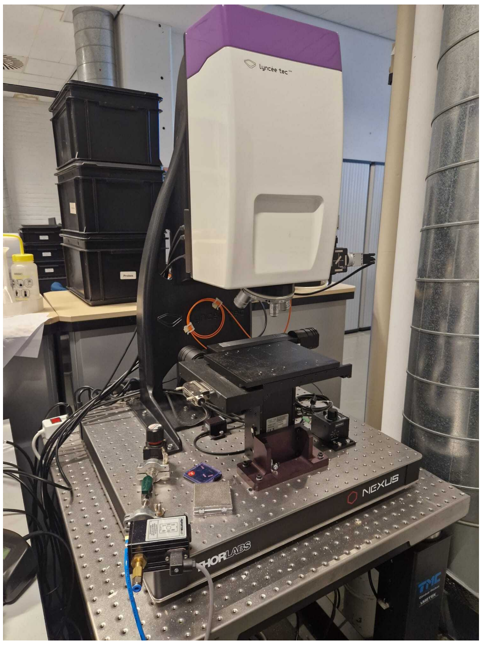

Figure 2.6: The Lynceetec DHM R2200

The DHM R2200 features three light sources, facilitating simultaneous interferences captured on the same camera. These interferences are recorded on a shared hologram and reconstructed independently, extending the measurement range up to 12 microns.

Utility in Optical Instrument Research

The DHM R2200 is pivotal in optical instrument research, providing unparalleled insights into the mechanical properties and dynamic behaviours of optical components. Key advantages include:

- **Non-Contact Measurement:** Preserves the integrity of delicate optical components by avoiding physical stress or alteration during examinations.
- **High Resolution and Precision:** Measures nanometric displacements and surface deformations, essential for fine-tuning optical components and validating theoretical models.
- **Real-Time Analysis:** Allows observation of dynamic events in real-time, crucial for assessing the impact of environmental changes or operational stresses.
- **Versatility:** Adaptable to various materials and structures, making it invaluable for both fundamental studies and applied engineering projects.

In summary, the DHM R2200 bridges theoretical predictions and practical outcomes, enhancing the development and refinement of optical components. It is instrumental in advancing the field of optics, paving the way for discoveries and innovations.

2.4.3. Experimental Techniques - LDV

The fundamentals of Laser Doppler Vibrometry are based on the Doppler effect, measuring frequency shifts to determine the velocity and displacement of vibrating objects.

Doppler Effect

The Doppler effect is the change in frequency or wavelength of light due to the relative motion between the light source and the observer. In LDV, this effect is used to measure the velocity of a vibrating surface. When the surface moves towards the laser source, the frequency of the reflected light increases; when it moves away, the frequency decreases.

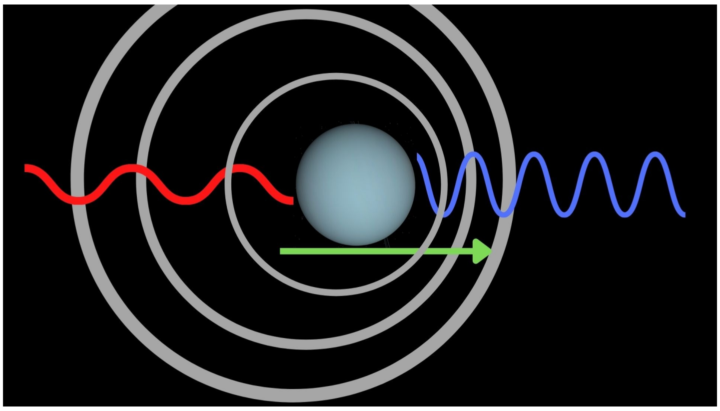

Figure 2.7: Doppler effect

Velocity Measurement

The LDV measures the frequency shift (Doppler shift) of the reflected light to determine the velocity of the vibrating surface. The velocity v is given by:

$$v = \frac{\Delta f \lambda}{2} \tag{2.4}$$

where Δf is the frequency shift and λ is the wavelength of the laser light.

Non-Contact Measurement

Like DHM, LDV is a non-contact method, ensuring that the integrity of delicate components is maintained during measurements. This is particularly important in applications involving sensitive optical components and materials.

Moving from Optics to Data Capture

LDV is used to accurately measure the vibrational characteristics of optical components. By analyzing the frequency shifts caused by vibrations, detailed information about the velocity, displacement, and acceleration of the components can be obtained. This data is crucial for validating theoretical models and ensuring the reliability of optical instruments.

2.4.4. LDV

The Polytec PSV-400 LDV is another crucial tool for validating dynamic responses and modal properties.

Capturing Vibration Data

The Polytec PSV-400 utilizes LDV to measure vibrations with high precision. It operates by directing a laser beam onto the surface of an object and detecting frequency shifts in the reflected light caused by the object's motion. This non-contact method provides accurate data on the velocity, displacement, and acceleration of vibrating surfaces, making it ideal for analyzing the dynamic behaviour of optical components.

Utility in Optical Instrument Research

The PSV-400 offers several advantages for optical research:

- **High Precision Measurement:** Capable of detecting minute vibrations with high accuracy, essential for detailed modal analysis.
- **Non-Contact Method:** Ensures no physical interference with the tested object, preserving the integrity of delicate components.

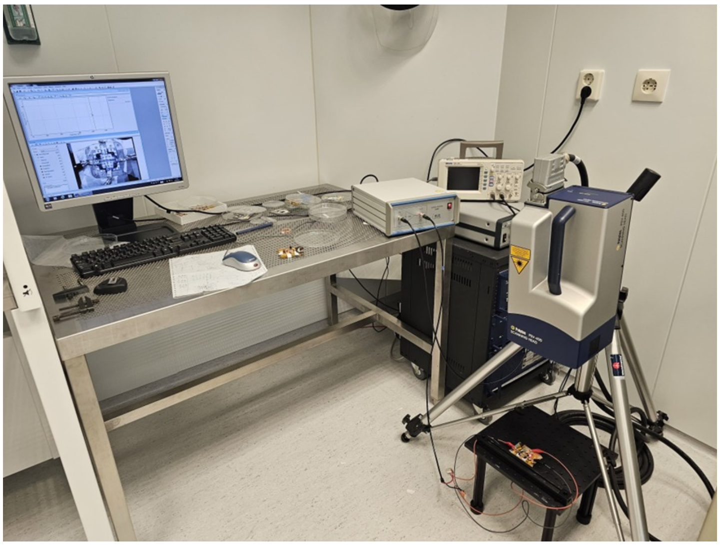

Figure 2.8: The Polytec PSV-400 setup

- **Versatile Applications:** Suitable for a wide range of materials and structures, from small MEMS devices to large aerospace components.
- **Real-Time Data Acquisition:** Provides immediate feedback on vibrational behaviour, allowing for rapid assessment and adjustments.

In summary, the Polytec PSV-400 LDV complements the DHM by providing detailed vibration analysis and validating theoretical models. Its non-contact, high-precision measurements are vital for ensuring the reliability and performance of spaceborne optical instruments.

2.4.5. Integration of Techniques for Comprehensive Analysis

The combined use of DHM for detailed modal analysis, and LDV for precise vibration measurements creates a strong framework for improving the design and performance of optical components for space. This integration allows for a thorough comparison between theoretical predictions and actual behaviours, enhancing the validation and refinement of our COMSOL simulation models. This comprehensive approach ensures that our designs are theoretically robust and practically viable under the demanding conditions of space operations.

2.5. Literature Conclusions

The exploration of membrane materials, thermomechanical characteristics, and advanced measurement techniques offers a comprehensive foundation for designing optical components suited for space applications.

Si_3N_4 and SiC are critical materials in this context, valued for their exceptional mechanical, thermal, and electrical properties. By integrating advanced measurement techniques such as Digital Holography Microscopy (DHM) and Laser Doppler Vibrometry (LDV) with COMSOL Multiphysics simulations, we establish a robust framework for validating and refining theoretical models.

In summary, the selection of appropriate materials, precise modelling, and empirical validation are essential for the development of reliable optical components for space missions. This integrated approach ensures that the components will perform effectively under the demanding conditions of space.

3 Research Methodology

This chapter outlines the research methodology designed to address the key objectives of this thesis. It starts with defining the questions that formulated the basis of our research and the objectives to answer these questions. Through a combination of FEM simulations and experimental validations, this chapter provides a detailed account of the methodologies employed to achieve these research goals.

3.1. Research Objectives

It has been established that an LVF for the FIR spectrum typically consists of a thin membrane with a variable bandpass filter pattern across its surface. The operational principle of an LVF is based on spatially varying optical properties, allowing it to filter different wavelengths of light at different positions. Membranes are an integral part of an LVF and they allow for the creation of extremely thin, lightweight, and flexible filters, which are ideal for space applications where weight and volume are at a premium.

The choice of materials for LVFs, particularly for cryogenic and FIR applications, is driven by several factors. Si_3N_4 is often selected due to its excellent mechanical strength, how thin it can be made, and high pre-stress in the FIR range. These properties make it suitable for creating robust, high-performance filters that can withstand the harsh conditions of space. The thermo-mechanical properties of the materials are critical because the LVF must maintain its structural integrity and optical performance across a wide range of temperatures. Therefore, the effects of thermal expansion, stress distribution, and mechanical vibrations on the filter's performance and longevity need to be understood.

Based on these observations, the research questions are formulated as follows:

"How do the thickness and pre-stress of Si_3N_4 membranes influence the modal properties and stress distribution of LVFs in far-infrared (FIR) applications?"

and

"How can the thermo-mechanical behaviour of membranes be modelled and validated to ensure reliability in cryogenic, far-infrared space environments?"

To address these research questions, the following research objectives are devised:

- **Analyze the Effect of Membrane Thickness and Tension on Modal Properties:** The impact of varying the thickness and tension of Si_3N_4 membranes on their eigenfrequencies, mode shapes, and dynamic responses is studied using FEM simulations.
- **Evaluate Stress Distribution in LVF Membranes:** The stress distribution across $\mathrm{Si_3N_4}$ membranes under different operating conditions is examined to ensure structural integrity, with a focus on pre-stressed membrane configurations.
- **Develop and Validate a Comprehensive Model:** A detailed model is created using COMSOL Multiphysics to simulate the thermal expansion and mechanical behavior of $\mathrm{Si_3N_4}$ membranes in

cryogenic, FIR environments. This model is validated through experimental techniques such as DHM and LDV.

3.2. Thesis Overview

To achieve the research objectives, this thesis is divided into three phases:

1. **Simulation Phase**: In this phase, COMSOL Multiphysics is used to model the Si_3N_4 membranes, focusing on their thickness and tension. An eigenfrequency analysis is performed to investigate the vibrational characteristics and identify the membranes' modal properties and stress profiles under different conditions.
2. **Experimental Phase**: This phase involves validating our membrane model through experimental techniques like DHM and LDV which allow for the measurement of the vibrational behaviour of the membrane in a real-world setting.
3. **Comparison Phase**: During this phase, the simulation results are compared with experimental data to check for similarities and assess if the parameters from both are comparable within an acceptable tolerance band. If differences between the simulation and reality are not random and are within tolerance, hypotheses are proposed to explain the discrepancies and investigate potential reasons for them.

The thesis is structured to encompass these phases systematically, starting with simulations and followed by experimental setups. In the final segment, the results from both the experimental and simulation phases are combined in the comparison phase. The following sections elaborate further on the details and expected outcomes of each phase.

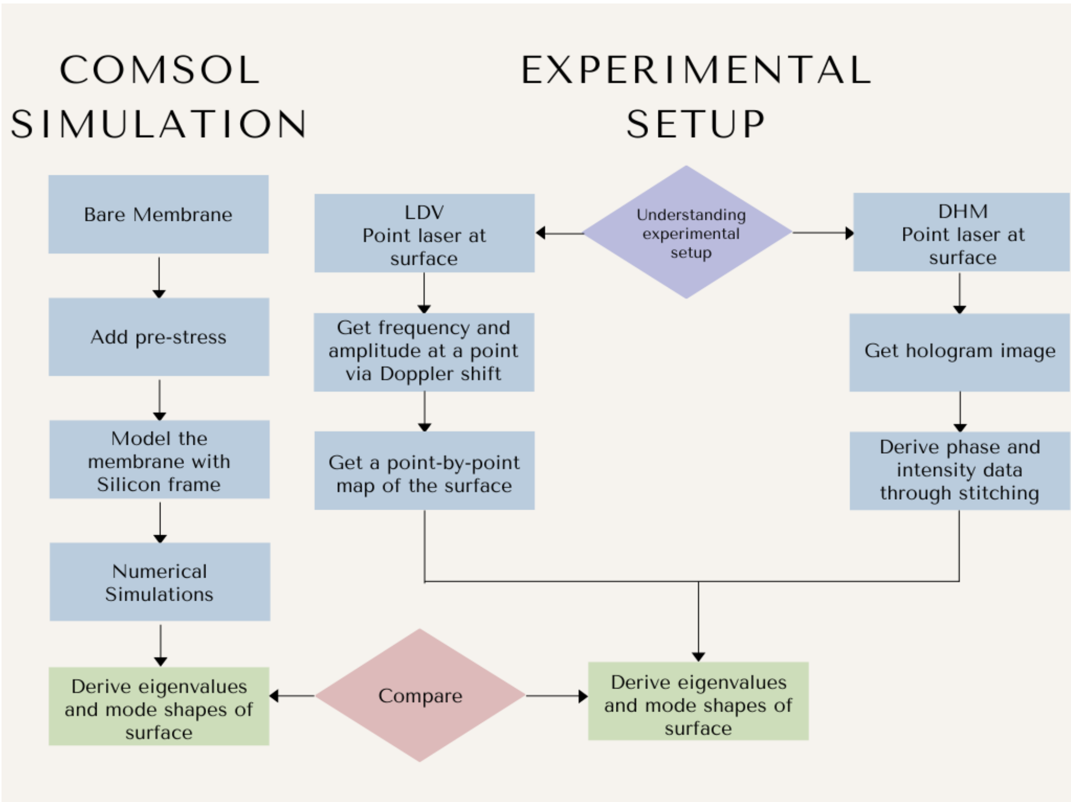

Figure 3.1: Thesis overview

3.3. Simulation Methodology

For the simulation phase, COMSOL Multiphysics software is used. The models are developed to replicate the experimental conditions and included detailed material properties and geometric configurations. First, the eigenmodes and frequencies of the bare LVF membranes (with and without a frame) are simulated to understand their dynamic behaviour. Then, the membrane is cooled in the simulations to replicate the low temperatures of space, and the resulting stress and strain patterns are analyzed. Finally, a gold layer is utilized to minimize ohmic losses, and COMSOL is employed to analyze the impact of this deposition on the eigenfrequencies.

3.3.1. Methodological Framework for Membrane and Frame Analysis

To streamline the research methodology, the approach can be systematically divided into two primary sections:

- **Membrane Analysis Without a Gold Layer:**
  In this section, we focus on modelling the bare membranes without the inclusion of a gold layer. This analysis is further subdivided into the following stages:
  1. **Bare Membrane:** The initial step involves simulating a square membrane with dimensions of 20 mm x 20 mm to determine its eigenfrequencies and mode shapes. The membrane, with a thickness of 500 nm, was subjected to pre-stress, and its behaviour under these conditions is thoroughly examined.
  2. **System of Membrane and Frame:** Subsequently, a silicon frame, with a width of 5 mm, is layered on top of the membrane and the eigenfrequencies and mode shapes of this composite system are analyzed. Additionally, the stress distribution between the frame and the membrane, as well as the stress associated with various mode shapes, are evaluated.
  3. **Cooled Membrane and Frame System to 50 K:** Finally, the entire membrane-frame system is cooled down to 50 K in a transient analysis. The resulting thermal stresses within the membrane are investigated, along with any changes in eigenfrequencies and mode shapes due to the cooling process.
- **Membrane Analysis With a Gold Layer:**
  This section extends the analysis to membranes that include a gold layer on the surface. The analysis is subdivided into the following components:
  1. **Gold-Layered Membrane:** In a similar approach to the previous analysis, a square membrane with a 100 nm gold layer on top is modelled to determine its eigenfrequencies and mode shapes. The membrane is subjected to identical boundary conditions, and its behaviour is assessed accordingly.
  2. **Gold-Layered Membrane and Frame System:** The next stage involves layering a gold layer on the membrane-frame system. Under similar conditions, the eigenfrequencies and mode shapes of this composite system are analyzed.
  3. **Cooling the Gold-Layered Membrane and Frame to 50 K:** Lastly, the gold-layered membrane-frame system is cooled down to 50 K in a transient analysis. The study examines the thermal stresses developed within the membrane and the changes in eigenfrequencies due to cooling.

The primary objective is to successfully cool the bare membrane and frame assembly to 50 K. Upon achieving this goal, the analysis is extended to include the effects of adding a gold layer, thereby providing a more comprehensive understanding of the system's behaviour under cryogenic conditions.

3.3.2. Elaborating On Model Configurations

This section outlines the configurations required for modelling a pre-stressed membrane using COMSOL Multiphysics. The discussion begins by justifying the choice of the membrane model, followed by an examination of the geometrical considerations, pre-stress application, cooling processes, and thickness settings. Each aspect is tailored to simulate the membrane's behaviour under various conditions, ensuring that the model reflects the physical characteristics and constraints of the actual system.

Justification for Selecting the Membrane Model:

While the COMSOL models were being configured, a choice was made between the plate, shell, and membrane models to accurately depict the filter. Based on Blevin's formulation [37], the characteristics of the three models were identified.

Plates	Shells	Membranes
1. Flatness and constant thickness.	1. Constant thickness.	1. Ability to support only tensile loads, not bending moments.
2. Homogeneous, linear elastic, isotropic material composition.	2. Thin walls relative to their radius.	2. Described by their mass per unit surface area and tension per unit length of boundary.
3. Thinness relative to their lateral dimensions.	3. Composition of linear elastic, homogeneous isotropic material.	3. Suitable for characterizing mode shapes and natural frequencies under fixed boundary conditions.
4. Deformation primarily through flexural deformation.	4. No loads applied to the shells.	
5. Zero in-plane load on the plates.	5. Deformations small compared to the shell radius.	

For our application, the zero in-plane load characteristic of plates is considered a significant limitation, as in-plane loads (here, pre-stresses in the membrane) are crucial to the study. Although shells can support both bending and in-plane stresses, the assumption that no loads are applied to the shells disqualifies this model for the specific needs, as there are mechanical loads/vibrations experienced by the LVF filter during launch.

Taking this into account, the membrane model is deemed appropriate for the LVF simulations because it accurately reflects the significant in-plane stresses and the negligible bending rigidity typical of the thin films being studied.

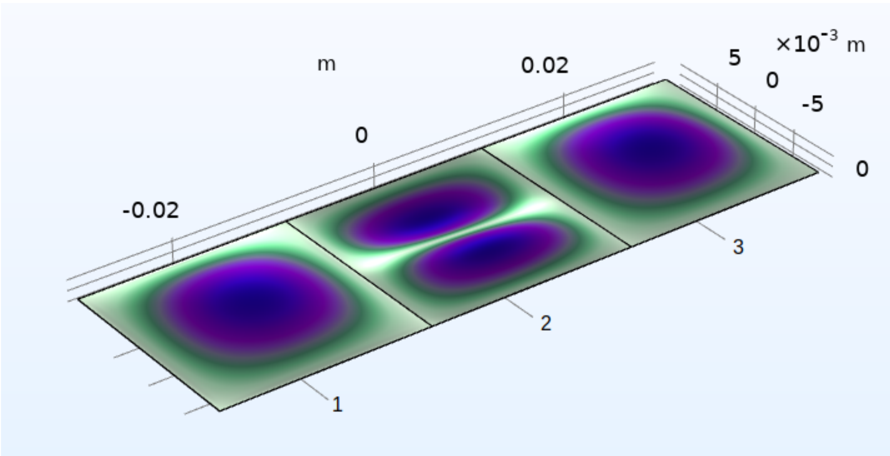

Figure 3.2: The comparison between three models (plate, membrane, shell)

In Figure 3.2, a membrane model (2) is shown wedged between a plate (1) and a shell model (3). The second eigenfrequency is observed in the membrane model but not in the shell or the plate. This observation validates the use of the membrane model.

Pre-stress of Membrane:

During fabrication, pre-stress is introduced in the filter membrane due to the processing techniques used. Si_3N_4 is initially deposited onto a Si substrate, inherently developing tensile stress. The large tensile stress in stoichiometric Si_3N_4 results from the shrinkage of the bulk of the film during and after growth, caused by dissociation of Si–H and N–H bonds and rearrangement of the dangling bonds to stable Si–N bonds. This stress is crucial for the membrane's stability. Subsequently, the underlying silicon is selectively etched away releasing the Si_3N_4 membrane.

The forces significantly influence the mechanical properties and performance of the membrane, ensuring that it maintains the desired shape and functionality in the final device. The value of this pre-stress is around 100 MPa for Si_3N_4. [41] [42].

The Distributed Forces Along the Height:

Here height is introduced using the 'thickness and offset' option. The pretension force is applied along the height of the membrane (similar to stretching a drum), resulting in a distributed force along the height of the membrane, as shown in Figure 3.3.

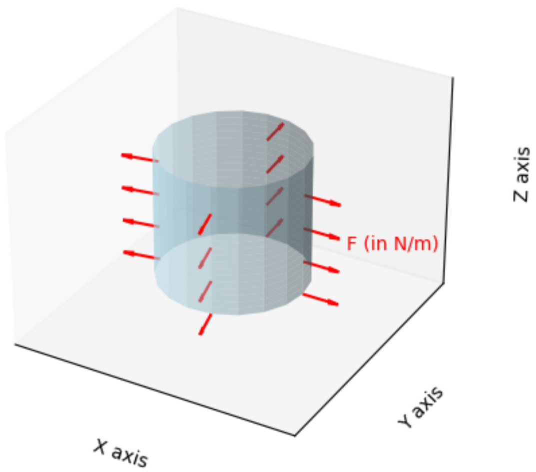

Figure 3.3: The stretched membrane

Based on a thickness of 500 nm, the force in N/m is calculated:

$$\text{Force in N/m} = 100\,\text{MPa} \times \text{thickness (nm)} = 50\,\text{N/m}$$

To simplify the stress tensor for a plane stress condition, where there are no shear stresses and only normal stresses in the x and y directions, the pre-stress tensor for the pre-stressed membrane is represented as a 2x2 matrix

$$\sigma = \begin{bmatrix} \sigma_{xx} & 0 \\ 0 & \sigma_{yy} \end{bmatrix} \tag{3.1}$$

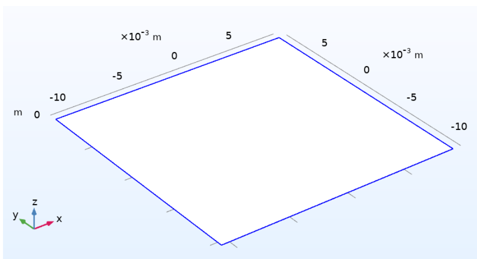

Figure 3.4: Membrane without frame

Geometries:

The geometrical configurations in this study are tailored to meet the specific requirements of each analysis stage. The process begins with modelling a bare membrane as a 20 mm x 20 mm square, with a thickness of 500 nm, fixed at the outer edges. Next, a 5 mm wide silicon frame is added around the membrane's edges, expanding the geometry to 30 mm x 30 mm, and this membrane-frame system is further analyzed. After this, the membrane-frame assembly is then subjected to cooling simulations down to 50 K. For the gold-layered analysis, the same steps are followed; however, for the cooling process, the frame is excluded to simplify computational requirements.

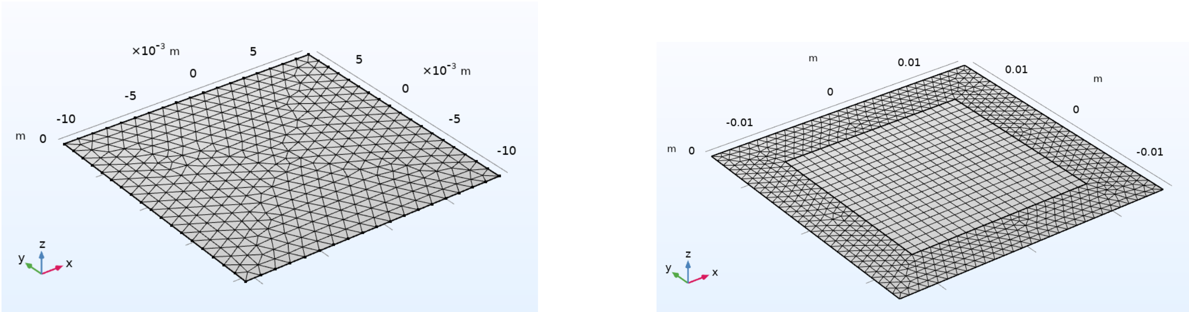

(a) Mesh of bare membrane

(b) Mesh of the membrane with frame

Figure 3.5: Meshes in the system

Material Properties for the Membrane Analysis:

The primary membrane material utilized is Si_3N_4, with ongoing investigations into the feasibility of using SiC as an alternative membrane material. Both Si_3N_4 and SiC have established applications as membrane materials. The properties of Si_3N_4 are sourced from the Ansys Granta Edupack [43], while the values for SiC are derived from Xu et al. [44].

In COMSOL, the calculations for mode shapes of vibrating membranes are governed by the equations of motion, stress-strain relationships, and strain-displacement relationships. These equations incorporate key material properties, including Young's modulus (E), Poisson's ratio (ν), and density (ρ). A detailed description of these equations can be found in Appendix D.

Steps for Thermal Analysis:

COMSOL models relating to thermomechanical modelling are developed, where the membrane and frame are cooled down to 50 K. A gold layer is incorporated on top of the membrane, and the entire system is subjected to transient cooling down to 50 K.

The operational temperature of the LVF is maintained at 100 mK, identical to that of the detector. The mechanical properties of the materials used do not exhibit any significant changes between temperatures of 4.2 K and lower. The most pronounced difference in the CTE occurs between room temperature and approximately 50 K, where a significant shift in material expansion characteristics is observed. Understanding these thermal dynamics is essential for optimizing the LVF's performance across varying temperatures.

The aims specified in my study goal are:

1. **Objective 1**: To understand how the differential expansion or contraction between silicon (Si) and silicon nitride Si_3N_4 due to temperature changes affects the stress levels in composite structures or interfaces.
2. **Objective 2**: To analyze and measure the stress developed in a membrane when the system is cooled, potentially rapidly, by liquid nitrogen. The stress due to the cooling down process is verified to be within acceptable limits.

Just as the membrane interface can be used for structural mechanics in 3D on thin structures, a heat transfer interface in the Shells module is added. This allows the membrane to be selected for the heat transfer interface. Both a heat transfer interface and a multiphysics interface are incorporated to link the heat transfer and the structural mechanics. A Thermal Expansion subnode is added for the linking. As per usual, this is an approximate study since it is not defined for membrane mechanics.

The membrane is cooled down from 290 K to 50 K using the following equation, where the temperature is changed with respect to time:

$$T_0 = 293.15\,[\text{K}] - 2\,[\text{K/min}] \times t \tag{3.2}$$

It is crucial to note that material properties like Young's modulus and density vary with temperature. Poisson's ratio, being dependent on internal structure and bonding, exhibited minimal change with temperature.

The volumetric thermal expansion equations for density [45] and Young's modulus are given by:

$$\rho = \rho_1 \left(1 + b(T - T_r)\right) \tag{3.3}$$

$$E = E_1 \left(1 + b(T - T_r)\right) \tag{3.4}$$

where:

- ρ is the density at temperature T,
- ρ_1 is the reference density at the reference temperature T_r,
- E is Young's modulus at temperature T,
- E_1 is the reference Young's modulus at the reference temperature T_r,
- ν is Poisson's ratio at temperature T,
- ν_1 is the reference Poisson's ratio at the reference temperature T_r,
- b= (+/-)β is the coefficient of volumetric thermal expansion, defined as $\beta = 3\alpha$, where α is the coefficient of thermal expansion (CTE)
- T is the current temperature, and
- T_r is the reference temperature.

An important consideration is that the CTE of a material also changes with temperature. Therefore, it is essential to know the varying CTE values for each material (in this case, Si_3N_4 and Si) across the entire temperature range of interest, spanning from 290 K to 50 K. These values are derived from the Material Property Database by JAHM Software, Inc [46].

Steps For the Addition of a Gold Layer

The next modelling objective involves the addition of a 100 nm layer of gold on top of the Si_3N_4 membrane. Gold, being an excellent conductor, minimizes ohmic losses in the component, influencing transmission, bandwidth, spectral resolving power, and resonance frequency. This mechanism is analogous to the operation of mechanical resonators.

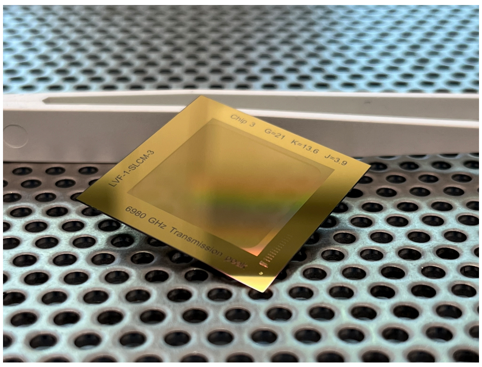

Figure 3.6: Shiny gold layer on top of the membrane

Impact on Eigenfrequency

- Mass Increase: The addition of a layer of gold increases the mass of the membrane, which inversely affects the eigenfrequency. The eigenfrequency f is given by:

$$f \propto \sqrt{\frac{T}{m}} \tag{3.5}$$

  where T is the tension and m is the mass per unit area. Increasing the mass m lowers the eigenfrequency.
- Trade-off Consideration: While the reduction in eigenfrequency is a drawback, the benefits provided by the gold layer are considered more critical for the specific application of the optical filter.

The material properties are derived from COMSOL's material directory.

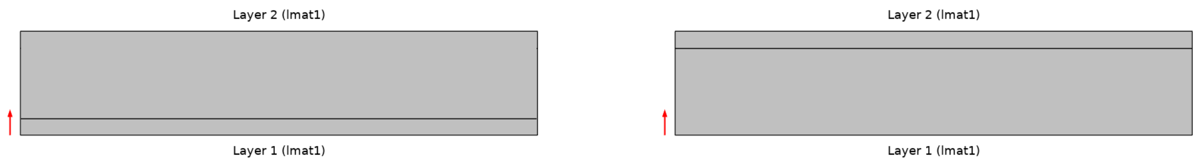

(a) A layered material defined with 500 nm of Si_3N_4 and 375 µm of Si on top of it

(b) A layered material defined with 500 nm of Si_3N_4 and 100 nm of Au on top of it

Figure 3.7: Layering in the System

One of the key issues with layering materials on top of each other is the absence of a layered membrane interface. This issue arises because the added layers introduce bending stiffness, which is typically ignored in the membrane interface model. To address this, we implement a workaround by defining the material itself as layered. Instead of externally defining the layers and then assigning a material to them, we directly define the material properties to reflect the layered structure. The only addition required is a Layered linear elastic material node.

3.4. Experimental Methodology

The experimental phase involves the use of Digital Holography Microscopy (DHM) and LDV to capture eigenmodes, frequencies, and vibrational data of the LVF membranes. The DHM provides detailed holographic images containing both amplitude and phase information, while the LDV measures vibrations using the Doppler effect.

Experimental Setup and Equipment

This section details the specific equipment and instruments used in the experiments, including calibration, settings, and configurations necessary to achieve the research objectives.

For both instruments, a common setup is modelled and manufactured. A base plate serves as the foundational support. On a smaller platform, four piezo actuators are mounted and affixed to the base plate using screws, as shown in Figures 3.8a and 3.8b. The piezos are used to induce vibrations in the sample (in-phase actuation). Figure 3.8c illustrates the positioning of the LVF filter along with the LVF-holder on top of the piezo plate. However, due to constraints in the z-axis height, it is decided not to use the holder. Instead, the LVF is secured on top of the actuator plate with tape for accurate measurement, as depicted in Figure 3.8d.

The CAD drawing depiced in Figure 3.9 illustrates the final setup and the final manufactured part (without the base plate). All 4 piezo actuators are driven by the same input voltage (actuation in phase) the details of which are provided in Section 5.

Clamping Technique

The filter is clamped on the frame using Kapton tape. It is a type of adhesive tape made from a polyimide film developed by DuPont. It is renowned for its exceptional thermal, chemical, and electrical properties,

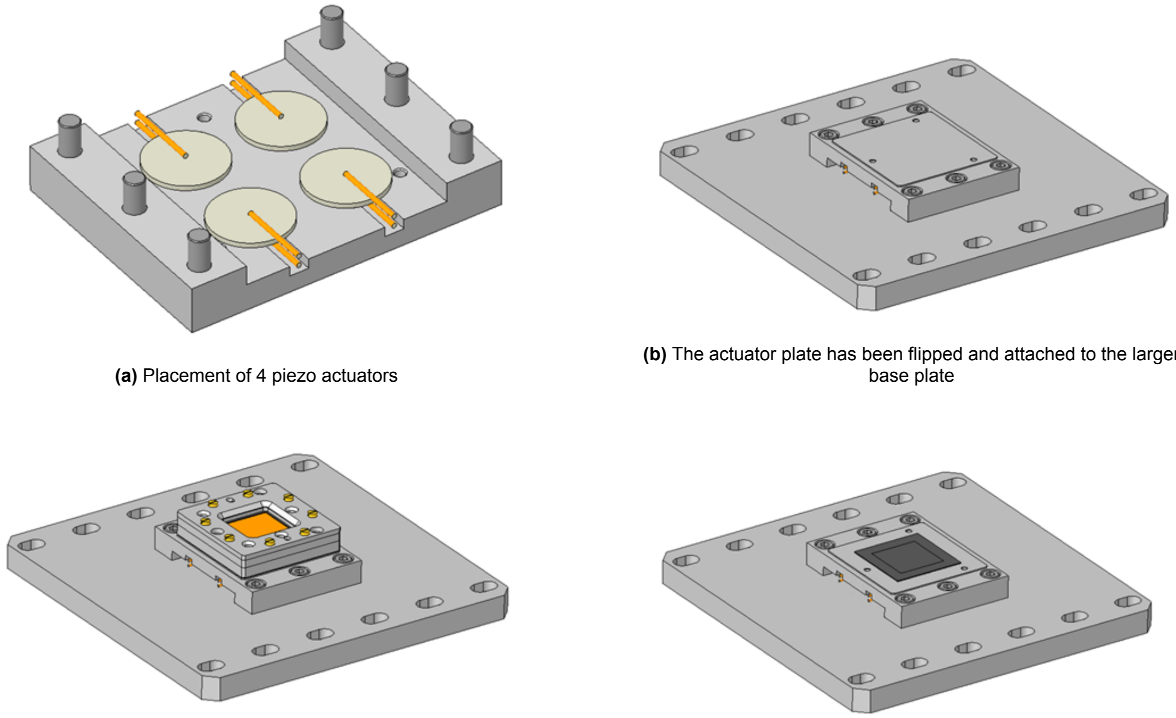

(a) Placement of 4 piezo actuators

(b) The actuator plate has been flipped and attached to the larger base plate

(c) Measurement setup including LVF holder (discarded)

(d) Filter on the backside of the actuator plate

Figure 3.8: Design of the setup

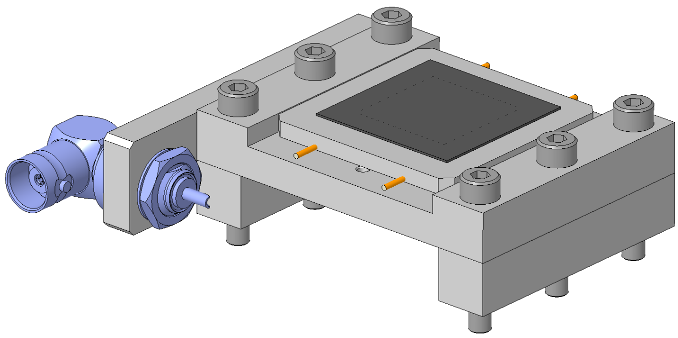

Figure 3.9: Assembled CAD drawing

making it highly suitable for a wide range of industrial applications. Kapton tape can withstand extreme temperatures, ranging from -269°C to +400°C (-452°F to 752°F), without losing its physical properties, which makes it incredibly versatile.

Use of Kapton Tape

Kapton tape is a critical material in spacecraft and satellites due to its ability to withstand extreme temperature variations, provide electrical insulation, and offer mechanical protection. Its chemical resistance ensures long-term reliability, and its lightweight, durable nature makes it ideal for space missions where weight is a crucial factor [47].

Additionally, the tape can be applied and removed without requiring specialized tools or causing physical alterations to the setup, making it convenient and practical.

However, as discussed in Chapter 5, this clamping technique was inadequate and additional methods will have to be used in the future.

We also use blacking tape below the filter. This helps minimize stray light that can interfere with the holographic measurements. It also helps to increase the contrast between the features of interest on the membrane and the background. This is particularly important in DHM, where precise phase and amplitude information are critical.

3.4.1. Material Choice for Experimentation

In the initial phase of this research, silicon nitride (Si_3N_4) and silicon carbide (SiC) were considered as potential materials due to their excellent mechanical and thermal properties.

However, during the sample preparation phase, significant challenges were encountered with the lithographic process for SiC. The existing recipe in the lithographic cleanroom proved inadequate for producing high-quality SiC samples, leading to difficulties in obtaining consistent and reliable material.

Consequently, the focus exclusively shifted on silicon nitride (Si_3N_4) for this research due to its reliable fabrication process and well-documented performance in similar applications.

The entire phase of sample preparation is done at the SRON cleanroom by the lithographic team using their recipe. The preparation of silicon nitride samples involves a series of steps to ensure the quality and consistency required for experimental validity.

3.4.2. Visualizing and Data Capture Process

The imaging process employed in this work involves capturing high-resolution holographic images and precise vibration data. The DHM setup captures the deformation patterns and phase information, while the LDV setup measures the velocity and displacement of the membranes.

The Digital Holographic Microscope

To measure the deflections of membranes, DHM is employed. DHM is a quantitative phase microscopy technique that has been extensively used for various applications, including static and dynamic surface metrology, particle tracking, and the tracking and monitoring of live biological cells.

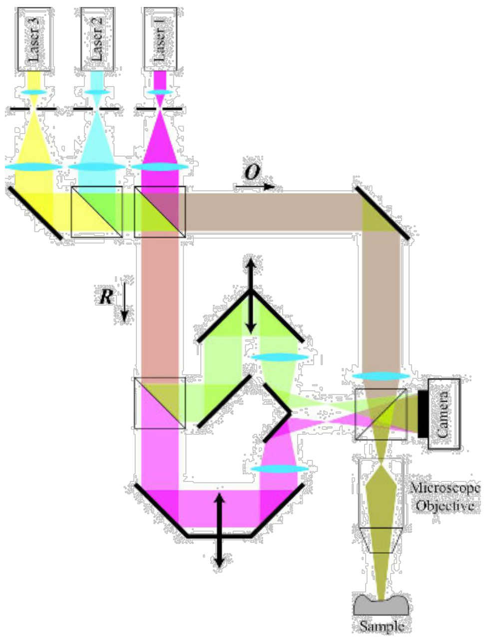

Figure 3.10: Basic optical configuration of DHM in reflection geometry to measure height profiles

DHM operates based on interferometric principles. A coherent, monochromatic light source is split into an object and reference beams. The object beam passes through an objective lens, interacts with the sample surface, and is reflected through the objective lens, where it recombines with the reference beam, as shown in Figure 3.10. The interferogram produced by the recombined object and reference beams is recorded as a 2D hologram on a charge-coupled device (CCD) camera. This hologram is a complex superposition of interferograms, each formed by a reflecting wave from a point on the object's surface and interfering with the reference wave. Consequently, the hologram contains all the phase and amplitude information of the specimen [48]–[51].

In digital holography, numerical reconstruction of the hologram produces a wavefront in an observation plane based on the recorded hologram intensity. This reconstructed wavefront consists of real and imaginary parts, from which two-dimensional images are generated: a 2D amplitude image, similar to conventional light microscopy, and a 2D phase image. Additional processing addresses aberrations and the sample surface's characteristics, such as tilt [52], [53]. The phase ϕ at a given pixel (ξ, η) in the image can be converted to height h as a function of the known wavelength λ and the refractive index [51], as shown in the following Equation:

$$h(\xi, \eta) = \frac{665.5651nm \times \phi(\xi, \eta)}{4\pi \times 1} \tag{3.6}$$

A labelled diagram of the instrument used in this project is shown in Figure 3.11,.

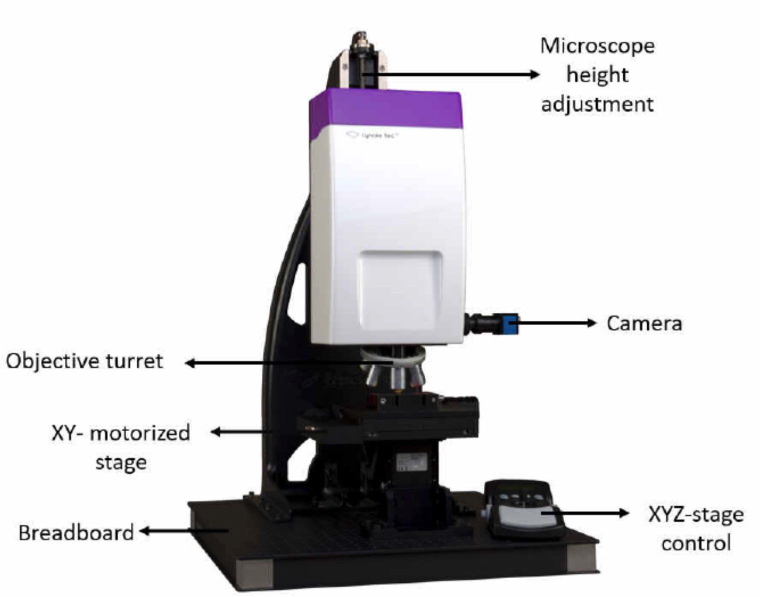

Figure 3.11: The LynceeTec DHM R2200

The instrument is capable of generating three different wavelengths ($\lambda_1 = 665.5651$ nm, $\lambda_2 = 793.2365$ nm, or $\lambda_3 = 681.0068$ nm) and can operate in either single-wavelength mode (λ_1 only) or dual-wavelength mode (λ_1 and λ_2 or λ_1 and λ_3). For our purposes, the single-wavelength mode sufficed to obtain the deflection profiles. Details of the objective lens employed in the DHM setup for this study are presented in the following table. 3.1.

Table 3.1: DHM objective lens details

Magnification	Lens Description	Lens Type	Numerical Aperture	Working Distance (mm)
2.5x	Leica N Plan 2.5x/0.07	Air	0.07	11.2

Lyncée Tec incorporates a software tool called Koala which is designed to analyze holograms obtained through DHM, enabling users to perform intensity and phase measurements on samples under observation. Koala includes additional functionalities that facilitate the extraction of deflection profiles from test specimens.

The intensity, phase, and holographic images of the sample under consideration are captured. The z-reference and flatness reference are set, and the phase is unwrapped. Subsequently, the piezo actuator is set to sweep through a range of frequencies, allowing the frequency graph to be obtained. This process enables zooming into specific resonance peaks and the reconstruction of their mode shapes.

Due to the small field of view (FoV) that can not encompass the entire filter, a stitching tool is employed to combine multiple images of the membrane. The detailed procedure for this process is provided in Appendix A.

The Laser Doppler Vibrometer

The Laser Doppler Vibrometer (LDV) uses the Doppler effect of a laser beam to measure vibrations in structures. A laser is emitted from the objective, strikes the sample, and is reflected in the system. The frequency or wavelength of the reflected light changes as a function of the sample's velocity, allowing the system to detect vibrations. Step-by-step procedure is provided in Appendix B.

The Doppler Effect:
Laser vibrometry leverages the Doppler effect to measure vibrations. When light is scattered from a moving object, its frequency changes. Piezo actuators are used to induce vibrations on the surface as shown in Figure 3.8a.

The acquisition process involves several detailed steps. First, the PSV Acquisition - Scan software is opened to initiate the setup. The laser beam must then be carefully aligned with the sample to ensure precise measurements. After alignment, a grid of points is defined on the sample, enabling accurate data collection across its surface. This grid setup is crucial for ensuring that measurements are taken uniformly and comprehensively.

Next, the measurement configuration begins with setting the analogue-to-digital (A/D) parameters, which are essential for converting the analogue signals from the vibrometer into digital data for analysis. The function generator settings are then adjusted to control the frequency and amplitude of the input signal, tailoring the test conditions to the specific requirements of the experiment. In the general tab, the type of measurement is defined, ensuring that all necessary parameters are correctly set for the specific type of analysis being conducted. Subsequently, bandwidth and Fast Fourier Transform (FFT) lines are configured in the frequency tab to optimize the resolution and accuracy of the frequency data. Finally, the measurement process is initiated by clicking the Scan button, which starts the data acquisition. This structured approach ensures comprehensive data acquisition for detailed vibrational analysis. Additional steps and detailed procedures are given in Appendix B.

Process of height measurement:

The DHM technique is highly effective for capturing high-resolution, three-dimensional topographic measurements of samples, though it does not directly represent z-axis heights. To address this, a MATLAB script is developed to automate the conversion of phase images into height displacement maps, offering a clear visualization of the data. This script processes the unwrapped phase data to generate a height map, effectively translating the phase shift information into topographical height measurements. The code is provided in Appendix C.

After initializing essential parameters, like the wavelength of light and the refractive index of air, a loop is employed to iterate through each phase image file. For each iteration, the script generates the appropriate filename and loads the corresponding phase image. The images are then downsized to a resolution suitable for processing. In the first iteration, the script initializes a 3D matrix to store the height maps for all images. The phase values, initially measured in nanometers, are converted to radians. Next, the unwrapped phase is converted to height displacement using the Equation 3.6. This computed height is stored for further visualization purposes to create height maps and generate videos of the height displacement data across the sequence of images, enabling dynamic visualization of the surface topography.

3.4.3. Comparison Methodology

Once both the experimental and simulation data are acquired, a detailed comparison between these datasets is conducted as the final phase of the study. This step is crucial for validating the accuracy of the computational models and for gaining deeper insights into the system's behaviour under study.

Basis for Comparison

- **Eigenfrequency value analysis:** A direct comparison is made between the eigenfrequency values obtained from the DHM, LDV, and COMSOL simulations. An exact match among these values would indicate a high degree of accuracy and reliability in both the experimental measurements and the simulation models.
- **Eigenfrequency ratio analysis:** In the instance where the eigenfrequency values do not align perfectly between the experimental and simulation results, a more nuanced approach is adopted, by comparing the ratios of the eigenfrequencies. This method allows the assessment of the relative differences between frequencies, rather than focusing solely on absolute values. These ratios are analyzed to get insights into the underlying patterns and discrepancies in the data. Additionally, various factors that may contribute to the observed deviations are considered, including experimental uncertainties, model assumptions, and material properties. Through speculation and the formulation of informed hypotheses, the differences are explained and our understanding of the system's behavior is refined.

The comparison of experimental and simulation data is undertaken to ensure that the findings are accurate and reliable, thereby providing a solid foundation for further research and development.

3.5. Conclusion of Membrane Simulation Methodologies

In conclusion, the methodologies outlined in this chapter provide a robust framework for exploring and validating Si_3N_4 and SiC membranes as LVFs. By systematically simulating the modal properties, stress distribution, and thermo-mechanical behaviour of these materials, and validating these models through experimental techniques such as DHM and LDV, an understanding of their suitability for space missions is ensured.

4 Simulation Results

This section provides a detailed overview and analysis of the simulation results achieved through the modelling approach. The use of COMSOL Multiphysics as the primary simulation tool allows for the comprehensive modelling of the membranes' structural dynamics and thermo-mechanical properties under various conditions, ensuring the reliability and accuracy of the simulations.

4.1. Overview of Simulation Approach

For seamless correlation, this chapter is systematically divided into two distinct sections: Simulation for Measurement and Simulation for Theory. This structure mirrors the approach taken in the COMSOL studies. The first section is dedicated to simulations that directly inform about subsequent measurements and validations, such as the eigenfrequencies of framed and unframed membranes. The second section, while primarily theoretical at this stage, establishes a foundation for future experimental validation. This theoretical component includes simulations involving the cooling of the membrane and frame to 50 K, the addition of a gold layer to the membrane, and the subsequent cooling of the membrane-gold system to 50 K. Across both sections, eigenfrequencies and mode shapes are examined alongside stress plots. This comprehensive approach not only ensures rigorous validation of the current work presented in this research but also strategically prepares for future experimental investigations.

4.2. Simulation for Measurements

In this section, the results of an eigenfrequency and mode shape analysis for a basic membrane model composed of Si_3N_4 are presented. Additionally, these findings are compared with those from a similar model made of SiC. To further our analysis, a silicon frame is also incorporated around the membrane. This comparative approach enables the assesment and differentiation of material properties across different configurations.

4.2.1. Results for Membrane-Only COMSOL Simulations

The Si_3N_4 Membrane

The base model used in the experiment is a membrane model of a square of Si_3N_4 with a side length of 20 mm and a thickness of 500 nm. The pretension force was 50 N/m. The constraint is a fixed constraint at the edges which leaves the displacement free in the z-axis.

This results in the following first six modes of the membrane. There might have been higher modes but this study is restricted to the first six, as they are the most critical modes with the highest amplitudes.

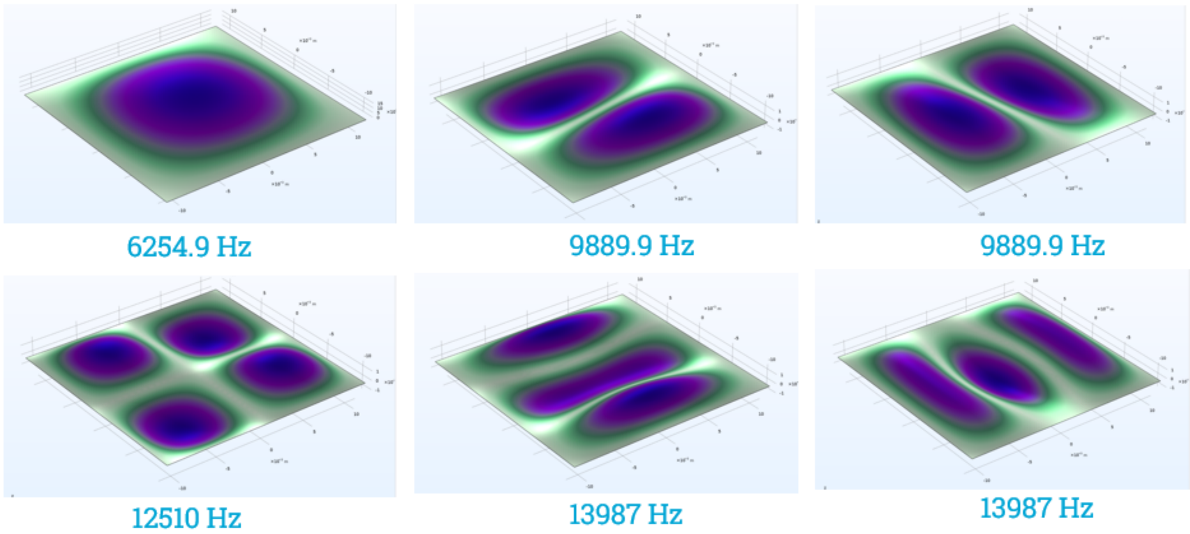

Figure 4.1: Mode shapes for silicon nitride for each eigenfrequency

The image shows six mode shapes of a square silicon nitride membrane with their corresponding natural frequencies in Hertz (Hz). Here is an analysis of these mode shapes:

First Mode (6254.9 Hz) The first mode shape shows a single central bulge, indicating a fundamental mode of vibration. This mode is characterized by the entire membrane moving in phase, with the maximum displacement at the centre.

Second Mode (9889.9 Hz) The second mode shape shows two bulges side by side along one axis. This indicates a mode with a single nodal line along one axis, dividing the membrane into two regions that move out of phase with each other. This mode is degenerate with the third mode due to both being at the same frequency.

Third Mode (9889.9 Hz) The third mode shape is identical in frequency to the second mode but shows two bulges along the orthogonal axis. This indicates a single nodal line along the other axis, similar to the second mode but orthogonal to it.

Fourth Mode (12510 Hz) The fourth mode shape displays four bulges, forming a checkerboard pattern. This suggests two orthogonal nodal lines dividing the membrane into four quadrants, each moving out of phase with its neighbours.

Fifth Mode (13987 Hz) The fifth mode shape shows two elongated bulges parallel to one axis. This suggests a mode with more complex nodal patterns, potentially two parallel nodal lines along one axis. This mode is degenerate with the sixth mode.

Sixth Mode (13987 Hz) The sixth mode shape is similar in frequency to the fifth mode but shows a different pattern, with elongated bulges along the orthogonal axis. This indicates two parallel nodal lines along the other axis.

The SiC Membrane:
Upon running the analysis with the material properties of SiC, while maintaining all other parameters constant, an increase in eigenfrequencies compared to those obtained with Si_3N_4 is observed.

This increase, though marginal, suggests that SiC could be a promising candidate for use as an LVF material. The higher eigenfrequencies align with the desirable performance characteristics for such applications. Furthermore, SiC's significantly higher ultimate tensile strength (UTS) of 12.04 GPa, compared to 0.4 GPa for Si_3N_4 indicates the potential to develop thinner yet stronger membranes. This combination of enhanced mechanical properties and improved dynamic performance makes SiC a compelling material choice for advanced membrane applications.

Si_3N_4 (Hz)	SiC (Hz)
6254.9	6350
9889.9	10040
9889.9	10040
12510	12700
13987	14200
13987	14200

Table 4.1: Side-by-side comparison of eigenfrequencies

Validation with Analytical Equation

To establish a foundational understanding of the vibrational characteristics of membranes, the formula for frequency by Blevin [37] is used. This formula provides a critical relationship between the geometrical and material properties of the membrane, enabling the prediction of eigenfrequencies based on key parameters such as side lengths, surface area, tension, and mass per unit area.

The formula for frequency as given in Blevin [37] is:

$$f_{ij} = \frac{\lambda_{ij}}{2}\sqrt{\frac{S}{\gamma A}}, \quad \text{and} \quad \lambda_{ij} = \sqrt{i^2\frac{b}{a} + j^2\frac{a}{b}}. \tag{4.1}$$

Here, a and b are the side lengths, A is the surface area, S is the tension per unit edge, and γ is the mass per unit area.

If the parameters used in the model are plugged in and a and b, and considered equal (square membrane), **an exact frequency match with the frequencies in Figure 4.1 is obtained**.

This validates the COMSOL model, with the equality between the calculated and simulated frequencies confirming the accuracy of the computational approach.

4.2.2. The Framed Membrane

As the next step for modelling, a frame is assigned to the model, 5mm wide on all sides with a thickness of 375 μm. The effects of this frame on the eigenfrequencies and mode shapes of the membrane are carefully evaluated.

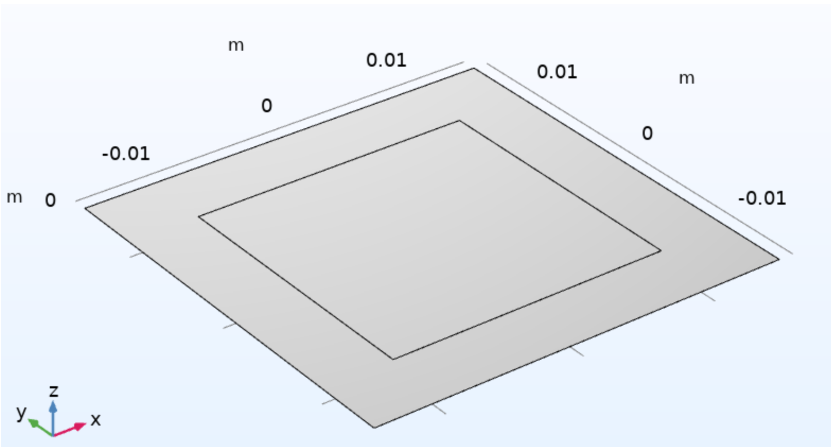

Figure 4.2: Membrane with frame

The frame is made of silicon as opposed to the previous Si_3N_4 material and is deposited on top of the membrane in a layered fashion. The properties of the material are derived from COMSOL's database.

The differential expansion or contraction between Si and Si_3N_4 is analyzed using guidance from the official COMSOL documentation [54]. Given the thin nature of the membranes, the sequence of layers in a multilayered structure is not explicitly considered in the analysis.

The investigation aims to assess whether the bending behaviour of a layered material where each layer has distinct mechanical properties could be accurately modelled. However, the membrane model employed in the simulation does not differentiate between the layers, instead it treats the composite structure as a uniform entity. As a result, this approach does not allow for the precise measurement of layer-specific bending, thereby limiting the ability to capture the effects of differential expansion or contraction in a layered membrane.

The final mode shapes with the frame are shown in Figure 4.3. The eigenfrequencies are the same as in the case of membrane-without-frame, and the mode shapes are similar.

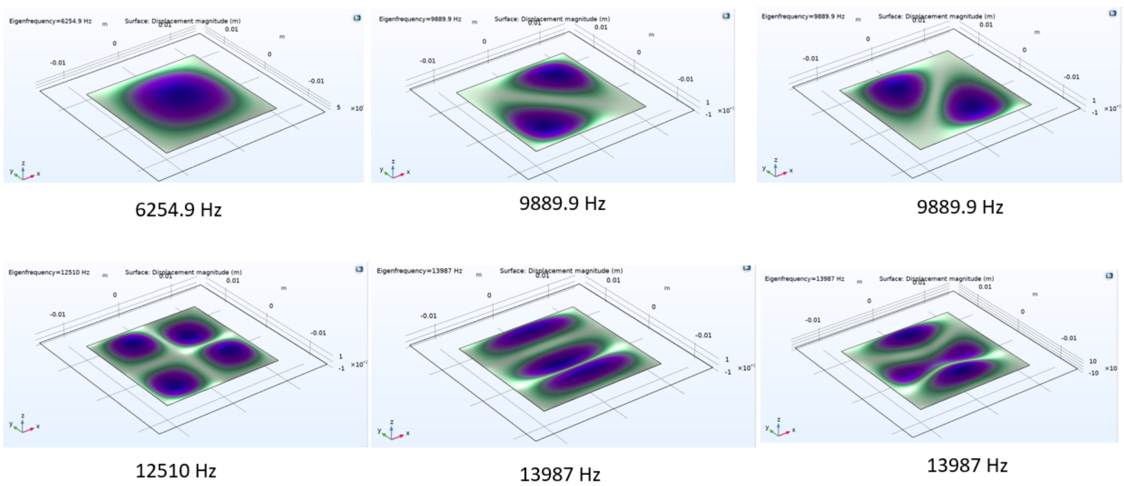

Figure 4.3: Mode shapes with the frame

Impact of Frame Addition on Degenerate Eigenmodes

In the COMSOL model of a membrane, the addition of a fully-fixed frame results in changes to the mode shapes. For example, a 45-degree rotation in the second and third modes is observed, while the frequencies remain similar.

Degeneracy of Eigenmodes:

This phenomenon can be attributed to the algebraic nature of the eigenvalue problem:

- The second and third modes of both the framed and frameless models share the same eigenfrequency.
- These eigenvalues have an algebraic (or geometric) multiplicity of 2, indicating degenerate eigenmodes.
- For degenerate modes, there is no unique solution. Any linear combination of the degenerate eigenvectors is also a valid eigenvector. If u and v are solutions, then $a \cdot u + (1 - a) \cdot v$ is also a solution for any a.

Numerical Method Dependence:

The specific mode shapes observed can vary depending on the numerical methods used, such as mesh refinement or solver algorithms. These methods determine which basis vectors within the degenerate subspace are identified, without altering the underlying physical properties.

In a previous case, changing the meshing sequence yields similar changes. For instance, if u is the first solution of the frameless model and v is the second, then in the framed model, the solution can be expressed as a linear combination. Specifically, for $a = 0.585$, the solution closely matches a mode shape from the framed model (see Figure 4.4).

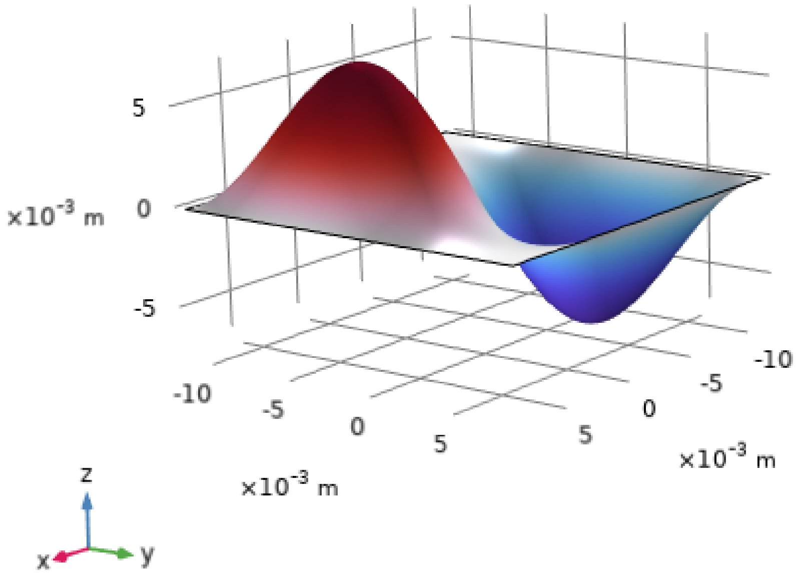

Figure 4.4: Mode shapes with the frame

The addition of a frame, though theoretically non-intrusive, influences the numerical representation of mode shapes due to the degeneracy of the eigenmodes. Thus, the 45-degree rotation in mode shapes is a result of different numerical representations of the same degenerate eigenmodes.

Stress Across the Whole Membrane

Based on the 3D cut line depicted in Figure 4.5, which spans across the entire membrane and frame system, the stress plots were as follows:

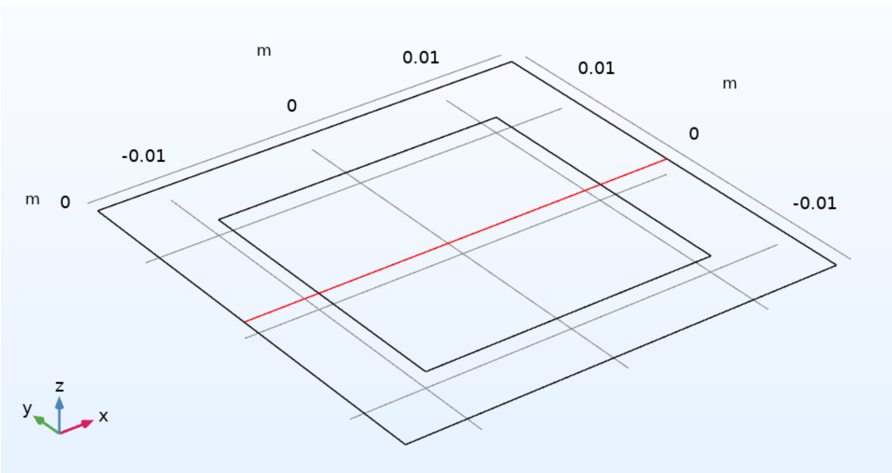

Figure 4.5: The cut line defined from [-1,0,0] to [1,0,0]

The stress plots are the same across all the eigenfrequencies of the membrane with the continuous value of $10^8 N/m^2$. The UTS of Si_3N_4 varies depending on the specific composition and processing methods used. However, typical values for the UTS of silicon nitride are generally in the range of 400 to 1000 MPa (0.5 to 1 GPa). The value of the stress is well within the ultimate tensile stress limit for Si_3N_4 [55].

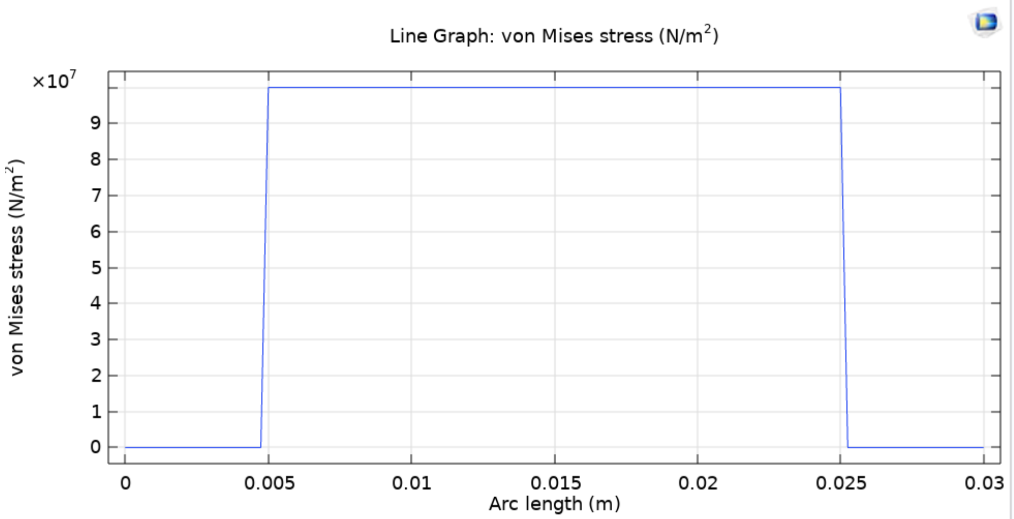

Figure 4.6: The stress profile

During an eigenfrequency analysis, the computed mode shapes represent the deformation patterns of the structure at various natural frequencies. The mode shapes are often normalized, which can make the stress distribution appear uniform across different modes. This normalization helps in identifying the characteristic deformation patterns without focusing on the actual stress magnitudes. Due to fixed constraints on the frame, the stress there becomes 0. When a fixed constraint is applied in a FEM, it prevents any displacement of the constrained region, effectively immobilizing the frame in this case.

However, it's important to note that while the stress within the frame is zero, the system still experiences reaction forces at the points where the constraints are applied. Although the frame itself is not deforming, it is still playing a crucial role in maintaining the overall equilibrium of the system. These do not show up in stress plots because stress plots in COMSOL, typically represent the internal stresses within the material, which are caused by deformation.

4.3. Simulation for Setting Up Theoretical Framework

This section outlines the results and methodologies related to the thermomechanical and damping analysis of $\mathrm{Si_3N_4}$ membranes with the addition of silicon frames and gold layers. The eigenfrequencies and mode shapes of these configurations are investigated, while paying particular attention to the effects of cooling. This approach helps ensure that the simulations provide a realistic representation of the membrane's behavior under varying conditions while also validating the computational models used in this study.

4.3.1. Thermomechanical Modeling

The analysis begins with a thermomechanical study, where the membranes are cooled and the changes in eigenfrequencies with the drop in temperature observed. Stress buildup due to differential thermal contraction between the silicon frame and the $\mathrm{Si_3N_4}$ membrane is also observed.

With the given rate of cool down:

$$T_0 = 293.15\,[\text{K}] - 2\,[\text{K/min}] \times t \tag{4.2}$$

, the following eigenfrequencies are obtained at every step of the process (for better understanding, only the plot from the first frequency is shown). The mode shapes remain consistent as per the previous studies.

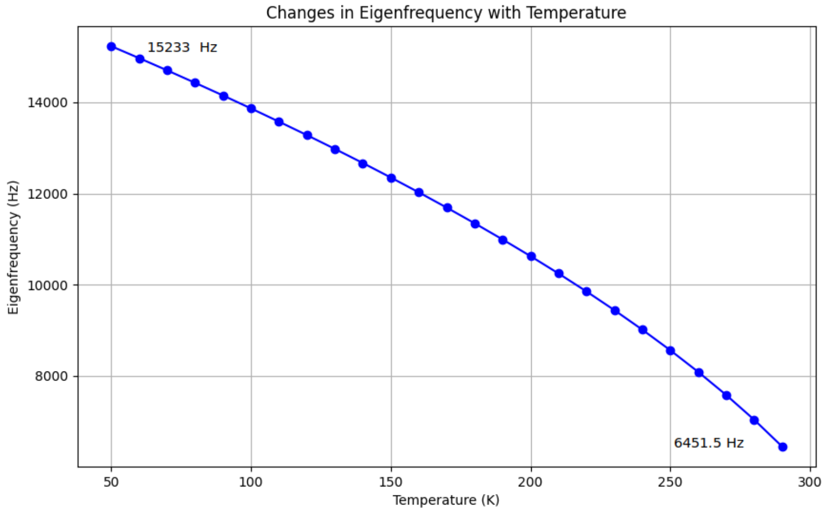

Figure 4.7: The first frequency wrt temperature

Due to cooling, the first eigenfrequency increases from 6 kHz to 15 kHz. As the frequency changes from 6 kHz to 15 kHz, the stress builds up due to cooling, so Si_3N_4 shrinks more than silicon due to the differences in their CTE. As Equation 4.2.1 suggests that eigenfrequencies are proportional to the square root of pretension in the membrane,

$$f_1 \propto \sqrt{S_1} \tag{4.3}$$

$$\frac{f_1}{f_2} = \sqrt{\frac{S_1}{S_2}} \tag{4.4}$$

Given:

$$f_1 = 6451.5\,\text{Hz}, \quad f_2 = 15233\,\text{Hz}, \quad S_1 = 10^8\,\text{N/m}^2$$

$$S_2 = \left(\frac{f_2}{f_1}\right)^2 \cdot S_1 = \left(\frac{15233}{6451.5}\right)^2 \cdot 10^8\,\text{N/m}^2 \approx 5.5 \times 10^8\,\text{N/m}^2$$

When comparing this calculated value with the observed value in Figure 4.9 of $3.8 * 10^8$, it becomes evident that the match is not exact. The following are the most likely reasons for this discrepancy:

1. **Method of Addition of Pre-stress**:
   - When analyzing thermal stress in the presence of a pre-stressed membrane, it's important to note that the addition of pre-stress is not purely mathematical. The pre-stress values are not treated as initial conditions in the traditional mathematical sense, but rather as a contribution to the constitutive relation of the material. As a result, in the thermal model, the pre-stress is integrated in a way that does not follow a straightforward mathematical addition, leading to a mismatch in the calculated frequencies [56].
2. **Interfacial Effects**:
   - The interface between Si_3N_4 and silicon may have interfacial stresses due to differential thermal contraction. These stresses can be complex and not fully captured by simple models, leading to inconsistencies.
3. **Model Approximations**:
   - The entire model is an approximation of the real physics of the membrane. Assumptions and simplifications made during modelling can introduce errors. For instance, the assumption of uniform temperature distribution or ideal material properties may not hold under all conditions.

4.3.2. Damping characteristics

In this section, a damping term into the COMSOL model is introduced, which, until now, has been formulated without considering damping effects. The objective is to investigate how the inclusion of damping influences the eigenfrequencies observed in the COMSOL simulations.

As observed in our previous analysis, the Q-factor appears to be infinity, indicating no damping in the membrane.

Eigenfrequency (Hz)	Damping ratio	Quality factor
15233	0.0000	Inf
14971	0.0000	Inf
14703	0.0000	Inf
14430	0.0000	Inf
14152	0.0000	Inf
13868	0.0000	Inf

Table 4.2: Eigenfrequencies without a damping term

To address this, a typical damping term is incorporated into the simulation model. This addition helps to better understand the damping characteristics and their impact on the membrane's behaviour.

Eigenfrequency (Hz)	Damping ratio	Quality factor
6254.9	5.0000E-7	9.9999E5
9889.9	5.0000E-7	1.0000E6
9889.9	5.0000E-7	1.0000E6
12510	5.4057E-7	9.2494E5
13987	5.6999E-7	8.7721E5
13987	5.7008E-7	8.7707E5

Table 4.3: Eigenfrequencies with a damping term

Incorporating Damping

The damping is represented by the damping coefficient c. According to literature, the Q-factor for broadband mid-infrared frequency comb generation in a Si_3N_4 micro-resonator is reported to be as high as 1×10^6 [57]. This Q-factor is used to estimate the damping ratio ζ which is then applied to the COMSOL models.

The Q-factor is related to the damping ratio by:

$$Q = \frac{1}{2\zeta} \tag{4.5}$$

Given $Q = 1 \times 10^6$:

$$\zeta = \frac{1}{2Q} = \frac{1}{2 \times 10^6} = 5 \times 10^{-7}$$

The damping term is included in the COMSOL model, and the simulations are rerun to observe its effect. The analyzed parameters include the changes in frequency and mode shapes resulting from the introduction of damping.

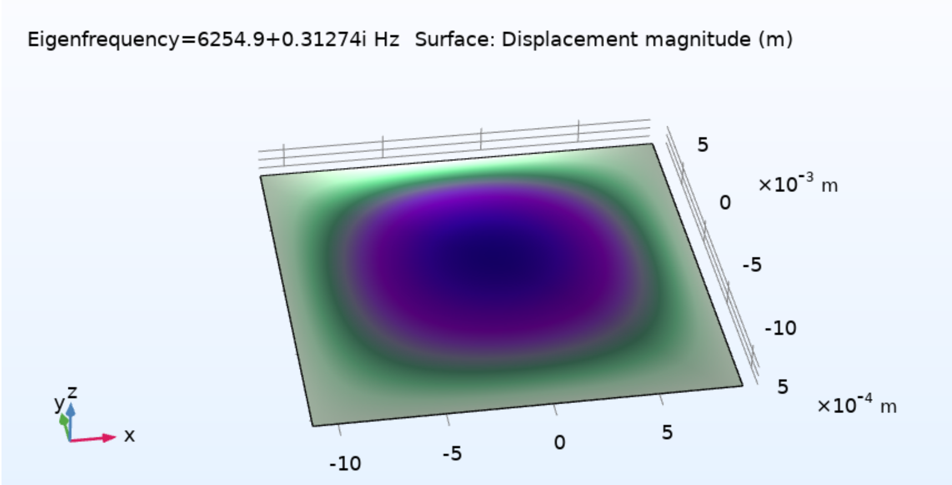

Figure 4.8: Effect of damping

Figure 4.8 illustrates the effect of damping in the model. It is observed for all modes that the same eigenfrequencies are obtained as without damping. Additionally, even with a higher damping term $Q = 1 \times 10^4$, the frequencies remain unchanged. This indicates that the natural frequencies of the system are not significantly affected by the added damping.

An imaginary part (0.31247i) is also observed in the damped eigenfrequencies. The complex-valued mode shape suggests that the phase angle provided information about the phase shift between different points in the structure during free vibrations. This means that if the displacements at two points have different phase angles, they would not reach their peak values simultaneously.

In most cases, the effects of damping on mode shapes and eigenfrequencies are marginal, likely due to the lack of actuation in the COMSOL models.

The Change in Stress On Cooling

Figure 4.9 shows that the stress increases linearly over time and with cooling. The maximum observed stress is 3.8×10^8 Pa, which remains well within the UTS of Si_3N_4 $(4 * 10^8 n/m^2)$ as reported by [55]. This indicates that the material can safely withstand the cooling process without the formation of cracks.

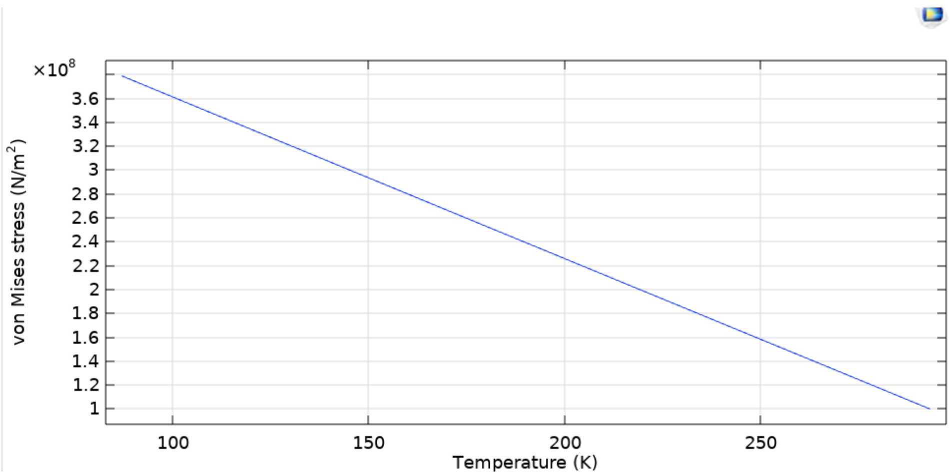

Figure 4.9: Stress vs Temerature

The relationship between thermal stress and temperature can be expressed using the following formula:

$$\sigma = E \cdot \alpha \cdot \Delta T \tag{4.6}$$

However, since the CTE (α) changes with temperature, α is considered as a function of temperature, $\alpha(T)$. The stress formula then integrates the effect of the temperature-dependent CTE over the temperature range:

$$\sigma(T) = E \cdot \int_{T_0}^{T} \alpha(T')\, dT' \tag{4.7}$$

To explain the linearity in the stress plot, the following needs to be checked:

1. If the change in CTE with temperature is small over the range of temperatures considered, the integral of $\alpha(T)$ might still approximate a linear function.

2. If Young's modulus E and the boundary conditions dominate the behaviour, it might linearize the response.

3. The overall thermal strain ϵ can be approximated as:

$$\epsilon = \int_{T_0}^{T} \alpha(T')\, dT' \tag{4.8}$$

In a situation where the variation in $\alpha(T)$ is minimal or approximately linear over the temperature range, the integral still results in a nearly linear function, thereby producing a linear stress response.

Simplified Case with Linear Approximation

If $\alpha(T)$ varies linearly with temperature as $\alpha(T) = \alpha_0 + \beta T$, where α_0 and β are constants, the integral becomes:

$$\epsilon = \int_{T_0}^{T} (\alpha_0 + \beta T')\, dT' = \alpha_0(T - T_0) + \frac{\beta}{2}(T^2 - T_0^2) \tag{4.9}$$

For small temperature ranges, the $\frac{\beta}{2}(T^2 - T_0^2)$ term might be negligible, leading to:

$$\epsilon \approx \alpha_0(T - T_0) \tag{4.10}$$

Thus, the stress:

$$\sigma(T) \approx E \cdot \alpha_0 \cdot (T - T_0) \tag{4.11}$$

This linear approximation justifies why the stress plot appears linear if the temperature-dependent variations of the CTE are not significant over the temperature range considered. To see a non-linear relationship clearly, the variation in $\alpha(T)$ would need to be substantial over the temperature range in question.

4.3.3. Eigenfrequency Model of a Membrane with a Gold Layer

In this section, the focus is on enhancing the Si_3N_4 membrane by adding a gold layer on top, followed by incorporating a silicon frame and cooling the membrane-gold layer system down to 50K. The addition of the gold layer has a significant impact on the eigenfrequencies, as the increased mass resulted in a reduction of the vibrational frequencies. This outcome is corroborated through both analytical calculations and COMSOL simulations.

The eigenfrequencies were lowered but the mode shapes remained consistent:

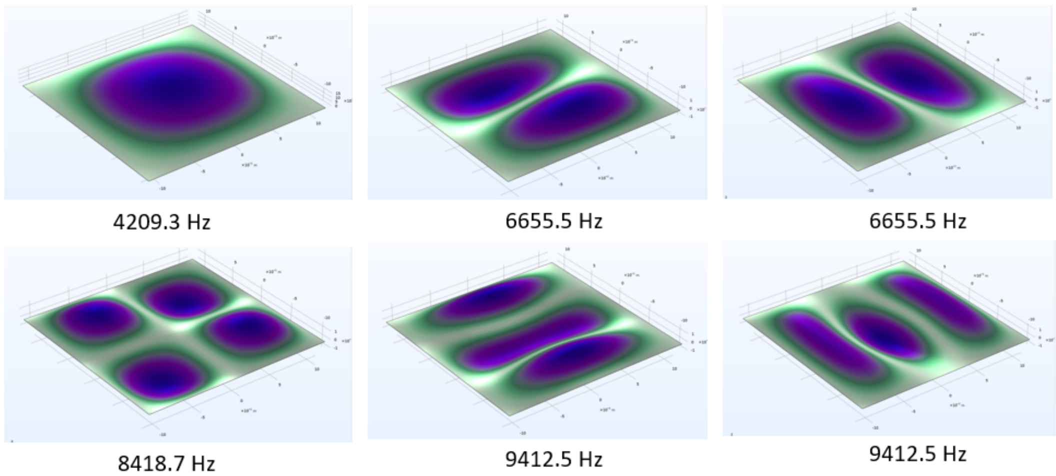

Figure 4.10: Eigenfrequencies with gold

Validation of COMSOL Model with Analytical Equation:

The goal is to compute the eigenmodes and eigenfrequencies for a 500 nm thick Si_3N_4 membrane with a 100 nm thick gold layer added on top of it. A comparison is made between the analytical results with those obtained from COMSOL, which show frequencies of 4209.3 Hz for the multilayer structure as opposed to 6254.9 Hz for the Si_3N_4 membrane alone.

For the original Si_3N_4 membrane, the fundamental frequency f_0 is given by:

$$f_0 = 6254.9 \text{ Hz}$$

When adding a 100 nm thick gold layer on top of the 500 nm thick Si_3N_4 membrane, the overall thickness increased. The mass per unit area of the membrane increases due to the added gold layer.

- $t_1 = 500$ nm is the thickness of the Si_3N_4 membrane.
- $t_2 = 100$ nm is the thickness of the gold layer.
- ρ_1 is the density of Si_3N_4.
- ρ_2 is the density of gold.

The mass per unit area for each layer is:

$$m_1 = \rho_1 \tag{4.12}$$

$$m_2 = \rho_2 t_2 \tag{4.13}$$

The total mass per unit area of the composite membrane is:

$$m_{\text{total}} = m_1 + m_2 = \rho_1 t_1 + \rho_2 t_2 \tag{4.14}$$

Assuming the pretension T in the membrane remains the same, the frequency of the membrane depends on the effective mass per unit area. The new frequency f_{new} is related to the original frequency f_0 by the ratio of the square roots of the masses:

$$f_{\text{new}} = f_0 \sqrt{\frac{m_1}{m_{\text{total}}}} = f_0 \sqrt{\frac{\rho_1 t_1}{\rho_1 t_1 + \rho_2 t_2}} \tag{4.15}$$

Using the known densities and thickness values:

$$f_{\text{new}} = 6254.9 \times \sqrt{\frac{1.5975 \times 10^{-3}}{3.5275 \times 10^{-3}}} = 6254.9 \times \sqrt{0.4528} \approx 6254.9 \times 0.6728 \approx 4209\,\text{Hz}$$

This proves that analytically the frequency obtained is the same as the COMSOL results. This also demonstrated the impact of increased mass on the vibrational characteristics of the membrane.

Gold-layered Eigenfrequency Model with a Frame

This methodology closely parallels the approach employed for the initial frame, with the steps being substantially similar. However, in this instance, the simulation model incorporates two-layered material links.

The material properties are kept consistent with those previously used, and the frame retained the same fixed constraints as in earlier configurations.

The mode shapes observed are analogous to those identified in previous studies, with the frequencies reflecting the modifications resulting from the addition of a gold layer to the membrane.

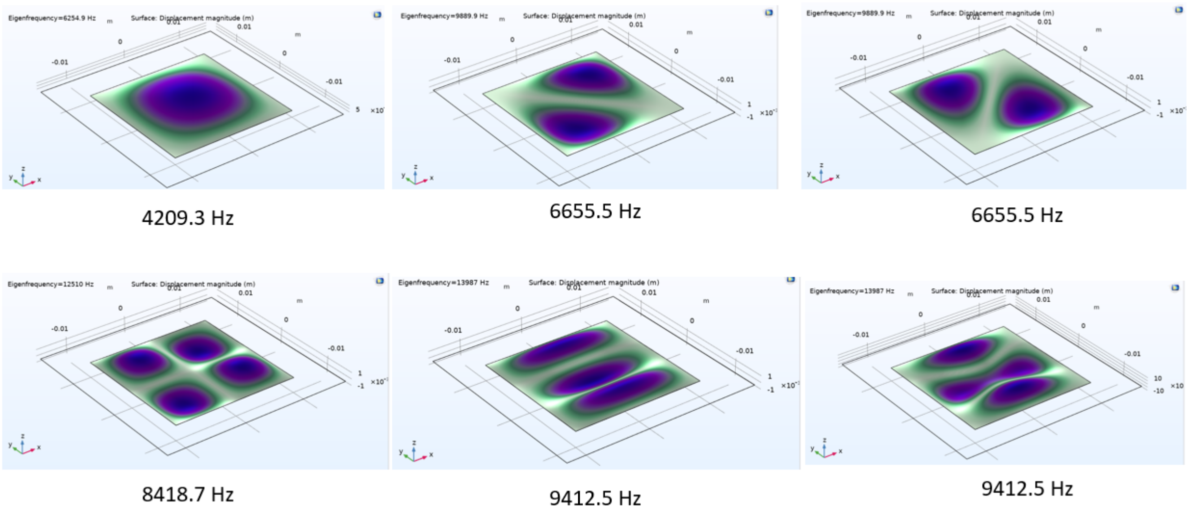

Figure 4.11: Eigenfrequencies with gold and frame

Cooling The System of Gold-Layered Membrane Down to 50K

This section aims to examine the changes in eigenfrequencies when the gold-coated membrane system was cooled down to 50 K. To verify the accuracy of the model, the results are compared with the initial and final frequencies obtained from the previous thermomechanical analysis involving the membrane and frame. While we anticipate that the rate of frequency change may vary due to the differences in the coefficients of thermal expansion (CTE) between gold and the membrane, the overall frequency values should remain within a comparable range, given that the same membrane material is being used.

The procedures and steps were identical to the previous processes but with the addition of gold as a material. The CTE values of gold were derived from MPDB software and inserted into the relevant equations. The stress plots and frequency plots were generated as follows:

Mode shapes remain consistent with the ones found with just the membrane and gold layer.

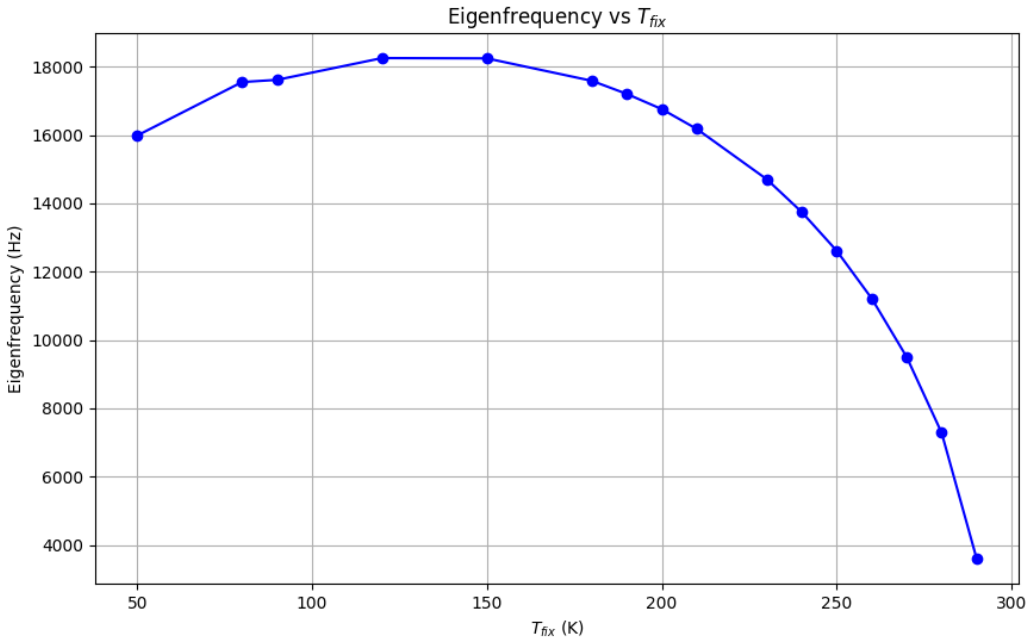

Figure 4.12: Variation of the first eigenfrequency with temperature (T_{fix}) as a plot

The range of eigenfrequencies observed when cooling the gold and Si_3N_4 system to 50 K closely aligns with the results from the Si frame layered on top of Si_3N_4. At 290 K, the frequency with the gold layer is approximately 3600 Hz, which falls within the expected range based on room temperature simulations involving the gold-coated membrane. The slight differences can be attributed to variations in pre-stress considerations. As the system cools to 50 K, the frequency increases to around 16,000 Hz, consistent with the trends observed in the membrane and frame model.

In summary, the initial rise in eigenfrequency is likely due to increased tensile stress from differential thermal contraction. The subsequent plateau and decrease may result from stress saturation, changes in material properties at low temperatures, and potential interfacial effects or residual stresses.

Temperature (K)	Eigenfrequency (Hz)
50.000	15987
80.000	17554
90.000	17618
120.00	18256
150.00	18247
180.00	17590
190.00	17206
200.00	16760
210.00	16180
230.00	14707
240.00	13747
250.00	12613
260.00	11217
270.00	9502.0
280.00	7281.4
290.00	3599.0

Table 4.4: Variation of the first eigenfrequency with temperature

The stress build-up observed during the cooling process can be primarily attributed to the factors discussed in Section 4.3.2. Notably, the stress plots for this configuration closely resemble those observed in the membrane and frame setup, highlighting the consistent impact of thermal mismatch on stress development. Despite these similarities, the maximum stress of $2.137 * 10^8 N/m^2$ remains well within the tensile stress limit of Si_3N_4, ensuring the material's integrity under the cooling conditions.

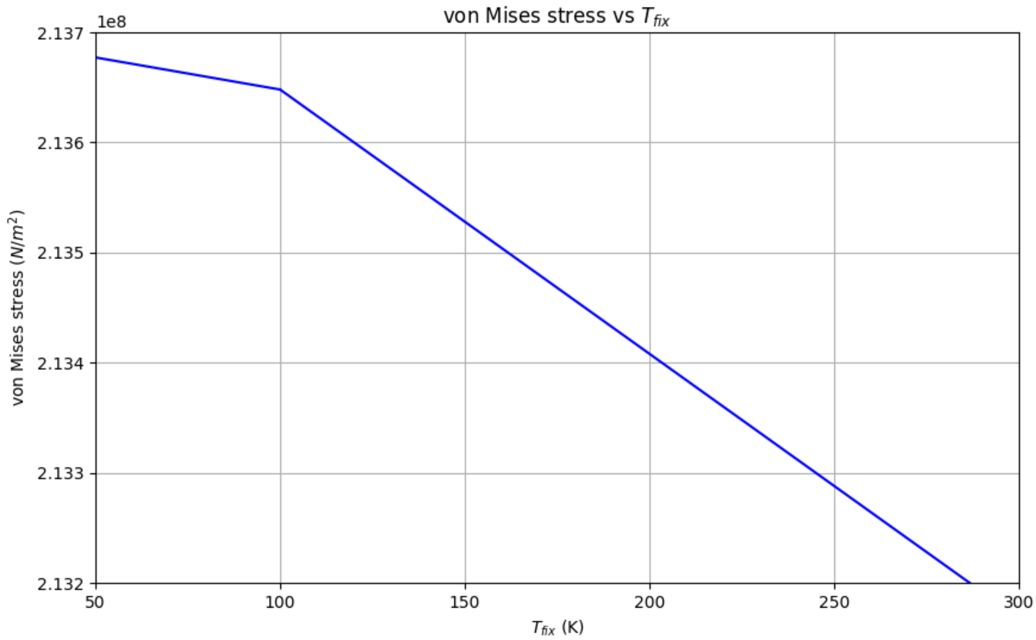

Figure 4.13: The stress build-up in the material due to cooling (around $2.137 * 10^8 N/m^2$)

The large CTE difference between Si_3N_4 and gold, for instance, leads to more pronounced stress fluctuations compared to the silicon-silicon nitride interface, where the materials have more compatible thermal behaviours.

4.4. Summary of Simulation Findings

In conclusion, the simulations performed using COMSOL Multiphysics provide crucial insights into the structural and thermo-mechanical behaviour of LVF membranes under different conditions. The comparative analysis between materials, as well as the inclusion of various configurations such as frames and layered structures demonstrates the versatility and effectiveness of the simulation approach.

- **Addition of Frame**: There was minimal change in the eigenfrequencies and mode shapes upon the addition of a frame.
- **Introduction of Damping**: The inclusion of a damping term did not significantly alter the eigenfrequencies, indicating that the natural frequencies of the system are robust against damping effects.
- **Cooling Process**: Cooling the system leads to an increase in both eigenfrequencies and stress levels, yet all values remain well within the material's safety limits, ensuring the membrane's structural integrity under thermal stress.

5

Experimental Results and Discussion

The detailed holographic images and phase information captured by the Lynceetec DHM are first examined, providing insights into the membrane's deflection profiles and mode shapes. This analysis is then followed by a thorough exploration of the vibration characteristics measured by the Polytec LDV, where the frequency response and displacement data are assessed.

5.1. The LynceeTec DHM R2200

The entire process and background behind the measurement calculations are detailed in Section 3. The approach involves performing a broad frequency sweep over a large range to identify frequency peaks. Once their positions are determined, the frequency range is narrowed down to find the exact eigenfrequency for resonance.

Mode shape acquisition is then carried out after zooming in on the first and second frequencies. The membrane is excited at these specific frequencies, and stitching is performed to capture the mode shape across the entire membrane.

An initial sweep from 4 to 15 kHz reveals several peaks in the frequency graph, as shown in Figure 5.1. This frequency range is selected based on an approximation from our preliminary COMSOL simulations.

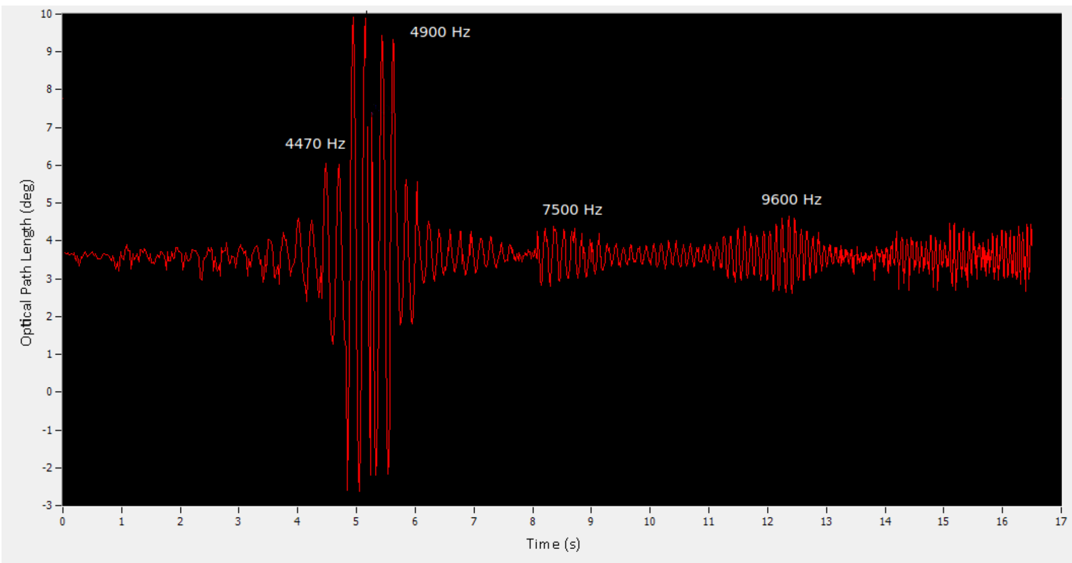

Figure 5.1: The frequency graph for our initial frequency sweep

Here peaks at around 4470 Hz, 4900 Hz, 7500 Hz, and 9600 Hz are seen. However, a good signal-to-noise ratio is obtained at two frequencies, since for the other frequencies, the obtained images are too noisy.

Table 5.1: Run 1: DHM measurement details

Magnification	Frequency	Signal	Offset	No of periods/frequency)	No of Samples/period
2.5x	4910 Hz	4V	2V	3	15

Table 5.2: Run 2: DHM measurement details

Magnification	Frequency	Signal	Offset	No of periods/fre)	No of Samples/period
2.5x	9570 Hz	4V	2V	3	15

Measurement Parameters:
After experimenting with various combinations of settings and configurations, the parameters that yielded the best results are identified. These parameters are chosen based on their ability to provide clear and accurate measurements, ensuring the reliability and consistency of our data. The chosen parameters reflect the most effective setup for capturing the behaviour and characteristics of the membranes under study.

Requirement of an Offset Voltage:
A 3V signal with a 1.5V offset is applied to our piezo actuator, yielding the best results. The offset voltage is crucial for several reasons:

Firstly, it helps avoid nonlinearity by keeping the actuator within a more linear response range, ensuring that the signal remains accurate and undistorted. Secondly, it maximizes the dynamic range of the actuator by utilizing its full potential, allowing for more effective excitation and measurement. Additionally, operating around a non-zero voltage significantly improves the signal-to-noise ratio (SNR), resulting in clearer and more reliable data. Finally, the offset enhances stability, providing better control and repeatability of the measurements, which is essential for consistent experimental results.

Advantages of Three-Period Averaging:
Using three periods per frequency yields clearer graphs, offering several key advantages. Improved signal averaging is achieved by averaging over three periods, which helps in reducing noise and producing cleaner data. This method also provides better frequency resolution, enabling a more detailed and precise frequency analysis, essential for identifying subtle features in the signal. Moreover, having more data points improves phase information accuracy, which is critical for understanding the behaviour of the membrane under different frequencies. Overall, this approach ensures a more comprehensive and reliable analysis of the frequency response.

Advantages of Fifteen Samples Per Period Rate:
Using fifteen samples per period produces good results, primarily due to the enhanced signal resolution it provides. More samples per period allow for finer details to be captured, ensuring that the nuances of the signal are accurately represented. This high level of sampling also ensures precise frequency analysis, which is crucial for identifying and characterizing the resonant frequencies of the membrane. Furthermore, having more data points results in better phase information, which is important for understanding the phase relationship between different parts of the signal. These factors combined make fifteen samples per period an effective choice for achieving detailed and accurate measurements.

Optimization of Input Signal for Accurate Mode Measurement:
Since the maximum amplitude change occurs in Mode 1 at the centre of the membrane, the membrane is excited at this location. For instance, with an example displacement of 10 nm and an amplification factor of 100, the final output becomes 1000 nm, which exceeds the wavelength of our laser. This necessitated experimenting with different input signal patterns to avoid exceeding the laser's wavelength and ensure accurate measurements. Consequently, an input signal of 3V with a 1.5V offset is found to provide a stable and effective signal pattern, minimizing disturbances and yielding reliable results.

5.1.1. Results of the DHM:

For visualization purposes, wrapped stitched phase image plots are preferred. At frequencies like 4910 Hz and 9570 Hz, distinct wrapped phase interference fringes are observed. These fringes illustrate the modal patterns and phase shifts across the membrane, offering insights into the dynamic response and deformation characteristics. The wrapped phase images are particularly useful as they allow for the examination of phase discontinuities and the identification of resonant modes. At 4910 and 9570 Hz, the wrapped phase interference fringes are seen as:

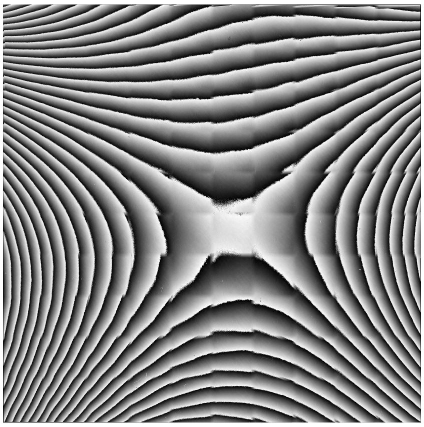

(a) Mode shape at 4910 Hz

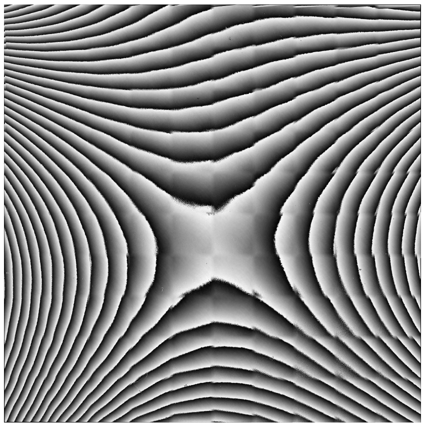

(b) Mode shape at 4910 Hz

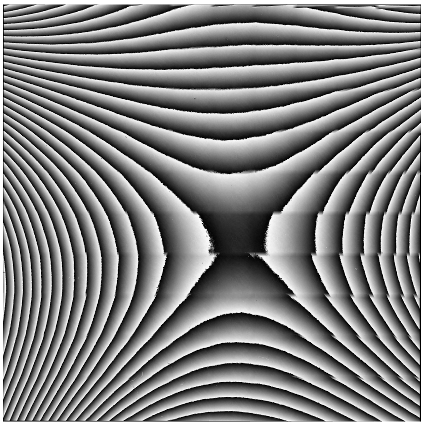

(c) Mode shape at 9570 Hz

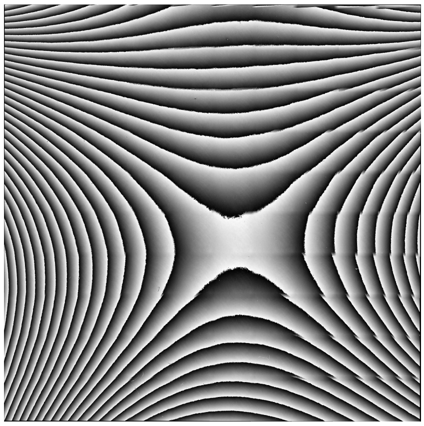

(d) Mode shape at 9570 Hz

Figure 5.2: The interference fringes

In Figure 5.2, a static image extracted from a video consisting of 45 frames is seen. This image displays an interferometric pattern representing mode shapes at 4910 Hz and 9570 Hz. Below is a detailed analysis of the phase density in different areas of the pattern:

1. **Center Patch:**
    - The white/black patch in the centre typically indicates a region of zero gradient of displacement.
    - In vibration mode shapes, this could represent a nodal point where there is no movement, while the areas around it show increasing displacement as you move away from the node.
2. **Dense Fringes At Corners:**
    - Areas with closely spaced fringes indicate regions with high displacement gradients.
    - This means the surface is experiencing rapid changes in displacement over a small area, suggesting areas of maximum vibration or deformation.

3. **Sparse Fringes:**
   - Regions where the fringes are spaced further apart indicate lower displacement gradients.
   - These areas are experiencing more uniform displacement with less variation over the surface.
4. **Symmetry and Pattern:**
   - The symmetry and specific patterns of the fringes can give insights into the mode shape of the vibration.
   - For example, the pattern in the image suggests a symmetrical mode shape around the centre, indicating the structure's natural frequency behaviour at 4910 Hz and 9570 Hz.

Upon close analysis of the videos, it is realized that at 4910 Hz, a gradual flow from left to right is observed, while at 9570 Hz, the central area exhibits expansion and contraction.

5.2. The Polytec LDV

The laser beam is directed at specific points on the membrane, and the reflected light is recorded to map out the vibrational patterns precisely. This approach provides a clear visualization of how the membrane deforms under different frequencies. The steps outlined in Section 3 are followed, and the following results are obtained:

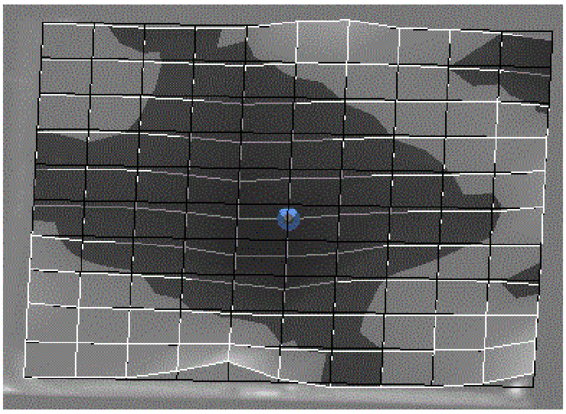

(a) Mode shape at 4340 Hz - start

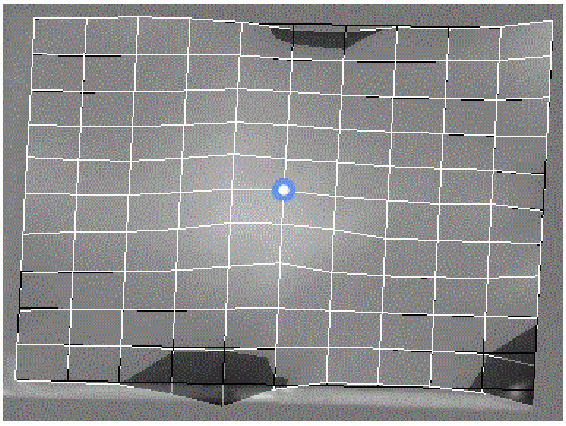

(b) Mode shape at 4340 Hz - end

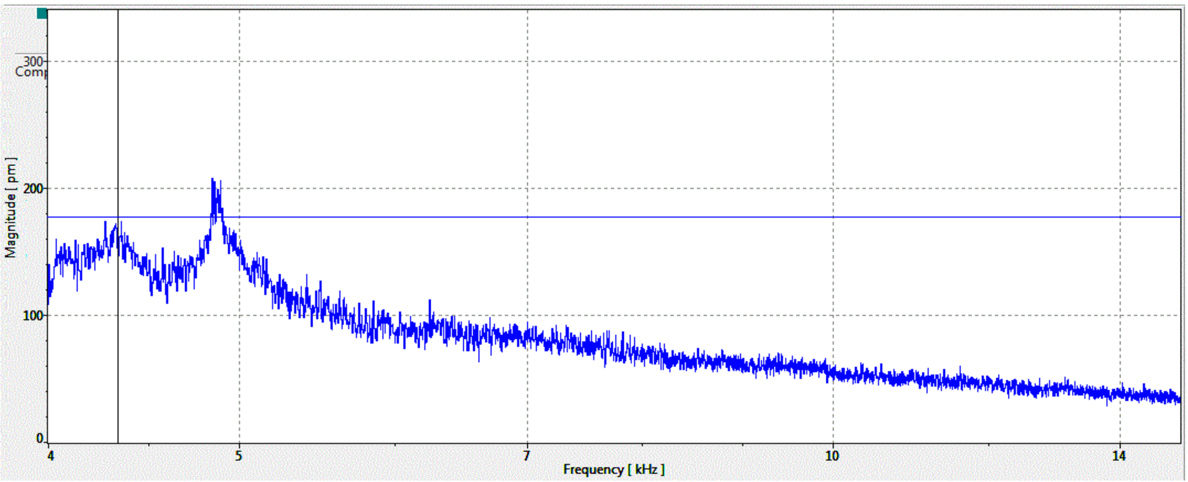

(c) Frequency graph at 4340 Hz

Figure 5.3: Frequency graph for the first observed eigenfrequency at 4340 Hz

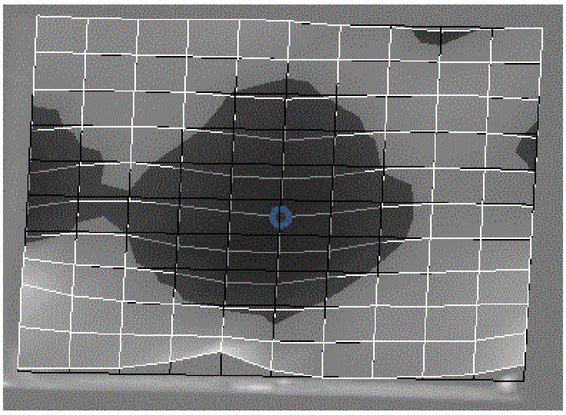

(a) Mode shape at 4859 Hz - start

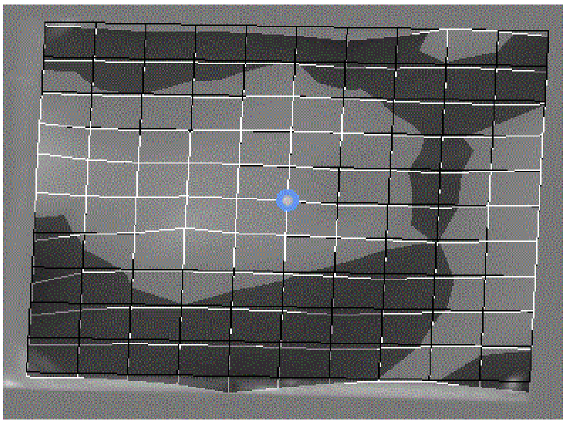

(b) Mode shape at 4859 Hz - end

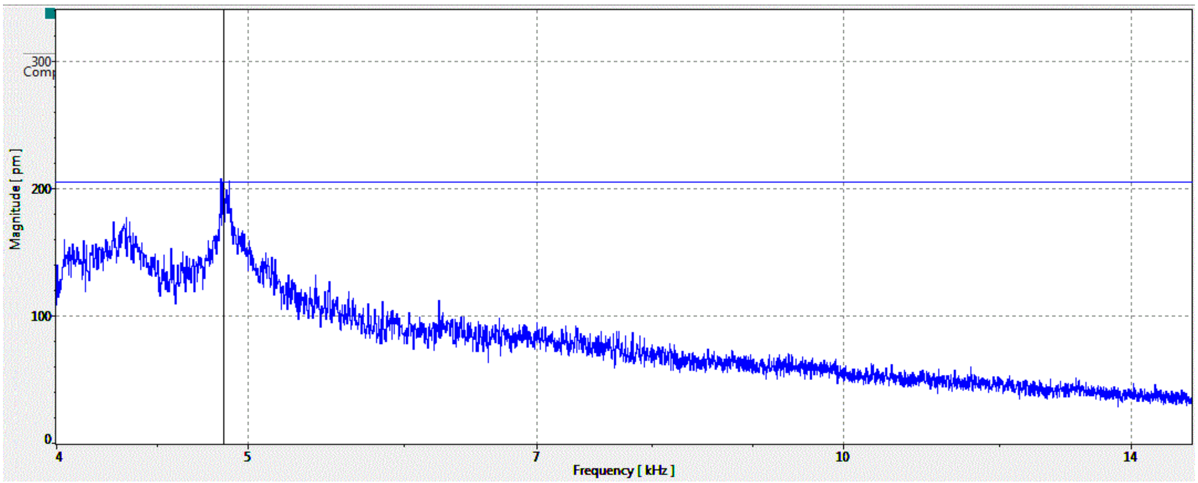

(c) Frequency graph at 4859 Hz

Figure 5.4: Frequency graph for the second observed eigenfrequency at 4859 Hz

However, the reflectivity of the sample is very low, which introduced significant noise into the measurements and required extensive averaging to resolve the peaks. Despite this challenge, persistent mode shapes are consistently observed at 4340 Hz and 4859 Hz.

5.3. Comparison

The following table summarizes the frequencies obtained from each instrument vs the COMSOL simulations:

COMSOL	DHM	LDV
	4400 Hz	4306 Hz
6254.9 Hz	4910 Hz	4859 Hz
9889.9 Hz	7500 Hz	
12510 Hz	9570 Hz	

Table 5.3: Frequencies observed through the DHM and LDV, compared with the COMSOL eigenfrequencies

5.3.1. Validation of DHM Frequency Ratios with Theoretical Predictions

According to theoretical calculations, the ratio between the third and first mode frequencies (12510 Hz and 6254.9 Hz) is approximately 2.00 $\left(\frac{12510\,\text{Hz}}{6254.9\,\text{Hz}} \approx 2.00\right)$. In the experimental results, the ratio between the frequencies 9570 Hz and 4910 Hz is approximately 1.95 $\left(\frac{9570\,\text{Hz}}{4910\,\text{Hz}} \approx 1.95\right)$, closely matched this theoretical ratio. This similarity suggests that the first and third frequencies are likely observed in the experiments.

Additionally, the peak observed in the sweep graph around 7500 Hz falls between the 4910 Hz and 9570 Hz peaks. This peak corresponds well with the ratio between the 9889.9 Hz and the 6254.9, indicating the presence of a second mode. While this second mode is not directly captured, its presence in the sweep graph suggests that the experimental setup is sensitive enough to detect its influence.

This finding suggests that while our experimental setup may have limitations in capturing all modes directly, the overall trends and frequency ratios observed align well with theoretical expectations, providing confidence in our modelling and measurement approaches.

5.3.2. Validation of LDV Frequency Ratios with Theoretical Predictions

In the frequency graph, two significant peaks are observed: one at 4859 Hz and another at 4306 Hz. The mode shape observed at 4859 Hz closely resembled the first mode shape shown in Figure 4.1. The eigenfrequency observed is also very close to the frequency observed with the DHM in the previous section (around 4910 Hz), with an error margin of approximately 1%.

The other peak at 4306 Hz appears to be significantly affected by edge effects (which refer to the distortions or irregularities near the edges of the membrane) in the membrane, making it harder to detect. This peak corresponds to the small peak observed in our frequency graph in Figure 5.1, which is around 4400 Hz. The mode shape at this frequency is difficult to detect due to pronounced edge effects.

A prominent vibration of the membrane edge, where it is connected to the frame, is also observed. This vibration significantly influences the overall behaviour of the membrane, particularly at the edges, where the mode shapes become more challenging to interpret and detect accurately.

5.4. Discussion

This section introduces the methodologies employed to measure the flatness of the membrane and examine the edge effects that can arise during experimentation. Flatness measurements are critical in determining the initial condition of the membrane, particularly when assessing its uniformity and structural integrity without actuation. Additionally, the edge effects are explored to understand how these factors may influence the overall behaviour of the system.

5.4.1. Flatness Measurement

Flatness measurements are crucial for assessing the structural integrity and initial conditions of the membrane before any actuation is applied. This analysis provides insight into the membrane's uniformity and alignment within the experimental setup. Upon conducting flatness measurements on the membrane without actuation, the following results are obtained:

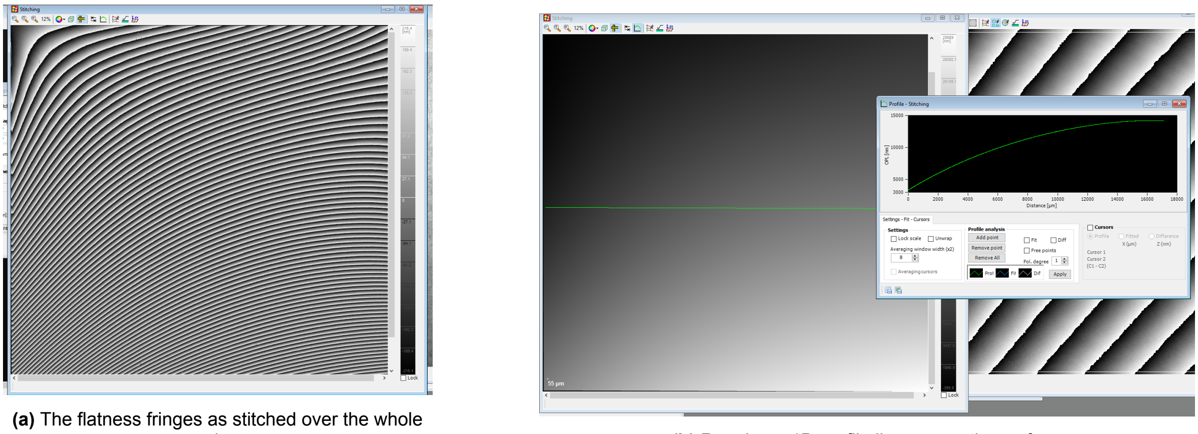

(a) The flatness fringes as stitched over the whole membrane

(b) Running a 1D profile line across the surface

Figure 5.5: Flatness measurements

Ideally, straight lines should be seen in any direction, indicating a uniform rigid body frame angle concerning the beam. However, bent lines are observed in this image, suggesting the bending of the membrane. Here, the reference is the frame of the membrane.

From the top left corner of the image, it can be seen that the fringes are asymmetrical and bent, indicating that this corner of the membrane is either higher or lower than the other corners. Therefore, the clamping of the frame is not done properly or the reference frame in this situation is not flat. Additionally, the presence of dust might also have an influence. Also, the membrane might be bent due to gravity. Given these observations, further measurements on the membrane with the frame would not yield significant results, as the system stands compromised.

5.4.2. Edge Effects and Discussion

Edge effects refer to the distortions or irregularities that occur near the edges of the membrane, particularly where it is attached to a frame. These effects are often caused by improper or uneven clamping of the frame, which can lead to several issues that affect the membrane's behaviour and performance.

When the clamping is poor, the frame holding the membrane may start to deflect or warp affecting the membrane. Ideally, the membrane should be uniformly stretched, with consistent tension, to maintain a flat and stable surface. However, if the clamping is not perfectly even, membrane edges—can experience variations in tension. This can lead to localized bending, wrinkling, or even buckling of the membrane, as depicted in Figure 5.6, which illustrates significant deformation in the frame (here, absorber) edges in contrast to the more stable membrane at the centre.

It can also significantly distort the membrane's mode shapes and vibrational characteristics. This distortion complicates the accurate measurement and prediction of the membrane's behaviour, as additional variables are introduced into the analysis like localized stress concentrations, irregular deformation patterns, and unexpected resonant frequencies. This not only degrades the membrane's optical and mechanical properties but also undermines the reliability of experimental measurements, as the reference frame is no longer stable.

When comparing Figure 5.6 with the DHM results in Figure 5.2, it is observed that the static pattern in the centre of the DHM measurements remains consistent. In both cases, the neutral (or 0) line forms a cross-like shape, indicating a correlation between the two sets of results. Furthermore, on comparing this with Figure 5.4 and Figure 5.3, it is noted that the edge midpoints exhibited a large deflection, highlighting the significant deformation occurring at these points.

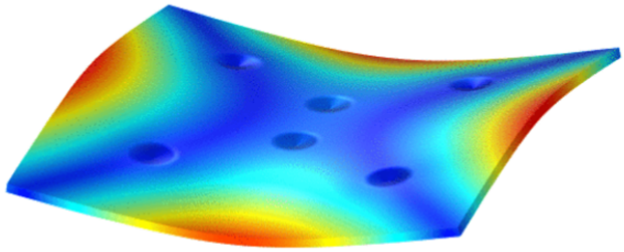

Figure 5.6: Motion in the frame (Sourced from SRON repository, Lynceetec challenge)

Therefore it is concluded that the current hardware setup does not fully align with our COMSOL model. The aim is to simulate non-uniform clamping, where the outer edge of the frame is mostly fixed, but the surface and inner edges are not. Our original COMSOL analysis used a fully fixed boundary condition, which was inaccurate. A new model was created where the frame is not entirely fixed, as shown in Figure 5.7 However, this model still doesn't accurately represent our hardware, since it fully fixes the frame's edges while allowing the membrane surface to move. Ideally, a partially fixed boundary constraint is needed, but the membrane interface in COMSOL doesn't allow for fixing one side while letting the other move freely. For these conditions, the solid mechanics interface would be more appropriate.

This issue may stem from the use of tape for clamping, which leaves the Si frame not fully constrained, making it part of the overall dynamics of the LVF and affecting both the membrane and the frame. Also, the LDV results reveal that the top and bottom edges move out of phase, a behaviour largely attributed to the mounting method. Tape provides inadequate local support, leading to nonlinearities in the system.

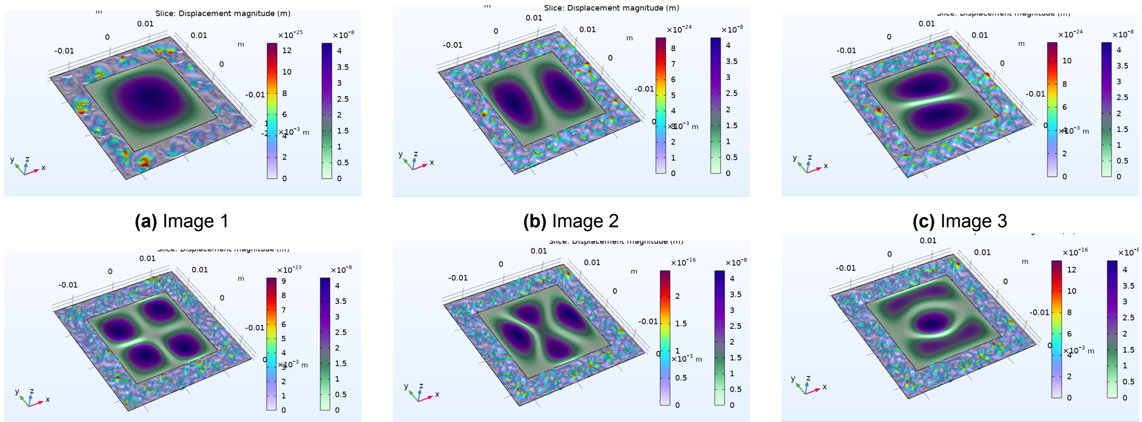

(a) Image 1 **(b)** Image 2 **(c)** Image 3

(d) Image 4 **(e)** Image 5 **(f)** Image 6

Figure 5.7: Frame fixed at the edges, but the surface is allowed to move

The flexibility in the frame can cause the piezo actuators to induce unintended vibrations or deformations in the frame itself, rather than solely affecting the membrane as intended. If the amplitudes of all four piezo actuators are not perfectly synchronized, this could result in uneven forces on the frame, further contributing to its movement and potentially leading to inaccuracies in the measurements or behaviour of the LVF system. Additionally, discrepancies in the piezo actuators, such as varying amplitudes or phase lag, may aggravate these issues, further complicating the system's dynamics.

5.5. Height Coding in MATLAB

A MATLAB code is developed, detailed in Appendix C, to calculate the precise mode shapes from the unwrapped phase images and create animations from them, mimicking the animations generated by the LDV. Through this process, a significant upward tilt at the edges of the frame is observed, which strongly confirms the presence of edge effects that have been identified in previous analyses.

Consequently, the height and the overall mode shapes cannot be accurately determined, as these edge-induced distortions introduce considerable inaccuracies into our measurements. This observation is consistent with our earlier findings and underscores the challenges posed by non-uniform clamping and frame movement in accurately capturing the membrane's behaviour.

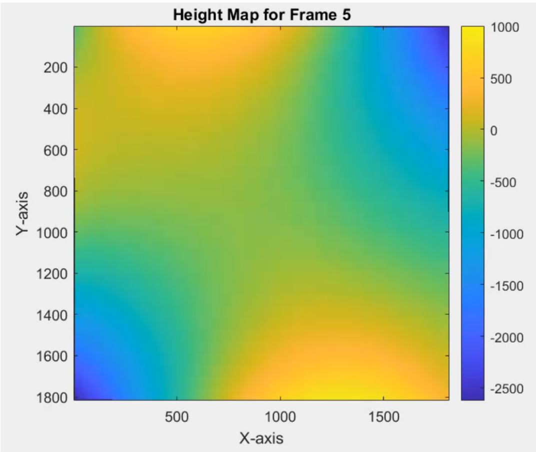

(a) Height map showing the improper clamping of the membrane around the edges

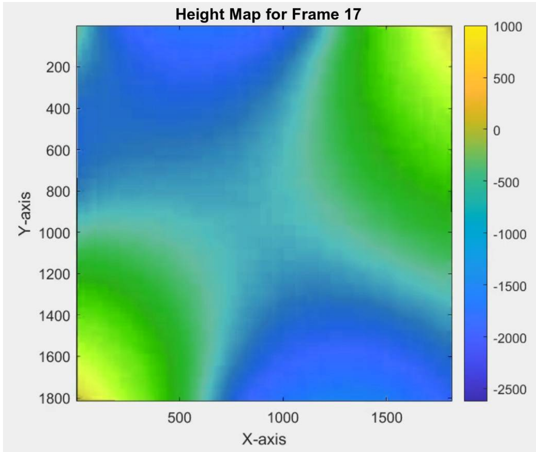

(b) Flipped colour profiles representing movement in the edges

Figure 5.8: Two frames from a height animation

5.6. Summary of Measurement Results

Therefore, it is evident that by systematically analyzing the data from each instrument, meaningful conclusions can be drawn that reinforce the accuracy of the simulations. This chapter not only validates the models but also contributes to the refinement of LVF designs, ensuring their robustness and reliability in practical applications.

6 Conclusion

This thesis explored the feasibility and performance of Si_3N_4 and SiC thin membranes as LVFs for FIR applications in space optics. The research addressed the thermo-mechanical challenges posed by the space environment, characterized by extreme temperatures and radiation.

The study began by highlighting the potential advantages of using thin membranes in LVF solutions, focusing on their optical performance and mechanical stability. A comprehensive approach was taken, combining FEM simulations with experimental validations to develop and analyze material-based models using COMSOL Multiphysics. The simulations considered factors such as geometry, pre-stress, and material properties to predict the behaviour and performance of LVFs under space-like conditions.

Experimental validations were conducted using DHM and LDV, providing precise measurements to verify the simulation models and ensuring their accuracy and consistency.

6.1. Key Findings

1. **Material Feasibility:** Both Si_3N_4 and SiC membranes demonstrated suitable mechanical stability under the expected operational conditions. Their thinness and inherent pre-stress make them promising candidates for LVF applications in space. Additionally, the frequency ranges for these materials were high enough to ensure low amplitudes in the filter membranes, further enhancing their suitability for precise and reliable operation in space environments.
2. **Thermo-Mechanical Behavior:** The differential thermal expansion between Si and Si_3N_4 was addressed through careful design and modelling. Simulations indicated that the stress buildup due to cooling from 290K to 50K was within acceptable limits, ensuring the structural integrity of the membranes. However, due to limitations in the membrane model in COMSOL, we could not conclusively determine the stresses between the membrane and frame materials. Despite this, no visible signs of warping were observed in the system.
3. **Mode Shapes and Frequencies:** While the experimentally determined mode shapes and frequencies did not perfectly align with the modelled shapes, mainly due to clamping issues and persistent edge effects, the frequency ratios between the simulations and experiments were consistent. This consistency suggests potential accuracy in the models, and all frequencies fell within acceptable limits, ensuring the LVF's capability to withstand the initial rocket frequencies.
4. **Edge Effects:** The modes observed are a complex mix of the membrane's inherent mode shapes and the influence of improper frame clamping. To improve the accuracy and reliability of our measurements, it is crucial to enhance the mounting method. Providing better and more uniform support will help minimize non-linear effects, allowing for a clearer and more accurate understanding of the membrane's vibrational behaviour. The inconsistency in support leads to pronounced edge effects, where distortions or irregularities occur near the clamped edges of the membrane.

6.2. Implications for Spaceborne Optical Instruments

The findings of this research contribute significantly to the development of robust LVFs for spaceborne optical instruments. By demonstrating the feasibility of using Si_3N_4 and SiC thin membranes and addressing the thermo-mechanical challenges, this work lays the foundation for future advancements in space optics.

The research provides insights into the material selection and design considerations necessary for LVFs to perform reliably in the environment of space. The successful modelling of the differential thermal expansion between Si and Si_3N_4 ensures that these materials can maintain their structural integrity under extreme temperature variations, which is a critical requirement for space applications. Additionally, the detailed analysis of mode shapes and frequencies confirms that these membranes can withstand the vibrational stresses encountered during launch and operation, making them viable candidates for integration into next-generation spaceborne optical systems.

Moreover, the identification of edge effects and the challenges associated with clamping highlight the importance of precise mounting techniques in the fabrication of LVFs. By addressing these challenges, future designs can achieve higher accuracy and reliability, ultimately improving the performance of spaceborne optical instruments. The methodologies and findings presented in this research provide a robust framework for continued exploration and refinement, guiding the development of more advanced, durable, and high-performance LVFs for use in demanding space environments.

7

Recommendations

Throughout this study, several challenges and limitations were encountered, particularly in the measurement process. The accuracy and reliability of the measurement techniques were impacted by factors such as edge effects, clamping issues, and reflectivity of the materials. These limitations influenced the precision of the results and the conclusions drawn from them.

7.1. Possible improvements

7.1.1. For the Clamping

Mitigating edge effects is crucial for obtaining accurate measurements.

- **Improved Clamping Stability:**
  - Placing a plate above the chip and secure it with a thicker plate that has a precisely positioned hole over the membrane.
  - This setup would be compatible with the laser vibrometer and significantly enhance clamping stability, reducing undesired vibrations and edge effects.
- **Use of Cyanoacrylate Adhesive:**
  - Carefully applying cyanoacrylate adhesive around the rim and allow it to set on the mount.
  - This process must be executed with caution to avoid damaging the actuator surface.
  - Properly fixing the rim could minimize its influence on the membrane's behaviour during measurements.
- **Placement of Counterweights:**
  - Placing counterweights on the rim to improve clamping efficacy by balancing the forces acting on the membrane.
  - Experimenting with different counterweight configurations might provide insights into optimizing this approach for various setups.
- **Exploring Gravity Effects:**
  - Conducting experiments with the membrane oriented parallel to the gravitational force to eliminate gravity-induced deformation.
  - This approach requires careful alignment and calibration but holds significant promise for improving measurement precision.

7.1.2. For the Piezo Actuator

To enhance piezo actuation accuracy, it is essential to rigidly couple the piezo actuators to the frame, minimizing unintended vibrations and deformations. Ensuring perfect synchronization among the four piezo actuators is crucial, as discrepancies in amplitude or phase lag can cause uneven forces, leading to frame movement and measurement inaccuracies. Implementing a precise control system and calibrating the actuators (e.g. adjusting the driving signals to compensate for differences in actuator response) to account for inherent variations will help equalize forces and reduce these issues, resulting in a more stable LVF system and improved measurement accuracy.

7.1.3. For the Reflectivity

Enhancing the reflectivity of the membrane surface is essential for improving the quality of measurements obtained through LDV. One effective method is to apply a thin layer of gold on top of the membrane. Gold's excellent reflective properties would increase the signal strength and accuracy of the LDV measurements. This modification should be performed with precision to ensure uniform coverage without adding significant mass or altering the membrane's mechanical properties.

7.1.4. Assumptions made in COMSOL

The membrane model, while computationally efficient, is insufficient on its own due to its inability to account for bending stiffness. However, by modifying the solid mechanics module to operate within certain constraints, these limitations can be overcome.

7.2. Future Directions

7.2.1. Experimental Realization of Theoretical COMSOL Models

A significant future direction involves the experimental realization of the theoretical COMSOL models developed in this research. To validate these simulations, a systematic approach can be undertaken where the actual membrane systems are subjected to controlled cooling down to 50 K. This can be achieved using advanced cooling techniques such as liquid helium cryostats, which allow for precise temperature control and uniform cooling of the system. These steps will not only confirm the validity of the COMSOL models but also provide deeper insights into the practical challenges of fabricating and testing LVF membranes under extreme conditions.

7.2.2. Advancing SiC Filter Fabrication Techniques

Another crucial direction for future work is the development of a robust SiC filter. Although SiC was identified as a promising material for its high eigenfrequencies and superior mechanical properties, the practical fabrication of SiC membranes has proven to be challenging. Attempts to produce SiC membranes were unsuccessful, as the membranes consistently broke during the fabrication process.

To overcome these difficulties, it is essential to refine the fabrication recipe to enhance the robustness of the SiC membranes. This may involve optimizing deposition parameters, improving etching techniques, or exploring alternative fabrication methods that can better accommodate the mechanical properties of SiC. By developing a reliable method to produce SiC membranes, future research can proceed with the planned eigenfrequency studies and fully explore the potential of SiC as a material for LVF applications.

7.2.3. Resonant metal mesh structures

One promising avenue for future research is the integration of resonant metal mesh structures into super-thin membranes to enhance the optical performance of LVFs.

The physical principle behind resonant metal-mesh structures involves their capacitive and inductive properties, which form a resonant LC circuit for incoming electromagnetic waves. A capacitive grid tends to perform a low-pass operation, while an inductive grid performs a high-pass operation. When combined in a resonant structure, they allow for selective filtering at specific frequencies.

As per Figure 7.1:

- **Length of element (K)**: The length of the cross elements in the mesh. It affects the mesh's interaction with magnetic fields, influencing its permeability. Longer elements can create inductive effects, similar to inductors. Adjusting K changes the inductive properties of the mesh. This can shift the resonant frequency and affect the filter's ability to select specific wavelengths.

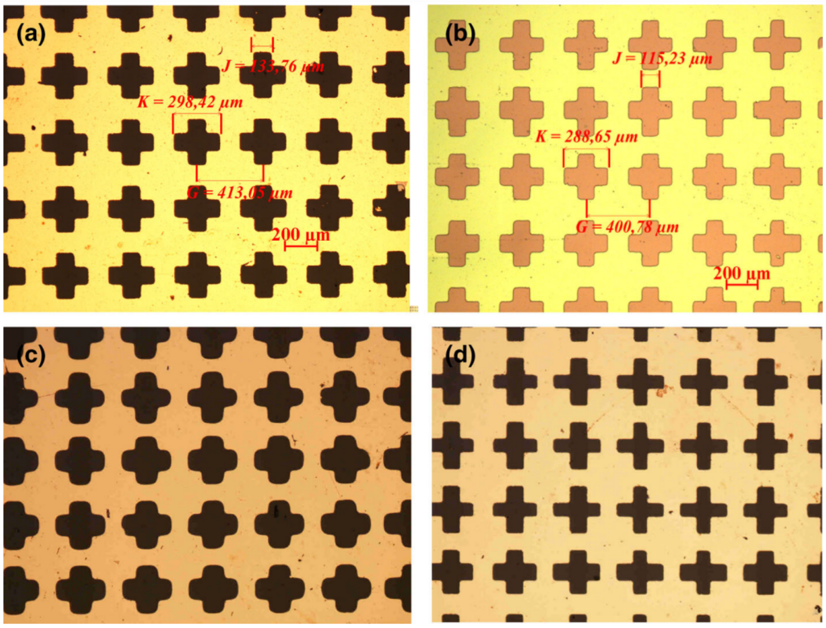

Figure 7.1: Optical microscope images of metal mesh filters (figure from SRON repository)

- **Width of elements (J)**: The width J affects how the mesh interacts with electric fields, influencing its permittivity. Wider elements can store more electric charge, acting similarly to capacitors. By modifying J, one can control the capacitive properties of the mesh, which influences how different wavelengths are transmitted or blocked.
- **Grid period (G)**: The grid period must be much smaller than the wavelength of the incoming electromagnetic wave to ensure that the mesh acts as a subwavelength structure. This helps in forming an artificial material that can manipulate electromagnetic waves in a controlled manner.

Therefore we can see that based on the wavelength that needs filtering we can tailor K, J and G values accordingly.

7.2.4. Towards perforated membranes

The next step of this research is to model the perforated membranes in COMSOL. These perforations are in the shape of crosses. In attempting to solve the issue, we realized that the layout of the crosses on the membrane is not uniformly distributed. Instead, it follows a distribution pattern.

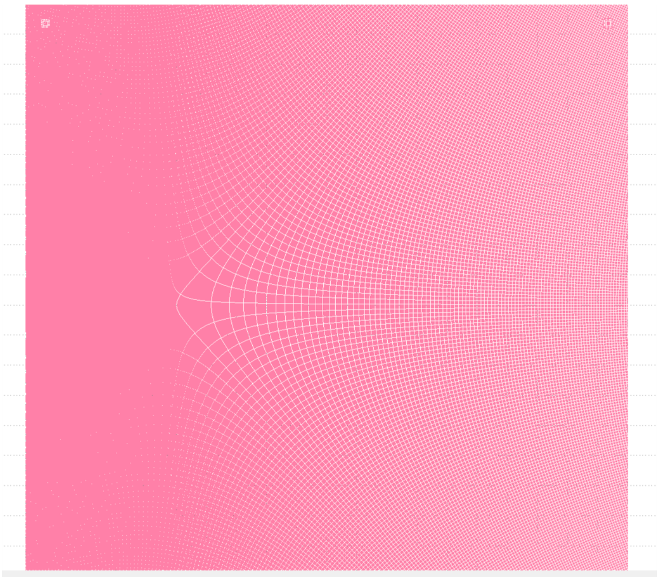

Figure 7.2: The distribution of crosses across the membrane (figure from SRON repository)

Due to the challenge of accurately representing a non-uniform distribution of cross-shaped perforations in COMSOL, a practical approach might involve approximating the distribution using a combination of simpler, well-defined distributions that COMSOL can handle more efficiently.

We can attempt to approximate the pattern using mirroring and sectioning. For areas where the perforations are nearly uniform, use a regular grid pattern. For areas with a gradient in spacing or size, use a gradient distribution model and for clusters of perforations, use localized patterns with higher density.

References

[1] NASA, *Alma mission*, `https://astrobiology.nasa.gov/missions/alma/`, Accessed: 2023-12-08, 2023.

[2] S. Casassus *et al.*, "Flows of gas through a protoplanetary gap," *Nature*, vol. 493, pp. 191–194, 2013.

[3] NASA, *Combined spitzer and alma observations reveal stellar birth in hh 46/47*, Accessed: 2023-12-08, Nov. 2013.

[4] ALMA Observatory, *Alma captures image of planet-forming disc details*, Accessed: 2023-12-08, Nov. 2014.

[5] NASA, *James webb space telescope technical information*, Accessed: [5th December, 2023], James Webb Space Telescope (JWST), 2023. [Online]. Available: `https://www.jwst.nasa.gov/resources/JWSTTech.pdf`.

[6] James Webb Space Telescope, *James webb space telescope technical resource*, `https://www.jwst.nasa.gov/resources/JWSTTech.pdf`, Accessed: [5th December, 2023], 2023.

[7] "Webb telescope: First year of science." Accessed: [8th of December, 2023]. (2023), [Online]. Available: `https://www.skyatnightmagazine.com/space-science/webb-telescope-first-year-science/`.

[8] N. F. Cothard, C. Albert, A. D. Beyer, *et al.*, "Parallel plate capacitor aluminum kids for future far-infrared space-based observatories," *arXiv preprint arXiv:2311.00773*, 2023, Accessed: 2023-12-08. [Online]. Available: `https://arxiv.org/abs/2311.00773`.

[9] Q. Yang, "Design study of a compact ultra-wide-angle high-spatial-resolution high-spectral-resolution snapshot imaging spectrometer," *Opt Express*, vol. 29, no. 2, pp. 2893–2908, Jan. 2021, PMID: 33726476. DOI: `10.1364/OE.415484`.

[10] D. J. Brady, *Optical imaging and spectroscopy*. John Wiley & Sons, 2009.

[11] M. B. Stuart, A. J. McGonigle, and J. R. Willmott, "Hyperspectral imaging in environmental monitoring: A review of recent developments and technological advances in compact field deployable systems," *Sensors*, vol. 19, no. 14, p. 3071, 2019.

[12] Y. Demirhan, H. Alaboz, and L. Ozyuzer, "Metal mesh filters based on ti, ito and cu thin films for terahertz waves," *Opt Quant Electron*, vol. 48, no. 2, p. 170, 2016. DOI: `10.1007/s11082-016-0427-z`.

[13] T. W. Ebbesen, H. J. Lezec, H. F. Ghaemi, T. Thio, and P. A. Wolff, "Extraordinary optical transmission through subwavelength hole arrays," *Nature*, vol. 391, no. 6667, pp. 667–669, 1998.

[14] P. A. R. Ade, G. Pisano, C. Tucker, and S. Weaver, "A review of metal mesh filters," *Millimeter and Submillimeter Detectors and Instrumentation for Astronomy III*, vol. 6275, no. 62750U, 62750U1–62750U15, 2006.

[15] B. A. Munk, *Frequency Selective Surfaces: Theory and Design*. John Wiley & Sons, 2000.

[16] R. Ulrich, "Far-infrared properties of metallic mesh and its complementary structure," *Infrared Physics*, vol. 7, no. 1, pp. 37–55, 1967.

[17] P. d. Maagt, R. Gonzalo, J. Y. Vardaxoglou, and J.-M. Baracco, "Electromagnetic bandgap antennas and components for microwave and (sub)millimeter wave applications," *IEEE Transactions on Antennas and Propagation*, vol. 46, no. 2, pp. 189–197, 1998.

[18] I. Ederra, R. Gonzalo, B. E. J. Alderman, P. G. Huggard, and P. d. Maagt, "Mesh filters for thz frequencies," in *2006 Joint 31st International Conference on Infrared Millimeter Waves and 14th International Conference on Terahertz Electronics*, IEEE, 2006.

[19] L. Yunjia, “Microelectromechanical systems (MEMS),” in *Material-Integrated Intelligent Systems: Technology and Applications*, New York, NY, USA: John Wiley & Sons, 2016, pp. 83–105.

[20] M. Ridder, P. Khosropanah, R. A. Hijmering, M. R. Zuiddam, *et al.*, “Fabrication of low-noise TES arrays for the SAFARI instrument on SPICA,” *Journal of Low Temperature Physics*, vol. 184, no. 1-2, 2016. DOI: 10.1007/s10909-015-1381-z.

[21] G. Silva, M. Finkel, W. M. Laauwen, *et al.*, “Beam waist properties of spiral antenna coupled HEB mixers at supra-THz frequencies,” *IEEE Transactions on Terahertz Science and Technology*, vol. 13, no. 2, pp. 167–177, 2023, Green Open Access added to TU Delft Institutional Repository ‘You share, we take care!’ – Taverne project https://www.openaccess.nl/en/you-share-we-take-care/ Otherwise as indicated in the copyright section: the publisher is the copyright holder of this work and the author uses the Dutch legislation to make this work public., ISSN: 2156-342X. DOI: 10.1109/TTHZ.2022.3230742. [Online]. Available: http://resolver.tudelft.nl/uuid:55ab9048-14c5-4d5d-bf62-f49d84d0c9ce.

[22] M. de Wit, L. Gottardi, K. Nagayoshi, *et al.*, “Performance of the sron ti/au transition edge sensor x-ray calorimeters,” in *Space Telescopes and Instrumentation 2022: Ultraviolet to Gamma Ray*, J.-W. A. den Herder, S. Nikzad, and K. Nakazawa, Eds., ser. Proceedings of SPIE - The International Society for Optical Engineering, vol. 12181, Montréal, Québec, Canada: SPIE, Aug. 2022. DOI: 10.1117/12.2629368.

[23] X. Ji, S. Roberts, M. Corato-Zanarella, and M. Lipson, “Methods to achieve ultra-high quality factor silicon nitride resonators,” *APL Photonics*, vol. 6, no. 7, 2021. DOI: 10.1063/5.0057881. [Online]. Available: https://doi.org/10.1063/5.0057881.

[24] O. Unal, J. Petrovic, and T. Mitchell, “Cvd si3n4 on single crystal sic. i - characterization and orientation relationship at the interface,” *Journal of Materials Research - J MATER RES*, vol. 7, pp. 136–147, Jan. 1992. DOI: 10.1557/JMR.1992.0136.

[25] A. Yurkov, “Silicon carbide–silicon nitride refractory materials: Part 1 materials science and processing,” *Processes*, vol. 11, no. 7, p. 2134, 2023. DOI: 10.3390/pr11072134. [Online]. Available: https://www.mdpi.com/2227-9717/11/7/2134.

[26] M. Lattemann, S. Ulrich, H. Holleck, M. Stüber, and H. Leiste, “Characterisation of silicon carbide and silicon nitride thin films and si3n4/sic multilayers,” *Diamond and Related Materials*, vol. 11, no. 3, pp. 1248–1253, 2002, ISSN: 0925-9635. DOI: https://doi.org/10.1016/S0925-9635(01)00622-7. [Online]. Available: https://www.sciencedirect.com/science/article/pii/S0925963501006227.

[27] S. Hampshire and T. Kennedy, “Silicon nitride–silicon carbide micro/nanocomposites: A review,” *International Journal of Applied Ceramic Technology*, vol. 19, pp. 1107–1125, 2022. DOI: 10.1111/ijac.13903.

[28] G. Cataldo, J. A. Beall, H.-M. Cho, B. McAndrew, M. D. Niemack, and E. J. Wollack, “Infrared dielectric properties of low-stress silicon nitride,” *Optics Letters*, vol. 37, no. 20, pp. 4202–4204, 2012, Received April 26, 2012; revised September 7, 2012; accepted September 10, 2012; posted September 10, 2012 (Doc. ID 167420); published October 4, 2012. DOI: 10.1364/OL.37.004202.

[29] B. Zhou, M. Rasmussen, S. Zibod, *et al.*, “Measurement of the dispersion of of and sin across the thz and far-infrared frequency bands,” *Laser & Photonics Reviews*, vol. n/a, no. n/a, p. 2 301 321, DOI: https://doi.org/10.1002/lpor.202301321. eprint: https://onlinelibrary.wiley.com/doi/pdf/10.1002/lpor.202301321. [Online]. Available: https://onlinelibrary.wiley.com/doi/abs/10.1002/lpor.202301321.

[30] S. Sako, T. Miyata, T. Kamizuka, *et al.*, “Developing metal coated mesh filters for mid-infrared astronomy,” in *Modern Technologies in Space- and Ground-based Telescopes and Instrumentation II*, R. Navarro, C. R. Cunningham, and E. Prieto, Eds., International Society for Optics and Photonics, vol. 8450, SPIE, 2012, p. 84503V. DOI: 10.1117/12.925768. [Online]. Available: https://doi.org/10.1117/12.925768.

[31] National Institute of Standards and Technology, *Silicon - nist cryogenic materials database*, https://trc.nist.gov/cryogenics/materials/Silicon/Silicon.htm, Accessed: April 26, 2024, 2024.

[32] M. Menzel, M. Davis, K. Parrish, *et al.*, "The design, verification, and performance of the james webb space telescope," *Publications of the Astronomical Society of the Pacific*, vol. 135, no. 1047, p. 058 002, 2023. DOI: `10.1088/1538-3873/acbb9f`. [Online]. Available: `https://iopscience.iop.org/article/10.1088/1538-3873/acbb9f`.

[33] X.-F. Wu and R. A. Jenson, "Stress-function variational method for stress analysis of bonded joints under mechanical and thermal loads," *International Journal of Engineering Science*, vol. 49, no. 3, pp. 279–294, Mar. 2011. DOI: `10.1016/j.ijengsci.2010.11.005`.

[34] E. Suhir, "Interfacial stresses in bi-metal thermostats," *Journal of Applied Mechanics*, vol. 56, no. 3, Sep. 1989. DOI: `10.1115/1.3176133`.

[35] COMSOL, *Comsol heat transfer module user's guide*, COMSOL, 2024. [Online]. Available: `https://doc.comsol.com/5.4/doc/com.comsol.help.heat/HeatTransferModuleUsersGuide.pdf`.

[36] S. S. Rao, *Mechanical Vibrations*, 5th. Pearson, 2010, ISBN: 0132128195.

[37] R. D. Blevins and R. Plunkett, *Formulas for natural frequency and mode shape*. Krieger Pub Co, 1980, vol. 47, p. 461, ISBN: 1575241846.

[38] W. C. Young and R. G. Budynas, *Roark's formulas for stress and strain*, 7th. New York: McGraw-Hill, 2002, ISBN: 0-07-072542-X.

[39] COMSOL. "Comsol multiphysics documentation." (year), [Online]. Available: `https://doc.comsol.com/5.5/doc/com.comsol.help.comsol/comsol_ref_materials.16.04.html`.

[40] Lyncee Tec, *Reflection DHM*, Accessed: February 7, 2024. [Online]. Available: `https://www.lynceetec.com/reflection-dhm`.

[41] J. Gardeniers, H. Tilmans, and C. Visser, "Lpcvd silicon-rich silicon nitride films for applications in micromechanics, studied with statistical experimental design," *Journal of Vacuum Science & Technology A: Vacuum, Surfaces, and Films*, vol. 14, no. 5, pp. 2879–2892, 1996.

[42] A. Noskov, E. Gorokhov, G. Sokolova, E. Trukhanov, and S. Stenin, "Correlation between stress and structure in chemical vapour deposited silicon nitride films," *Thin Solid Films*, vol. 162, pp. 129–143, Aug. 1988.

[43] ANSYS, Inc., *Ansys granta edupack software*, `https://www.ansys.com/materials`, Accessed: 31-07-2024, 2021.

[44] M. Xu, D. Shin, P. M. Sberna, *et al.*, "High-strength amorphous silicon carbide for nanomechanics," 2023, arXiv:YYMM.NNNNN. eprint: `arXiv:YYMM.NNNNN`.

[45] B. S. Bhadauria, A. K. Srivastava, N. C. Sacheti, and P. Chandran, "Gravity modulation of thermal instability in a viscoelastic fluid saturated anisotropic porous medium," *Zeitschrift für Naturforschung A*, vol. 67a, pp. 1–9, 2012, Received November 22, 2010 / revised June 22, 2011. DOI: `10.5560/ZNA.2011-0045`. [Online]. Available: `http://znaturforsch.com`.

[46] I. JAHM Software, *Material property database*, `https://www.jahm.com`, Accessed: 2024-07-31.

[47] L. Cornwell, P. Wozniakiewicz, M. Burchell, *et al.*, "A study on the capabilities and accuracy of kapton based tof space dust and debris detectors," *Advances in Space Research*, vol. 72, no. 7, pp. 2959–2970, 2023, Space Environment Management and Space Sustainability, ISSN: 0273-1177. DOI: `https://doi.org/10.1016/j.asr.2022.07.022`. [Online]. Available: `https://www.sciencedirect.com/science/article/pii/S0273117722006238`.

[48] S. De Nicola, P. Ferraro, A. Finizio, and et al., "Surface topography of microstructures in lithium niobate by digital holographic microscopy," *Measurement Science and Technology*, vol. 15, no. 5, p. 961, 2004.

[49] F. Dubois, N. Callens, C. Yourassowsky, M. Hoyos, P. Kurowski, and O. Monnom, "Digital holographic microscopy with reduced spatial coherence for three-dimensional particle flow analysis," *Applied Optics*, vol. 45, no. 5, pp. 864–871, 2006.

[50] N. Verrier, C. Fournier, and T. Fournel, "3d tracking the brownian motion of colloidal particles using digital holographic microscopy and joint reconstruction," *Applied Optics*, vol. 54, no. 16, pp. 4996–5002, 2015.

[51] P. Langehanenberg, L. Ivanova, I. Bernhardt, and et al., “Automated three-dimensional tracking of living cells by digital holographic microscopy,” *Journal of Biomedical Optics*, vol. 14, no. 1, pp. 014 018–014 018, 2009.

[52] E. Cuche, P. Marquet, and C. Depeursinge, “Simultaneous amplitude-contrast and quantitative phase-contrast microscopy by numerical reconstruction of fresnel off-axis holograms,” *Applied Optics*, vol. 38, no. 34, pp. 6994–7001, 1999.

[53] T. Colomb, J. Kühn, F. Charrière, C. Depeursinge, P. Marquet, and N. Aspert, “Total aberrations compensation in digital holographic microscopy with a reference conjugated hologram,” *Optics Express*, vol. 14, no. 10, pp. 4300–4306, 2006.

[54] COMSOL, *Membrane modeling in comsol multiphysics*, `https://doc.comsol.com/5.5/doc/com.comsol.help.sme/sme_ug_membrane.10.03.html`, Accessed: 2024-07-31.

[55] R. Vaidyanathan, J. Sankar, and V. Avva, “Uniaxial tensile characteristics of silicon nitride at room temperature,” in *12th Annual Conference on Composites and Advanced Ceramic Materials: Ceramic Engineering and Science Proceedings*, Wiley Online Library, 1988, pp. 1383–1392.

[56] COMSOL AB, *Membrane module user’s guide*, Version 6.2, 2023. [Online]. Available: `https://doc.comsol.com/6.2/docserver`.

[57] K. Luke, Y. Okawachi, M. R. E. Lamont, A. L. Gaeta, and M. Lipson, “Broadband mid-infrared frequency comb generation in a si3n4 microresonator,” *Opt. Lett.*, vol. 40, pp. 4823–4826, 2015. DOI: `10.1364/OL.40.004823`.

[58] Lyncée Tec, *Phase Microscopy*, `https://www.lynceetec.com/phase-microscopy`, [Accessed: July 5, 2024], 2024.

[59] X. Lai, H. Lin, Q. Chen, Y. Ge, C. Su, and K. Wei, “Performance of the 1d standard polynomials fitting method for total phase aberration compensation in digital holographic microscopy,” *Optik*, vol. 223, p. 165 586, 2020. DOI: `10.1016/j.ijleo.2020.165586`.

[60] M. A. Schofield and Y. Zhu, “Fast phase unwrapping algorithm for interferometric applications,” *Optics Letters*, vol. 28, no. 14, pp. 1194–1196, 2003. DOI: `10.1364/OL.28.001194`.

[61] L. L. García, A. G. Arellano, and W. Cruz-Santos, “A parallel path-following phase unwrapping algorithm based on a top-down breadth-first search approach,” *Optics and Lasers in Engineering*, vol. 124, p. 105 827, 2020. DOI: `10.1016/j.optlaseng.2019.105827`.

Appendices

Appendix A - Steps for deflection measurement in Koala Software

This appendix provides a detailed, step-by-step explanation of how deflection profiles are acquired and how the maximum deflection values are determined during the measurement of the test specimen.

A.1. Step by step procedure

- **Koala interface**: Lyncée Tec provides a power supply unit for the microscope and motorized stage, which must be switched on before commencing measurements. Subsequently, the Koala software is launched by clicking on its icon to initiate operations.

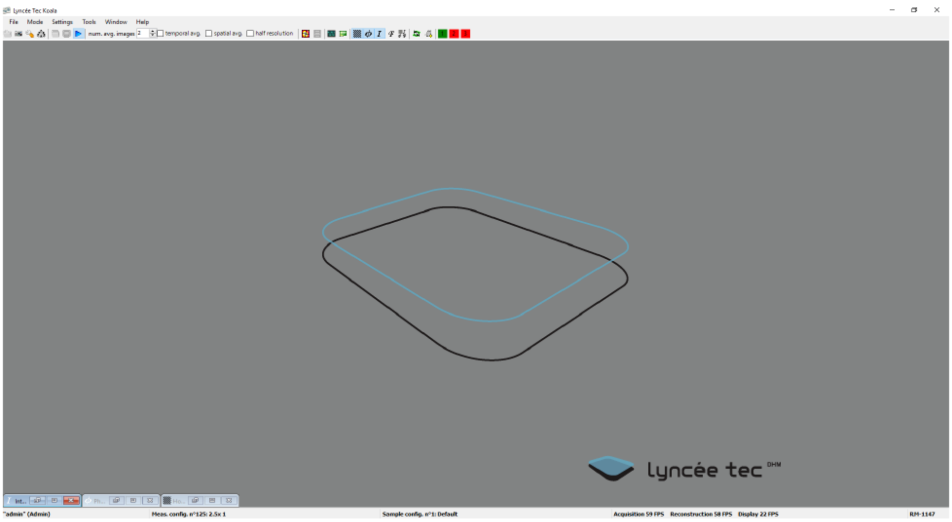

Figure A.1: Main window

The Koala main window, depicted in Figure A.1, is structured into three primary sections:

  - Menu bar, as shown in Figure A.2, comprises seven drop-down menus (FILE, MODE, SETTINGS, OPTIONS, TOOLS, and HELP) along the top line. Additionally, there are icon buttons located on the lower bar, providing shortcuts and commands for quick access.
  - Main section of the program, initially empty upon launch, serves as the display area for hologram presentations as well as for viewing phase and intensity measurements.
  - Status bar, as illustrated in Figure A.3, is structured horizontally with several fields from right to left.

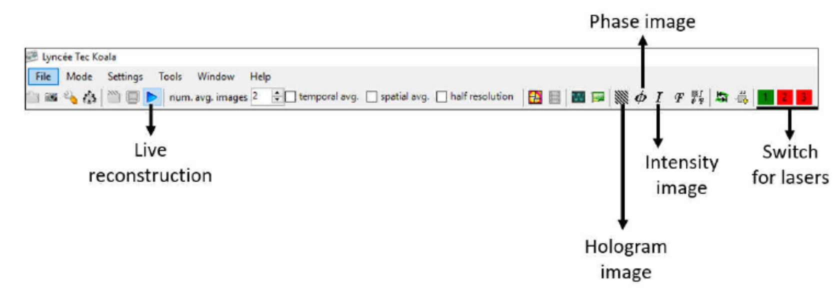

Figure A.2: Menu bar

Figure A.3: Status bar

* ⋆ Status: This field indicates the operational status of the microscope. Any errors that occur are displayed here.
* ⋆ Name of the current configuration: This field shows the name or description of the current configuration settings.
* ⋆ Acquisition rate: When the camera is active and capturing data, this field displays the acquisition rate.

- **Initial configuration setting**: Once the main window is launched, the first step involves selecting a configuration that matches the chosen objective and wavelength of the laser source. This can be done by accessing the ”Open configuration” command located in the FILE menu. Digital Holographic Microscopy (DHM) provides predefined factory configurations that cannot be modified or deleted.

  Upon selecting ”Open configuration,” a dialogue box (refer to Figure A.4) will appear, allowing the user to choose the desired configuration. Note that only one configuration can be active at any given time.

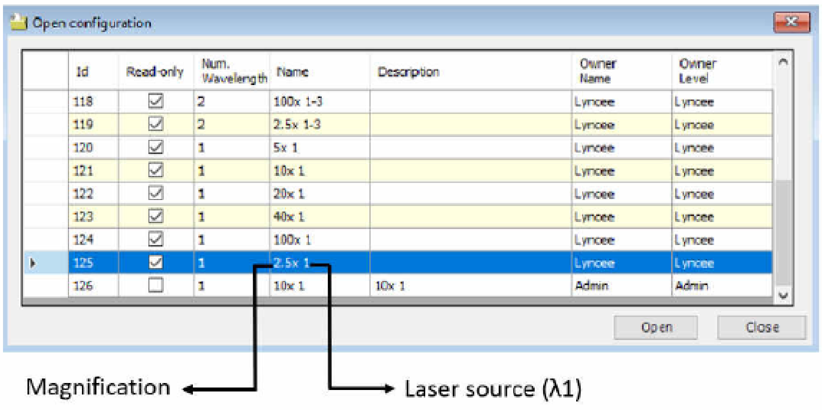

Figure A.4: Configuration options

In our specific case, the configuration selected corresponds to a 2.5x magnification and a laser source with a wavelength of 665.5651 nm.

However, for our membrane, the field of view is not enough to view the entirety of the membrane at once. With the lowest magnification of 2.5x, we can only see a box of 2.6mm x 2.6mm, which is approximately 1/16th of the entire membrane. That is why we use the stitching tool [INSERT FIGURE] to take several pictures along the x and y axes at a particular frequency and stitch all these pictures to reconstruct the whole membrane.

The resolution therefore is 2600 μm / 1024 (pixels) which gives us 2.5 μm.

- **Hologram acquisition**: After selecting a suitable configuration, the next step is to choose an appropriate functional mode within the Koala program to begin analyzing the test specimen. The "Live reconstruction" command, available in the main window, enables real-time operation. This mode facilitates the continuous acquisition of holograms and immediate reconstruction of phase and intensity images.

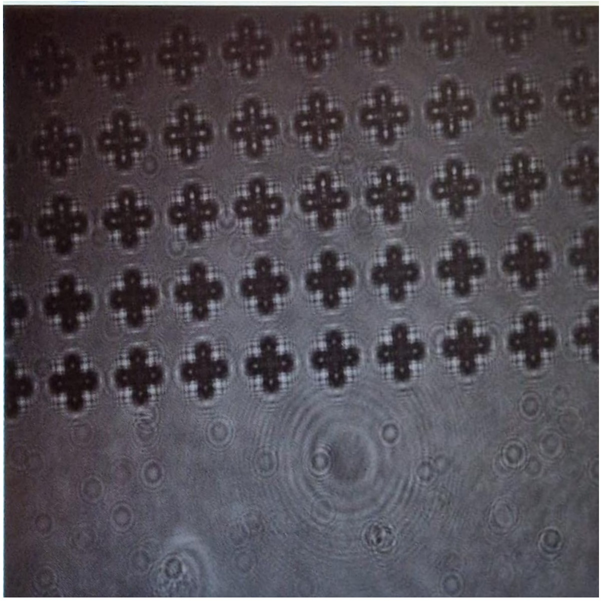

Figure A.5: Hologram window of a sample filter with crosses

Activating the live reconstruction mode initiates the direct recording of images by the camera, capturing the holograms generated by the Digital Holographic Microscopy (DHM) setup (Figure A.5). This process allows for dynamic, ongoing analysis of the specimen's characteristics and behaviour.

- **Intensity image**: Digital Holographic Microscopy (DHM) provides two types of sample representations: intensity (or amplitude contrast) images and phase (or phase contrast) images. Intensity images resemble those produced by traditional optical microscopes. However, it's important to note that these intensity images are captured using a monochromatic source (such as a laser) rather than white light, which covers the full spectrum of visible wavelengths. Consequently, intensity images do not convey information about the sample's colour but indicate the degree of focus.

  To obtain an intensity image, users can select the intensity icon I from the menu bar (refer to Figure A.2). When viewing the intensity image it resembles the representation shown in Figure A.6.

  If we wish to improve the focus on the sample, the DHM objective needs to be adjusted closer to the specimen. This adjustment can be accomplished manually by rotating the screw head located at the rear of the microscope or by utilizing the XYZ stage controller.

- **Phase image**: To analyze the phase image of the sample and obtain its deflection profile, adjust the intensity image correctly. The phase window in the MENU bar (Figure A.2) facilitates this analysis.

  Figure A.7 demonstrates the principle of phase measurement using Digital Holographic Microscopy (DHM) on a homogeneous reflective sample illuminated by a monochromatic plane wave with wavelength λ. During reflection from the sample, the wavefront undergoes deformation. This deformation relative to the incident wave, measured in degrees, is termed dephasing $\Delta\phi$ [58]. For a homogeneous sample, this dephasing directly correlates with the sample's 3D surface profile

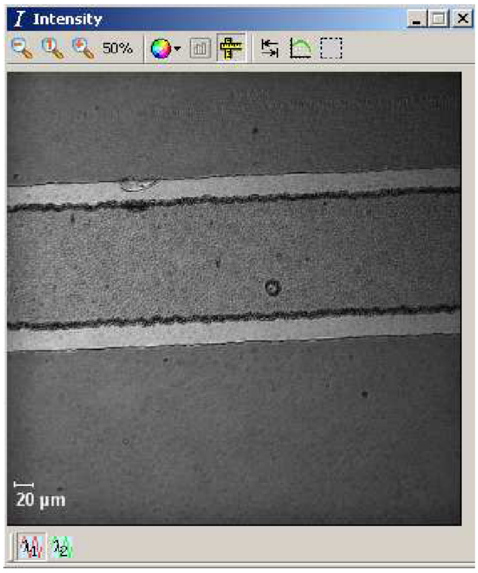

Figure A.6: Intensity window of our sample showing the boundary between the frame and the tape

through the equation:

$$\Delta h = \frac{\lambda \Delta \phi}{4\pi n}$$

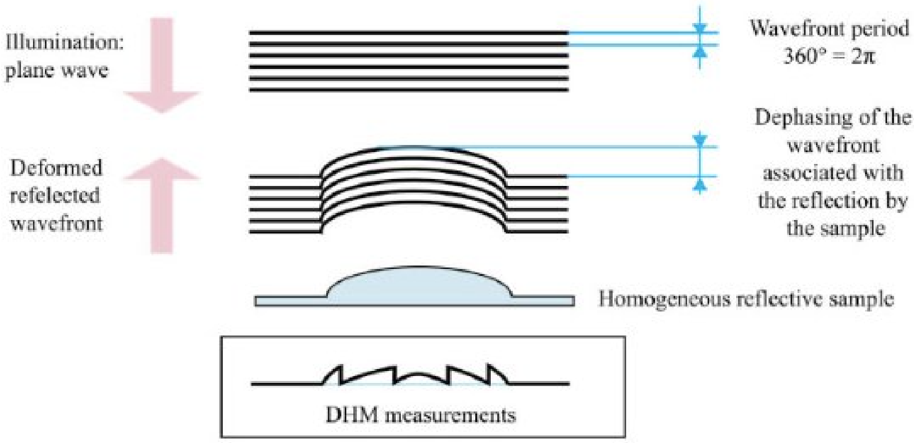

Figure A.7: Phase image principle in DHM

In DHM, Δh represents the height of the sample and n denotes the refractive index of the immersion medium (where $n = 1$ in air). As typical in interferometric metrology, discontinuities in sample height result in discontinuities in the phase measurements. The phase map is "wrapped" within the range of $-\pi$ to π for interferometric geometries. Therefore, DHM measures the phase modulo 2π as described in the following equation. This behaviour is analogous to the topography shown at the bottom of Figure A.7.

$$\phi_{\text{DHM}} = \frac{\Delta h 4\pi n}{\lambda} \mod 2\pi$$

For samples with sufficiently smooth topography, it is feasible to use a mathematical technique known as phase unwrapping, available in the Koala software, to reconstruct the 3D wavefront topography from the phase image obtained by DHM, removing the 2π ambiguity.

In summary, dephasing in phase measurement quantifies the phase difference relative to a reference plane typically defined within the sample. The Koala program offers various options to define and digitally adjust this reference plane, including digital tilt and phase offset adjustments.

- **Digital tilt and phase offset adjustment**: When the phase window is opened, likely, an image resembling the one shown in Figure A.9 will appear. This is often due to the microscope's reference plane not aligning with that of the sample. DHM can perform this alignment digitally. In Koala software, the XY planes of two reference frames (angles α and β in Figure A.10) are digitally matched.

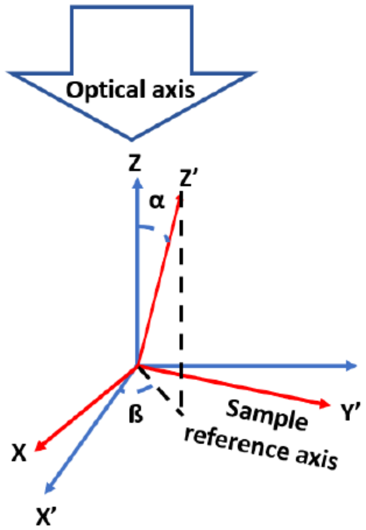

Figure A.8: Reference planes XYZ

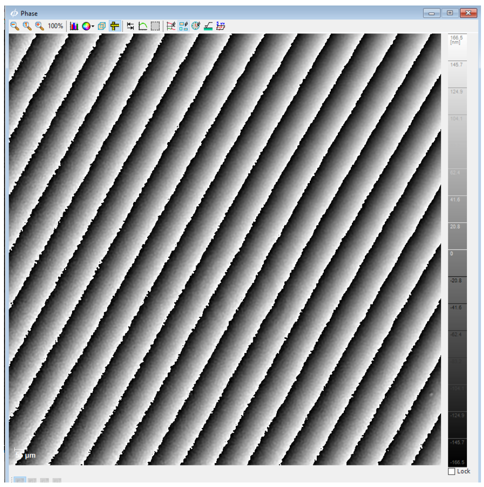

Figure A.9: Phase image of the filter showing interference fringes

Practically, phase measurement in Digital Holographic Microscopy (DHM) involves two main steps:

- Determination of the angles α and β between the microscope and sample reference planes, known as tilt adjustment.

  A 3D topographic measurement requires alignment relative to an orthogonal XYZ reference plane. The XY plane of this reference is aligned with the sample plane using the tilt correction tool. By default, Koala employs the 1D tilt fitting method for this adjustment [59]. To execute this, the phase mask adjustment tool at the top of the phase window must be selected (Figure A.10). Drawing at least two orthogonal segments on a reference surface of the sample assists Koala in performing the tilt adjustment. The same figure also depicts the reconstructed phase image after the tilt adjustment.

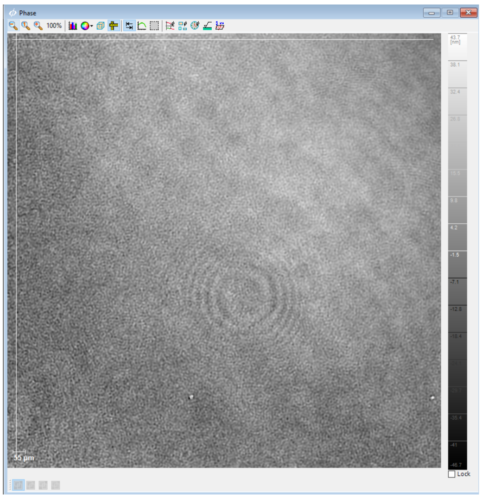

Figure A.10: Phase window with phase mask adjustment and phase offset adjustment

– Adjustment of the origin of the reference frame to the optical axis (Z) or offset adjustment.

  Once the sample plane is aligned relative to the reference plane, the origin of the plane (X=0, Y=0, Z=0) needs to be defined. Typically, the origin of the Z-axis (vertical) is set by defining an offset area using the phase offset adjustment tool available on the phase window (Figure A.10). This tool specifies the Z-axis value at a precise location, enabling consistent comparison of successive measurements with the same vertical reference individually. This is achieved by delineating surfaces or areas where the phase should be computed. Multiple areas can be defined, and the phase average will be calculated across these regions. It is advisable to define offset areas or surfaces on flat parts of the sample to utilize the full vertical range of deflection measurement efficiently. If no specific zone is selected, Koala automatically adjusts the offset using the phase average calculated over all regions of interest.

- **Phase unwrapping**: Once the phase image is obtained, it becomes evident that there are contour lines in the phase map that exhibit discontinuities (Figure A.10). Phase measurements of surfaces with height discontinuities result in phase jumps appearing in the phase map. This phenomenon is known as phase wrapping, where the phase values are constrained within a periodic interval, typically between $-\pi$ and π. These phase jumps can be visualized in the deflection profile.

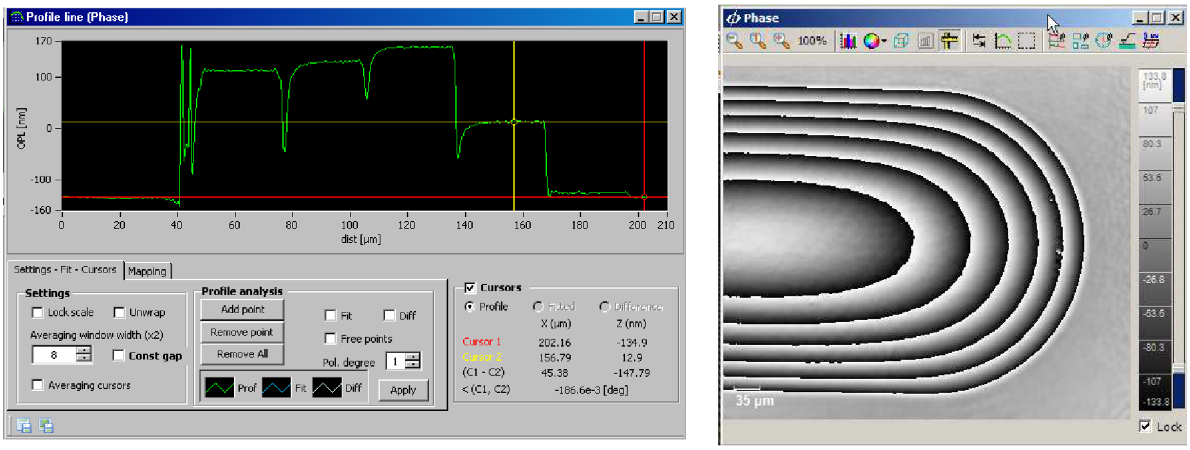

Figure A.11: Wrapped phase image and 1D profile

Using the 1D profile option available in the phase window, a deflection profile along a specific line can be extracted. Figure A.11 illustrates the wrapped phase map and the corresponding 1D deflection profile.

Unwrapping is a mathematical transformation of the phase image that yields good results when applied to regions of interest with consistently well-defined phase information. In Koala software, there are two unwrapping methods available:

- DCT unwrapping: This method solves the unwrapping equation in a least-squares sense using the discrete cosine transform. It is computationally less intensive but sensitive to noise, particularly in areas of the image without a signal from the sample [60].
- Path following method: This method is another solver of the unwrapping equation, supporting user-defined masks and automatically generated quality masks. It begins the unwrapping process from high-quality points and progresses to lower-quality ones. This method is less sensitive to noise because noisy regions are filtered out by the masks [61]. It is computationally more expensive but better suited for dynamic measurements.

The unwrapping algorithm can be selected using the phase unwrapping command found in the SETTINGS menu of Koala. Once the method is chosen, unwrapping can be executed by clicking the appropriate icon in the phase window. Figure A.12 illustrates the unwrapped phase image alongside the corresponding deflection profile.

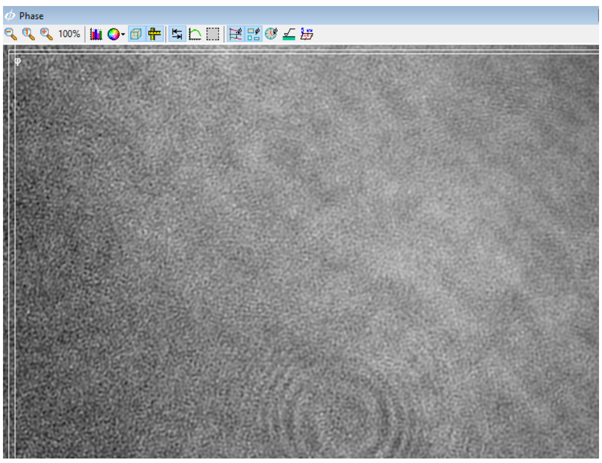

Figure A.12: Unwrapped phase image

Table A.1: Koala software setup and hologram acquisition process in brief

Step	Image
1. Launch Koala software	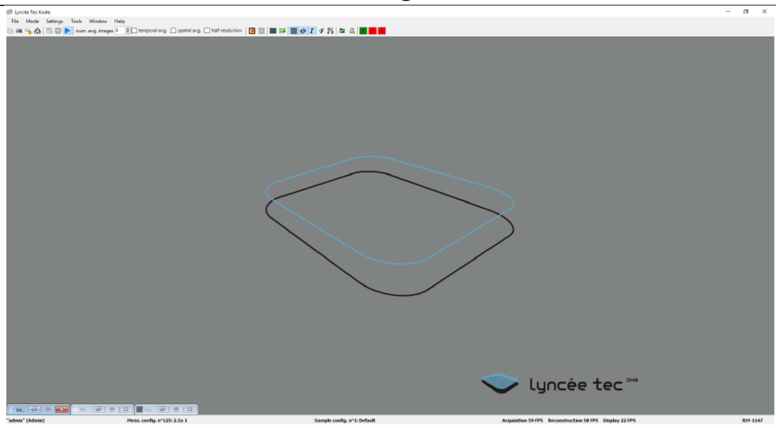
2. Live reconstruction	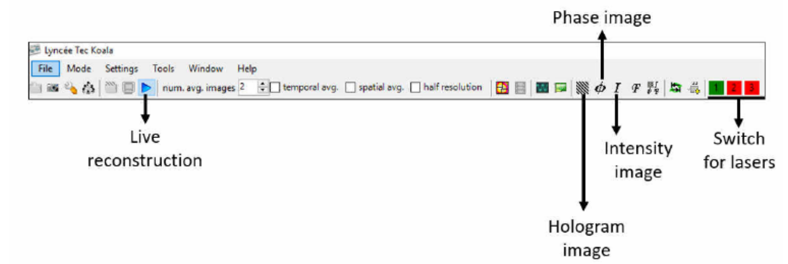
3. Select configuration	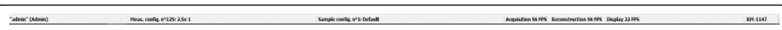
4. Set magnification and laser wavelength	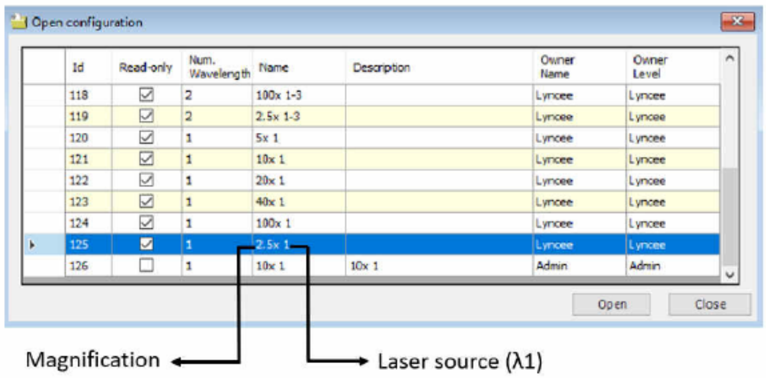
5. Use stitching tool	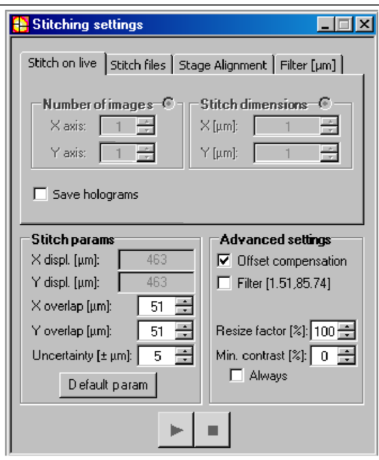

Step	Image
6. Choose functional mode and acquire hologram	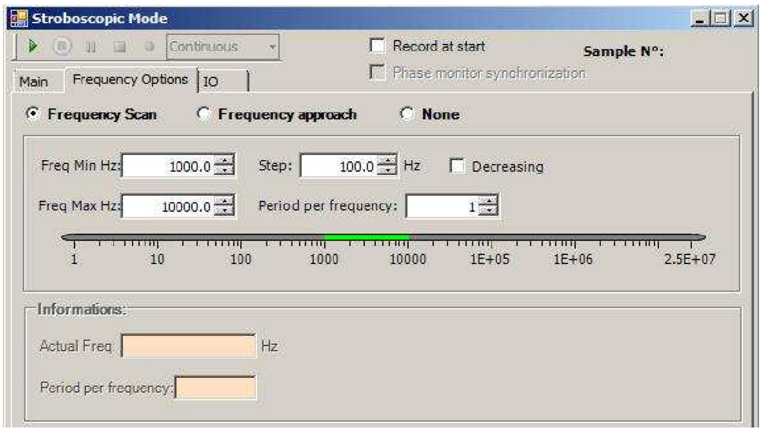

B

Appendix B - Step by Step for LDV measurements through Polytec

The Doppler Effect: Laser vibrometry leverages the Doppler effect to measure vibrations. When light is scattered from a moving object, its frequency changes slightly.

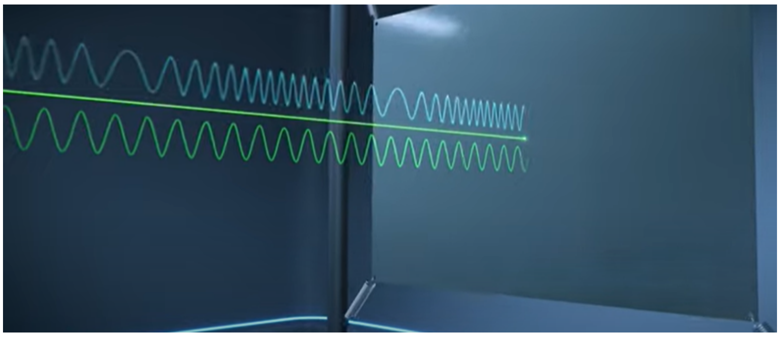

Figure B.1: Frequency change

Within the Polytec vibrometer, a high-precision interferometer detects these minute frequency shifts in the backscattered laser light as shown in Figure B.2.

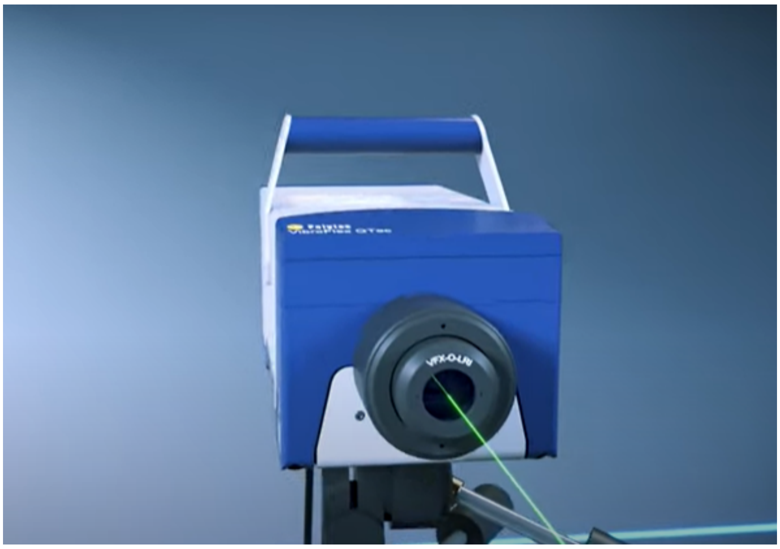

Figure B.2: The interferometer

The interferometer splits the light into two parts: the reference beam, which is directed at the photodetector, and the measurement beam, which is directed at the test object where the light scatters from the moving surface as shown in Figure B.3.

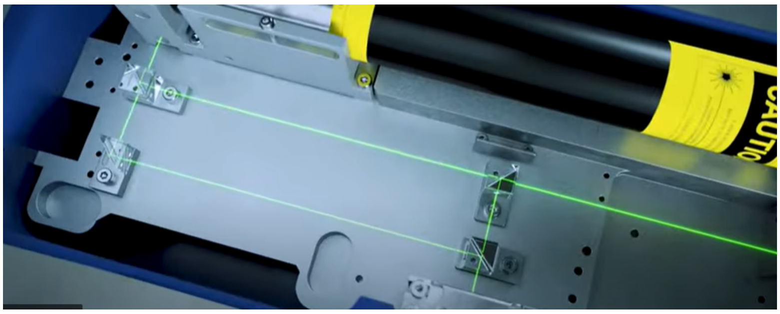

Figure B.3: The splitting of the light

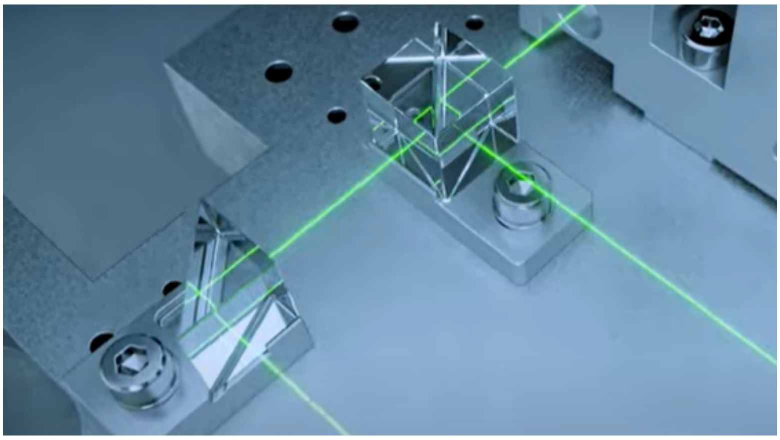

Figure B.4: Beam splitters

The frequency and phase of the backscattered light change depending on the object's velocity and displacement. The motion characteristics are entirely contained in this backscattered light.

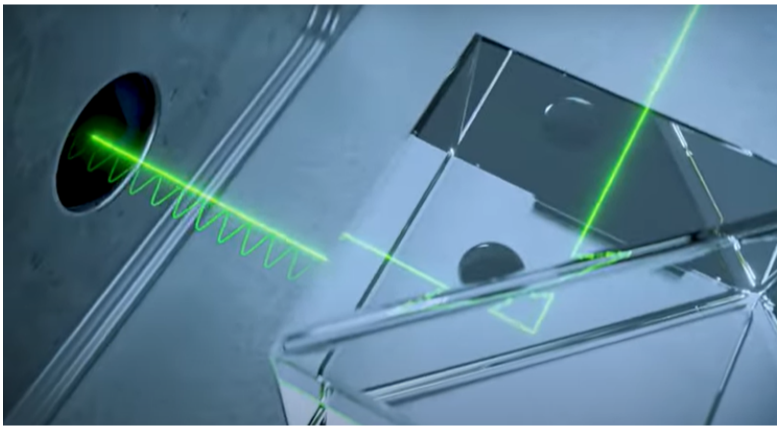

Figure B.5: Backscattered light

The superposition of this light with the reference beam creates a modulated detector output signal, revealing the Doppler shift in frequency.

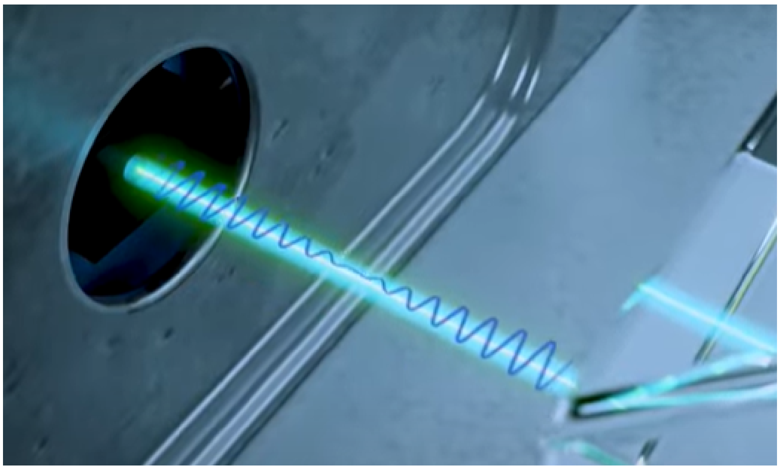

Figure B.6: Superimposed signal

Signal processing and analysis then provide the vibrational velocity and displacement of the test object.

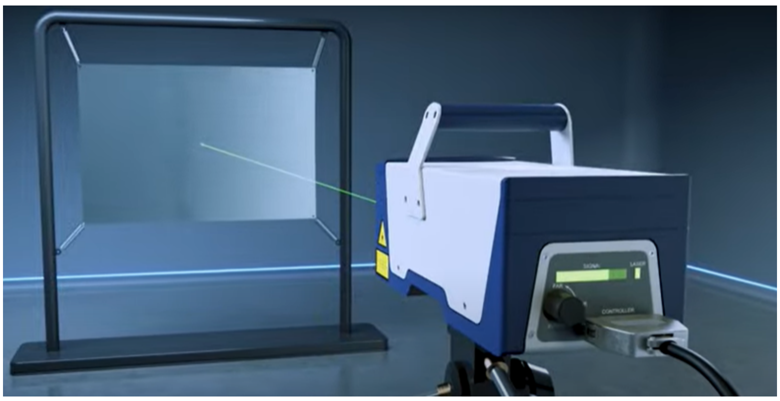

Figure B.7: The setup in brief

To induce vibrations on the surface, we use piezo actuators as shown in Figure 3.8a.

Operational Schematic:

1. The laser source box produces a laser beam, which travels through an optical fibre on the right.

Figure B.8: Interferometer boxe

2. The beam enters the optical head of the instrument.

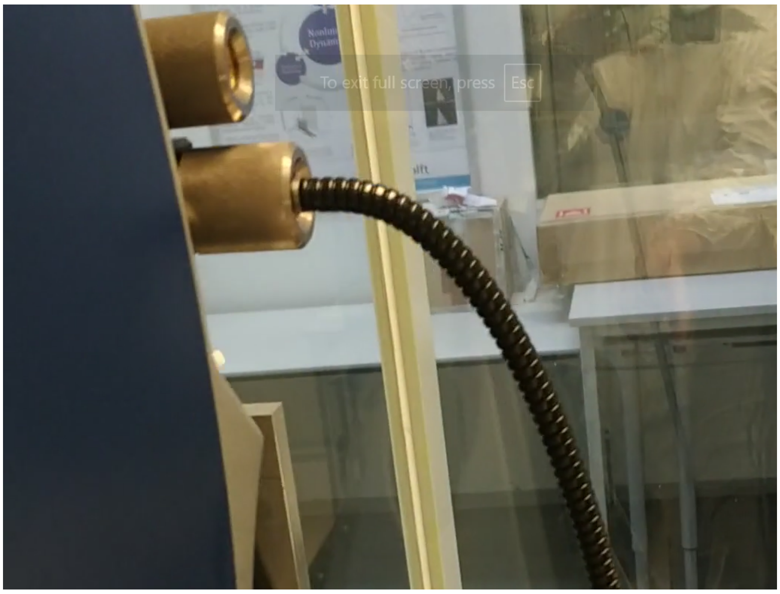

Figure B.9: Source signal

3. The laser passes through the microscope objective, reflects off the sample surface and returns to the laser source box via the same optical fibre (see Figure 12).

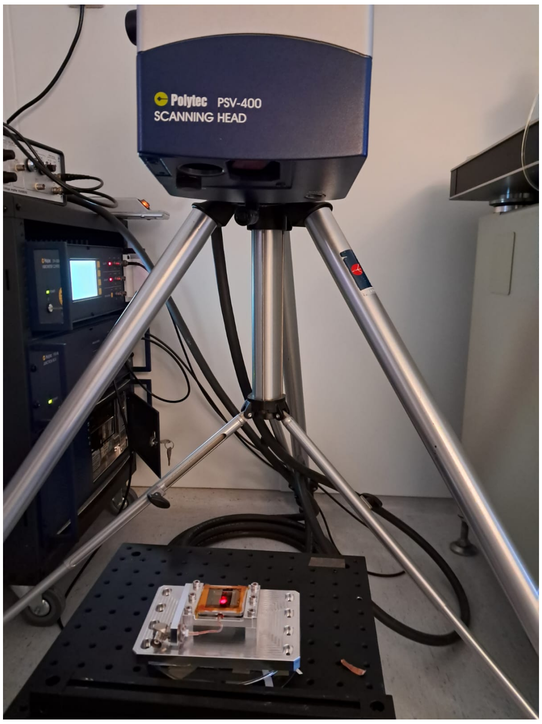

Figure B.10: The PSV setup with our sample mounted

4. The system processes the light and displays the results on the PSV acquisition software interface.

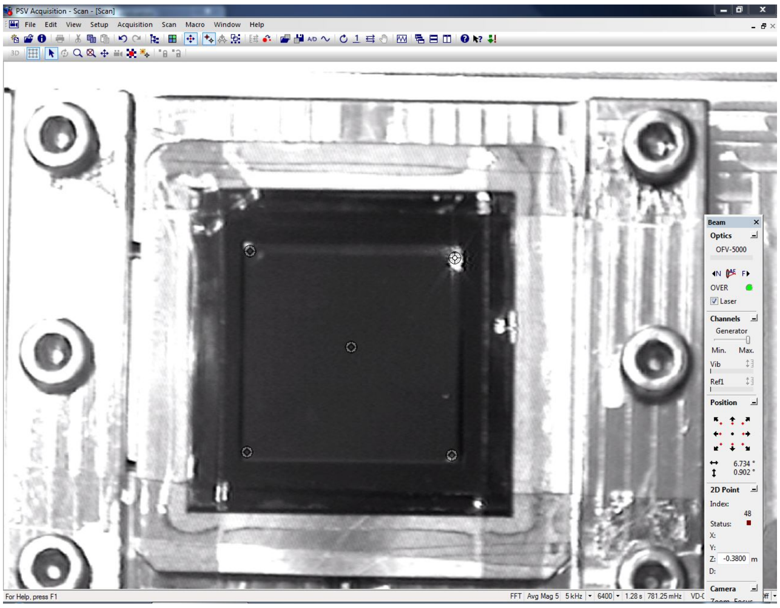

Figure B.11: Focusing in the PSV software

5. A second optical fibre generates a reference beam in the optical head.

After placing the sample under the microscope, we observe a red light as shown in Figure B.1. This illumination is from the microscope and serves as a guide to position the sample correctly under the microscope for visibility.

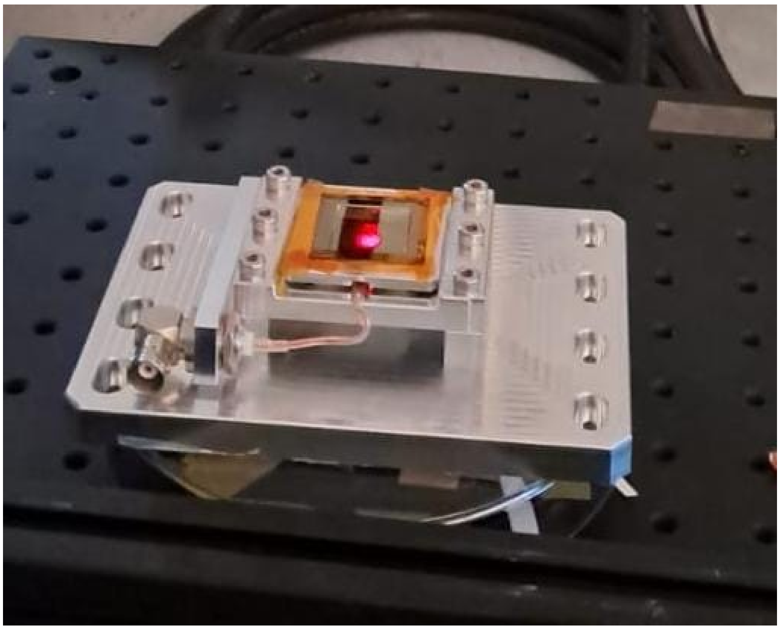

Figure B.12: Sample with the red light

Next, we focus the microscope on the sample using coarse and fine adjustment tools. The sample fits in the FOV of the LDV and therefore, requires no magnification. Once we obtain a clear image, we turn on the laser. The instrument's top display shows the signal strength, indicating the reflection amount from the sample surface. Ideally, the signal strength should be as high as possible, with a minimum of 50% required to ensure low-noise vibrational data.

To maximize reflectivity, most samples are coated with a layer of aluminium or gold.

Figure B.13: The bar of reflectivity

For MEMS systems, we select an output signal in the velocity mode, which is sensitive in the picometer range. The velocity output is in an analogue scale and needs digitization, which is performed by a separate junction box.

Acquisition in software:

1. This is the screen which pops up when we click on the PSV Acquisiton - Scan software. With this device, we can do single-point measurements in which we see the vibration pattern. To get an idea of the entire sample, we can scan the laser over a multitude of points through which we can reconstruct the vibration shapes.

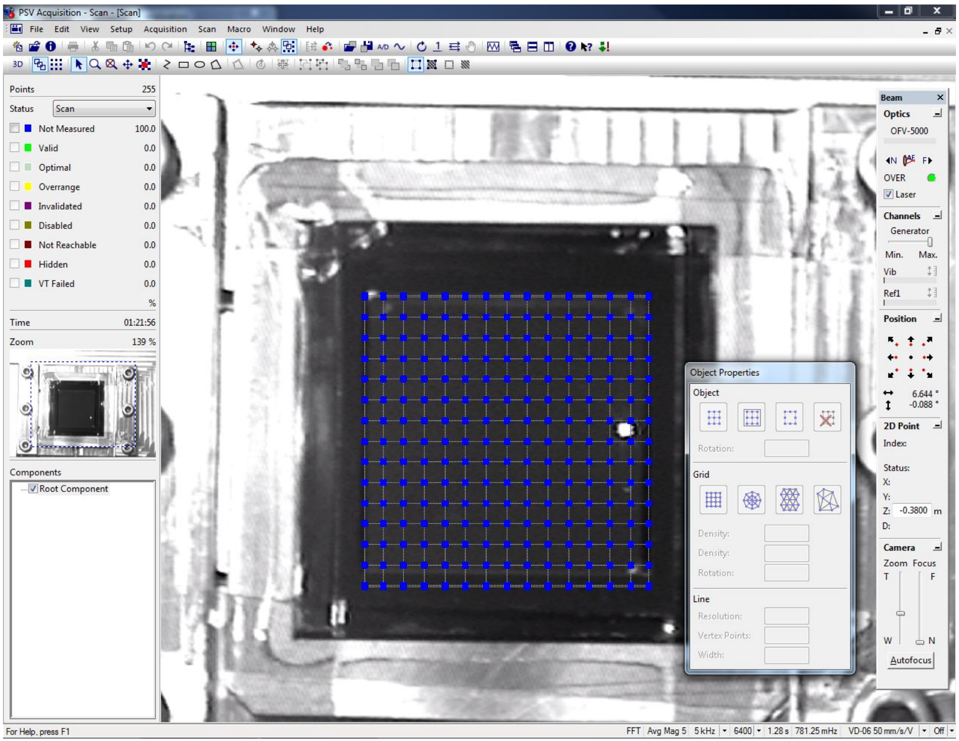

Figure B.14: Vibration shape reconstruction via grid points

If we wish to change the illumination we can do it by right-clicking the sample area on the screen and selecting Display Properties. Then this window pops up.

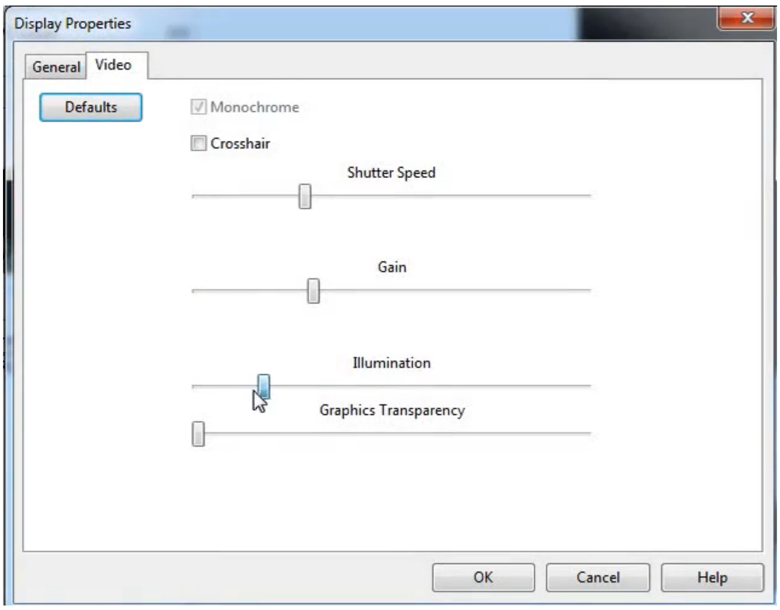

Figure B.15: Display properties

2. First of all we need to get our laser beam aligned with our sample. We need to calibrate our laser beam every time we change our focus. For this, we enter the 2D alignment menu as shown in Figure B.16. After clicking we enter the window shown in Figure B.17. Here we can set our alignment points by dragging the laser beam by clicking the middle mouse button. We can see our final points in Figure B.17.

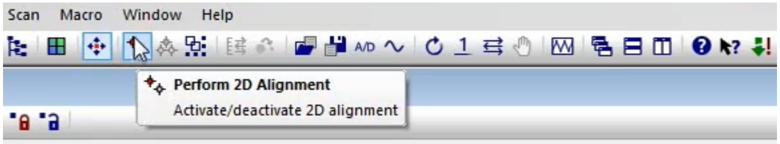

Figure B.16: Accessing the 2D alginment menu

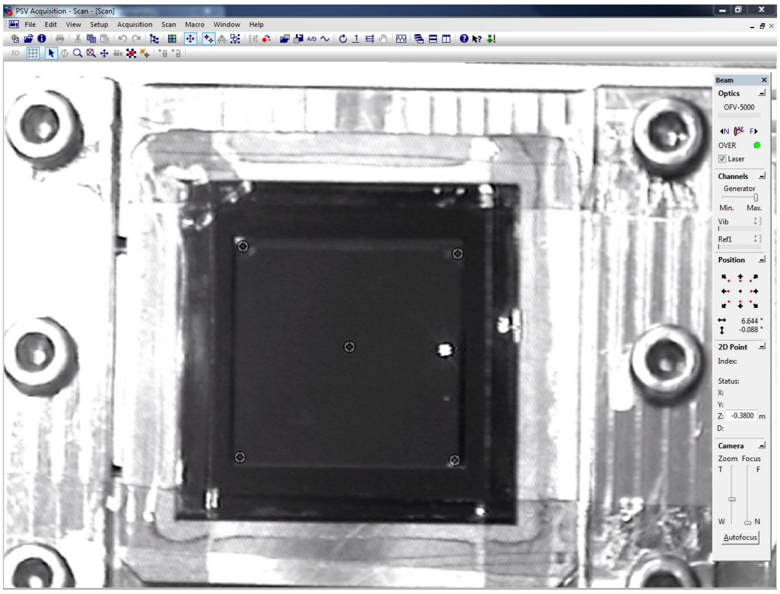

Figure B.17: Setting alignment points

3. Next step is to define the grid of points that we use for our measurements as shown in Figure B.18. We do it by selecting the option Define Scan Points as shown in Figure B.19.

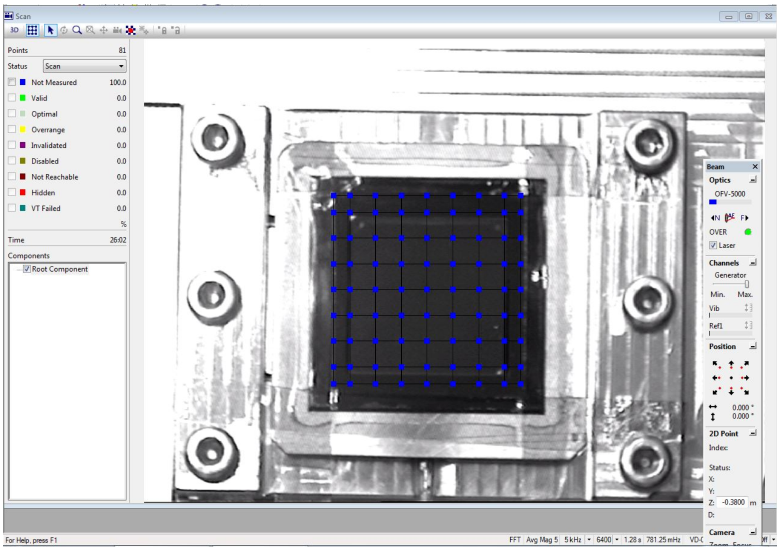

Figure B.18: Alignment points set

We have a lot of options for our grid shape like a rectangle, circle or even a line. Normally, rectangles or squares are ideal unless it is a circular membrane. Here in the side window, we can set the density of points, which for us is 30x30. Then we align the grid to our sample surface.

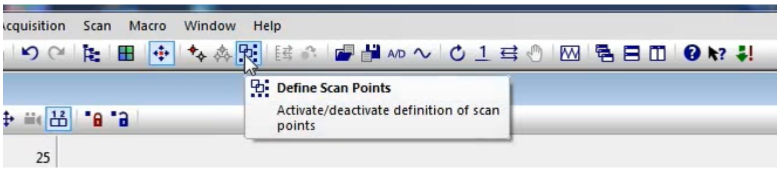

Figure B.19: Defining the scan points

4. The next step is to configure our measurements. We do that by clicking on A/D setting as shown in Figure B.20. This opens a dialogue box containing all the meaningful settings of our measurement.

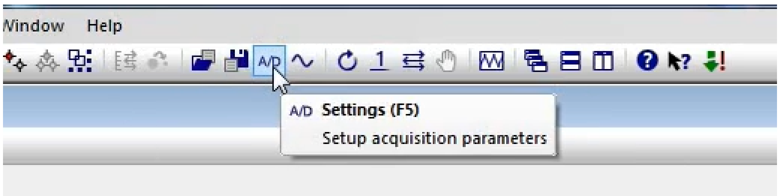

Figure B.20: Accessing the measurement configuration menu

Going from the last box, this is where we configure our function generator. This is the signal that we apply to our piezo as shown in Figure B.21. We have different options for waveform, but we've picked sweep to be consistent with our DHM measurements. Also with amplitude 4V with an offset of 2V. Our scanning sweep is from 4 kHz to 15 kHz.

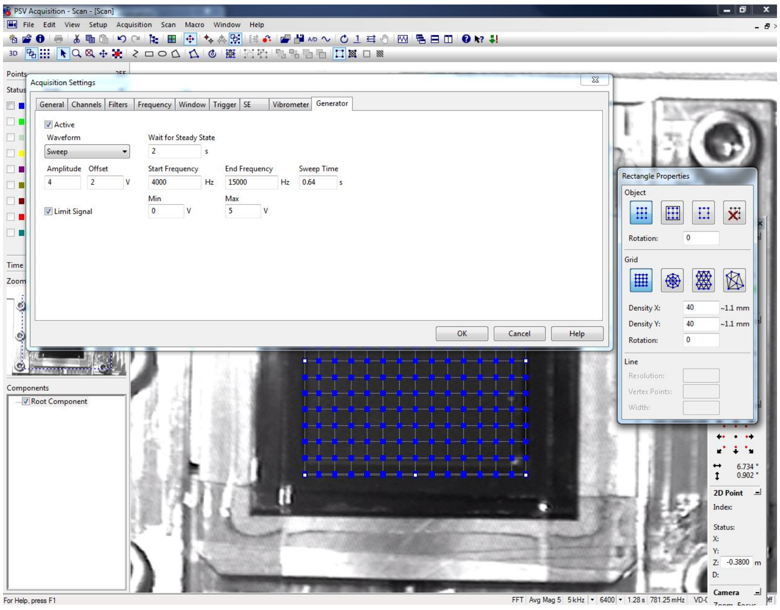

Figure B.21: Configuring the measurements

5. In the general tab as shown in Figure B.22, we define the type of our measurement. In this case, we stick to FFT (fast Fourier transform). The other options are not relevant to our data. Assuming a reflective device, we can set the averaging to off.

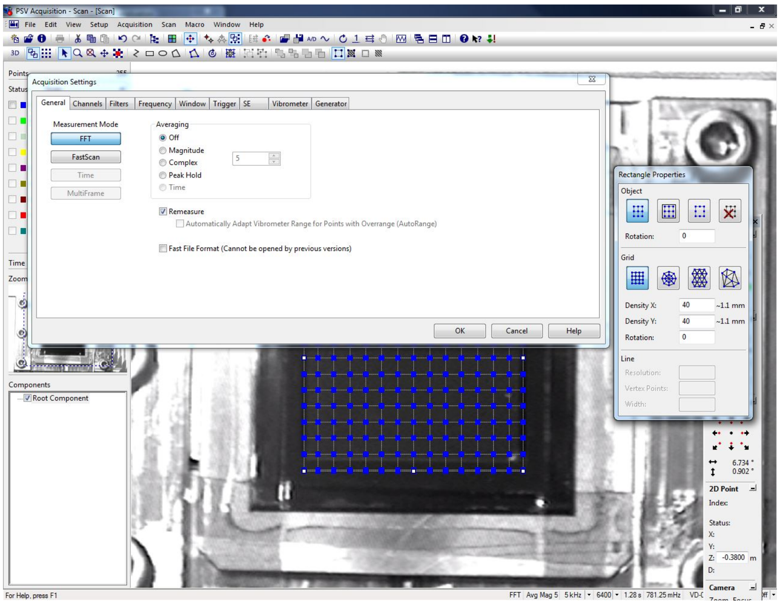

Figure B.22: Setting the measurement type

6. In the frequency tab as shown in Figure B.23, we use the FFT mode as set in the General tab. With this, we obtain the frequency domain content of the signal. We fix the bandwidth, which depends on the highest frequency I wish to detect. For our sample, it is 20 kHz. This automatically sets the sampling frequency needed for this bandwidth. This is derived from the Nyquist theorem [maybe give a reference?]. Another important parameter is the number of FFT lines. This will set the frequency resolution and the distance between the frequency lines. So for 6400 lines, we have a resolution of 3.125 Hz. This is simply the Bandwidth, divided by the number of FFT lines [insert math equation]. The sample time, which is the total recording time per point, is also calculated

according to the number of FFT lines. For the from and to sections, we have to select a range within the bandwidth, which for us is say from 0.1 kHz to 20 kHz.

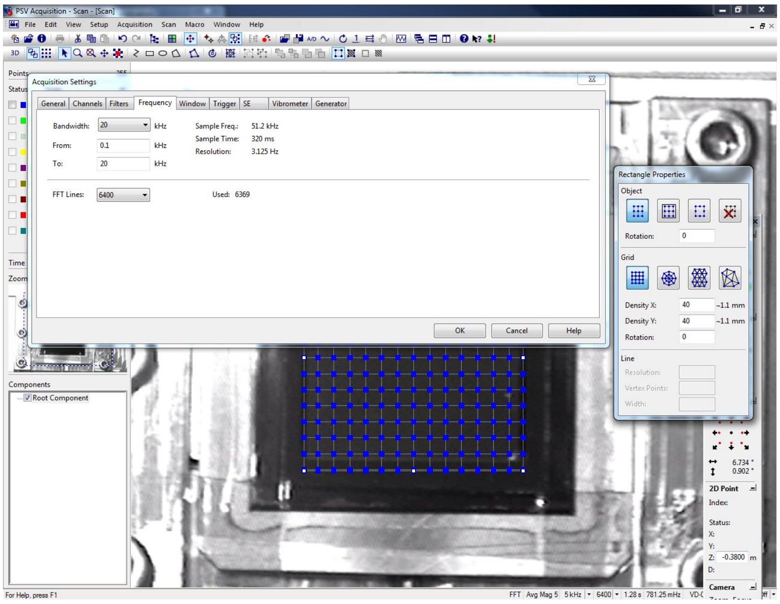

Figure B.23: Select bandwidth range

7. In the final tab the vibrometer as shown in Figure B.24, we configure the sensitivity of the decoding. VD stands for velocity decoder and we have used the configuration 02. Here, a sensitivity of 5mm/s/V stands for when the laser is at some point, that point moves at a speed of 5mm/s, and then the signal general by the decoder will have an amplitude of 1 V. This is important because, if the sensitivity is very low then it might produce a very large voltage of the decoder, and when we try to digitize it, it might be outside the range of the vibrometer. This leads to saturation of the digitization [maybe have a figure here]. The max frequency here should be set accordingly so that the bandwidth can allow for it.

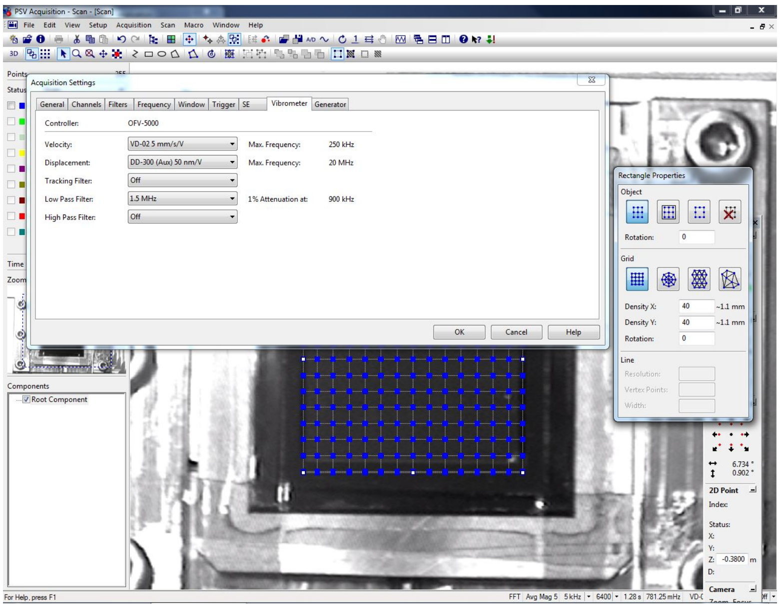

Figure B.24: Set maximum frequency

8. Now for our measurements, we click on Scan as shown in Figure B.25, and our generator is

activated automatically (unlike single point measurement). Then it will start measuring point by point over our entire grid. The green symbol signifies optimal signal strength. If it is yellow, then the signal was out of range and the instrument has averaged [have a picture of this] the signal at this point based on the surrounding points. This reduces the peaks of our resonant frequencies and is not ideal. To prevent this, we must ensure optimal signal strength.

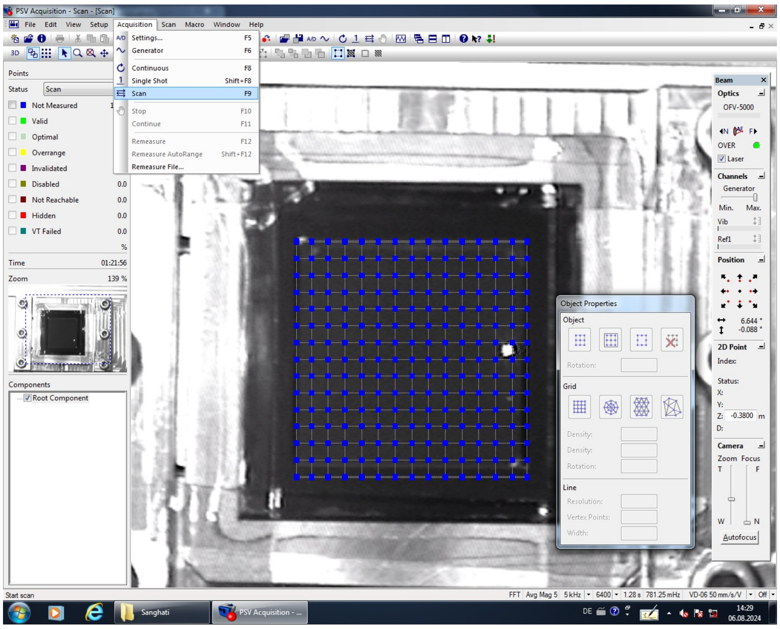

Figure B.25: Scan for measurements

C

Appendix C : Height measurement through MATLAB

Height measurement: The DHM is a powerful technique for obtaining high-resolution, three-dimensional topographic measurements of samples. However, it cannot give us a 3D representation of the z-axis heights. This MATLAB script automates the process of converting phase images into height displacement maps and visualizes the data. The key steps include parameter initialization, phase image loading, phase-to-height conversion, phase unwrapping, and result visualization.

```

clear
clc

% Parameters
wavelength_nm = 665.5651; % Wavelength of the light in nanometers
n = 1; % refractive index of air

%hange thisC
numFiles = 25; % Number of files in the sequence
folder = "D:\MATLAB\Thesis work\Data\Phase_img_July\";
binning_factor = 4;

% Loop over each file
for k = 0:numFiles-1
    disp("k = "+k+": Start")
    % Generate filename
    filename = folder + sprintf('Phase%05d.tif', k);%Check this

    % Load the image file
    phase_nm = imread(filename);

    % Downsize the image
    phase_nm = phase_nm(1:7268,1:7268);%Change this..multiple of 4
    desired_size = [size(phase_nm,1)/4, size(phase_nm,2)/4];
    phase_nm_resized = imresize(phase_nm, desired_size);

    if k==0
        height_stack = zeros(size(phase_nm_resized,1), size(phase_nm_resized,2),
           numFiles);
    end

    % Convert phase from nanometers to radian
    phase_radian = 2*pi*double(phase_nm_resized) / wavelength_nm;
```

```

    % Unwrap the phase
    phase_unwrapped = phase_radian; %in radian

    % Calculate height displacement from phase
    height = (wavelength_nm / (4 * pi * n)) * phase_unwrapped;    %in nm

    height_stack(:, :, k+1) = height;

end

%% Visualize the unwrapped phase


% % Select the slice index to plot
% slice_index = 11; % You can change this to any index from 1 to 46
%
% % Extract the slice from the height_stack
% slice_data = height_stack(:, :, slice_index);
%
% % Create a figure
% figure;
% imagesc(slice_data);
% colorbar;
% xlabel('X-axis');
% ylabel('Y-axis');
% title(['Height Map for Slice ', num2str(slice_index)]);
% axis equal;
% axis tight;




%%
min_height = min(height_stack(:));
max_height = max(height_stack(:));

% Create a video writer object
timestamp = datestr(now, 'yyyymmdd_HHMMSS');
baseFilename = 'height_video';
videoFileName = [baseFilename, '_', timestamp, '.mp4'];

v = VideoWriter(videoFileName, 'MPEG-4');
v.FrameRate = 5; % Adjust frame rate as needed
open(v);

% Create a video from the height_stack
figure;
for k = 1:numFiles
    imagesc(height_stack(:, :, k), [min_height, max_height]);
    colorbar;
    xlabel('X-axis');
    ylabel('Y-axis');
    title(['Height Map for Frame ', num2str(k)]);
    axis equal;
    axis tight;

    % Capture the plot as a frame
    frame = getframe(gcf);
    writeVideo(v, frame);
end
```

```
% Close the video writer object
close(v);

disp(['Video saved as ', videoFileName]);



% % Plot a 3D visualization of one slice
% slice_index = 1; % Change this to visualize a different slice
% slice_data = height_stack(:, :, slice_index);
%
% % Create meshgrid for X and Y coordinates
% [x, y] = meshgrid(1:size(slice_data, 2), 1:size(slice_data, 1));
%
% % Create a 3D surface plot
% figure;
% surf(x, y, slice_data);
% shading interp; % Smooth the colors
% colorbar;
% xlabel('X-axis');
% ylabel('Y-axis');
% zlabel('Height (nm)');
% title(['3D Height Map for Slice ', num2str(slice_index)]);
```

Listing C.1: MATLAB Script for Converting Phase Images to Height Maps

All in all, we see that this MATLAB script automates the processing of phase images obtained from the DHM, converting them into height displacement maps. The script takes the unwrapped phase image, performs height calculation, and visualizes the results both as static images and as a video sequence. The processed height maps and visualizations provide a comprehensive analysis of the sample's topography as captured through the DHM technique.

D

Appendix D: Equations of motion for mode shape calculation and Parametric analysis of material properties

Equation of motion:

The displacement fields $u(x, y, t)$ and $v(x, y, t)$ in the x and y directions are described by the following equations of motion:

$$\rho \frac{\partial^2 u}{\partial t^2} = \frac{\partial \sigma_{xx}}{\partial x} + \frac{\partial \tau_{xy}}{\partial y} \tag{D.1}$$

$$\rho \frac{\partial^2 v}{\partial t^2} = \frac{\partial \tau_{xy}}{\partial x} + \frac{\partial \sigma_{yy}}{\partial y} \tag{D.2}$$

Stress-Strain Relationships:

The stress components σ_{xx}, σ_{yy}, and τ_{xy} are related to the strain components ϵ_{xx}, ϵ_{yy}, and γ_{xy} through Young's modulus (E) and Poisson's ratio (ν):

$$\sigma_{xx} = \frac{E}{1-\nu^2} \left(\epsilon_{xx} + \nu \epsilon_{yy}\right) \tag{D.3}$$

$$\sigma_{yy} = \frac{E}{1-\nu^2} \left(\epsilon_{yy} + \nu \epsilon_{xx}\right) \tag{D.4}$$

$$\tau_{xy} = \frac{E}{2(1+\nu)} \gamma_{xy} \tag{D.5}$$

Strain-Displacement Relationships:

The strain components ϵ_{xx}, ϵ_{yy}, and γ_{xy} are related to the displacement fields u and v:

$$\epsilon_{xx} = \frac{\partial u}{\partial x} \tag{D.6}$$

$$\epsilon_{yy} = \frac{\partial v}{\partial y} \tag{D.7}$$

$$\gamma_{xy} = \frac{\partial u}{\partial y} + \frac{\partial v}{\partial x} \tag{D.8}$$

Combined Equations:

Combining these relationships, we obtain the full set of equations used by COMSOL for mode shape calculations:

$$\rho\frac{\partial^2 u}{\partial t^2} = \frac{\partial}{\partial x}\left(\frac{E}{1-\nu^2}\left(\frac{\partial u}{\partial x} + \nu\frac{\partial v}{\partial y}\right)\right) + \frac{\partial}{\partial y}\left(\frac{E}{2(1+\nu)}\left(\frac{\partial u}{\partial y} + \frac{\partial v}{\partial x}\right)\right) \tag{D.9}$$

$$\rho\frac{\partial^2 v}{\partial t^2} = \frac{\partial}{\partial y}\left(\frac{E}{1-\nu^2}\left(\frac{\partial v}{\partial y} + \nu\frac{\partial u}{\partial x}\right)\right) + \frac{\partial}{\partial x}\left(\frac{E}{2(1+\nu)}\left(\frac{\partial u}{\partial y} + \frac{\partial v}{\partial x}\right)\right) \tag{D.10}$$

These equations allow COMSOL to accurately calculate the mode shapes and natural frequencies of the membrane by solving for the displacement fields u and v, given the material properties and the geometry of the membrane.

D.1. Parametric analysis

Here we investigate the effect of the material properties of membrane material Si_3N_4 in themselves:

1. **Changing pre-stress to twice its value:** the frequencies scale according to Eqn F.1.

2. **Changing E to twice its value:** the frequencies and mode shapes do not change.

In the context of a membrane under tension, the eigenfrequencies primarily depend on the tension in the membrane and the mass per unit area, rather than directly on Young's modulus (E). The tension in the membrane is often due to an applied pre-stress or inherent stress from the manufacturing process.

The eigenfrequency f for a membrane is given by:

$$f \propto \sqrt{\frac{T}{\rho}} \tag{D.11}$$

where T is the tension per unit length, and ρ is the density of the material.

Therefore, doubling E does not affect the eigenfrequencies because the tension T is assumed to be independent of E in the membrane model.

Even though the tension and density primarily determine the eigenfrequencies, COMSOL requires Young's modulus (E) to define the material properties and ensure accurate numerical computations fully.

3. **Changing ρ (density) to twice its value:** the frequencies scale according to Eqn F.1

4. **Changing ν (Poisson's ratio) to twice its value:** COMSOL gives me an error: division by 0.

This suggests that the modified value is causing a division by zero in the expression for the stiffness matrix component D_{11}. For isotropic materials, components of the stiffness matrix D (used in plane stress conditions) are given by:

$$D_{11} = \frac{E(1-\nu)}{(1+\nu)(1-2\nu)}$$

Our initial value of (ν) was 0.25, doubling which we get 0.5. When doubled and subtracted from 1, this in the denominator gives zero, explaining our error code.

Since we violated the range for the Poisson's ratio and also picked a singularity, this was a limiting case. To fix this, we picked an arbitrary value of 0.45 and we found that the eigenfrequencies and mode shapes remained unchanged.

The Poisson's ratio primarily influences the material's deformation characteristics under stress but has a secondary effect on the stiffness-to-mass ratio that governs the eigenfrequencies. It affects the coupling between the strains in orthogonal directions, but this coupling does not significantly alter the fundamental stiffness or inertial properties that determine the eigenfrequencies.

E

Appendix E: Understanding Meshing

The original mesh in the image featured a uniform distribution of triangular elements, which enhanced consistency in results, particularly under symmetric or uniform loading and boundary conditions. Its symmetry facilitated simpler analysis and interpretation by leading to symmetric mode shapes, while also enhancing accuracy and convergence for symmetric geometries and loadings. This could cause certain modes to repeat or double, reflecting the inherent physical and geometric symmetry of the analyzed problem.

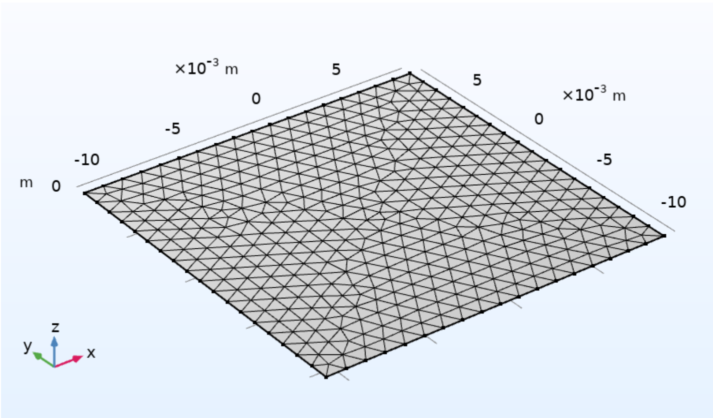

Figure E.1: The mesh

However, the profile was only C0 smooth in our case. However, we needed to increase the refinement of our mesh was seemed already necessary as the von Mises stress was not smooth for higher frequencies.

In finite element analysis (FEA), C^0 meshing refers to a type of meshing where the displacement field is continuous across element boundaries, but the derivatives of the displacement (strains) may not be continuous. This means that while the elements share common nodes and the displacement is smooth, the strain and stress values can exhibit discontinuities at the element interfaces.

The primary challenge with C^0 meshing is that the discontinuities in the strain and stress fields can lead to inaccuracies in stress calculations, particularly in regions with high-stress gradients. This can affect the precision of the computed von Mises stress, which is a critical measure of the yield criterion in materials.

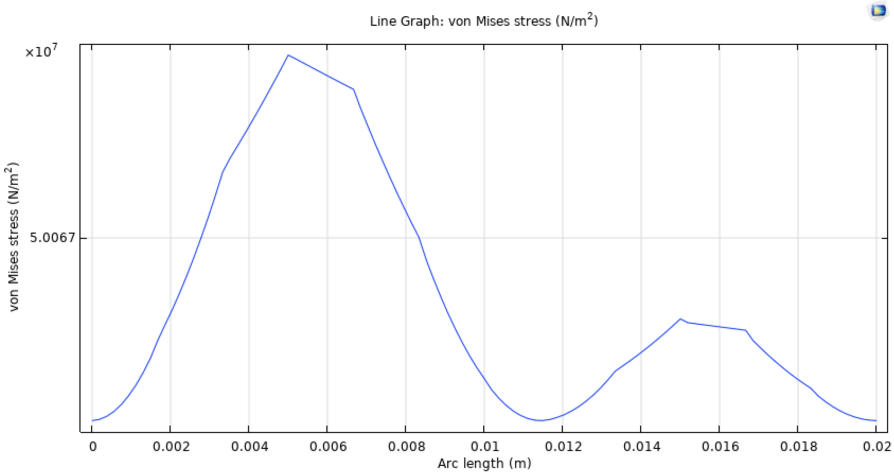

Figure E.2: Meshing while using 'finer' elements

One effective way to mitigate the issues associated with C^0 meshing is by using finer meshing elements. Here's how finer meshing elements help:

- **Increased Resolution**: Finer meshes increase the resolution of the model, providing a more detailed representation of the geometry and better capturing the stress gradients.
- **Reduced Discontinuities**: By decreasing the element size, the discontinuities in the strain and stress fields are reduced, leading to smoother and more accurate stress distributions.
- **Enhanced Accuracy**: Finer meshes result in more accurate numerical solutions, improving the precision of von Mises stress calculations and other derived quantities.

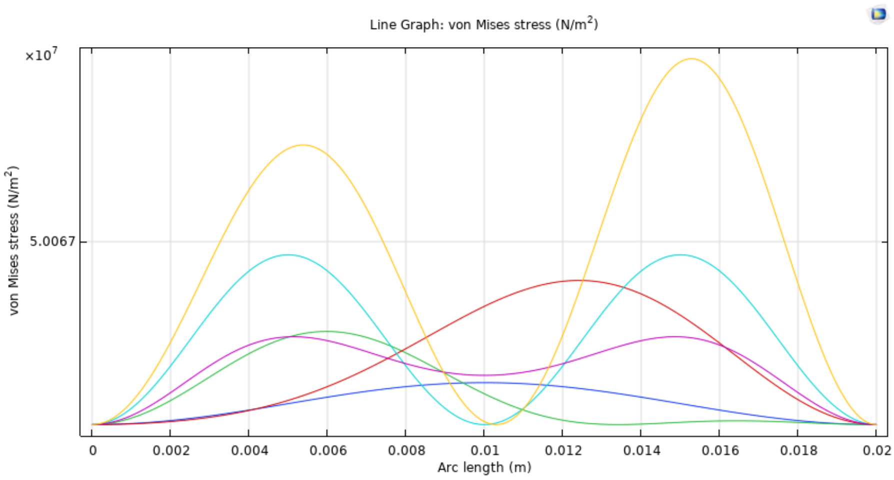

Figure E.3: Meshing while using 'extremely fine' elements

Impact on Von Mises stress based on poor meshing techniques:

- **Impact of C^0 Meshing**: The discontinuities in the strain and stress fields caused by C^0 meshing can lead to inaccuracies in the calculation of principal stresses, and consequently, in the von Mises stress.
- **Improvement with Finer Mesh**: Finer meshing elements reduce these discontinuities, providing a more accurate representation of the stress fields. This leads to more reliable von Mises stress calculations, which are crucial for assessing material failure and safety.

F

Appendix F: Material Properties, Solid Mechanics Model and Gold Layer

Properties of Si_3N_4 and SiC:

Parameter	Value
E_1	3.10×10^{11} Pa
ρ_1	3.195×10^3 kg/m^3
ν_1	0.25

Similarly, the values of SiC were:

Parameter	Value
E_1	2.23×10^{11} Pa
ρ_1	2.83×10^3 kg/m^3
ν_1	0.203

And for kapton tape:

Parameter	Value
E_1	2.5×10^8 Pa
ρ_1	0.925×10^3 kg/m^3
ν_1	0.45

The formula for frequency provided in Blevin's formulation [37] was:

$$\begin{aligned} f_{ij} &= \frac{\lambda_{ij}}{2}\sqrt{\frac{S}{\gamma A}}, \\ \lambda_{ij} &= \sqrt{i^2\frac{b}{a} + j^2\frac{a}{b}} \end{aligned} \tag{F.1}$$

Here, a and b are the side lengths, A is the surface area, S is the tension per unit edge, and γ is the mass per unit area.

We can see that $f_{i,j}$ scales with $\sqrt{\frac{S}{\gamma}}$ and $\sqrt{\frac{i^2 b}{a} + \frac{j^2 a}{b}}$ for a fixed geometry and the same surface area.

From this equation can derive the fundamental frequency $f_{i,j}$ for a square membrane as:

$$f_{i,j} = \frac{1}{2a}\sqrt{\frac{\sigma}{\rho}}\sqrt{i^2 + j^2}$$

For the case of the membrane, with $a = 20$ mm, $T = 50$ N/m, and $t = 500$ nm, the stress σ as verified in Figure 4.6, was:

$$\sigma = \frac{T}{t} = \frac{50}{500 \times 10^{-9}} = 10^8 \text{ N/m}^2$$

Thus, the normalized resonance frequency $\frac{f_{i,j}}{\sqrt{\frac{i^2 b}{a} + \frac{j^2 a}{b}}}$ as plotted as a function of $\sqrt{\frac{S}{\gamma}}$ for different materials with the same geometry, should result in a straight line.

- **Silicon Nitride (Si_3N_4)**:

$$\sqrt{\frac{\sigma}{\rho}} = \sqrt{\frac{10^8}{3.195 \times 10^3}} \approx 176.84$$

$$\text{Normalized } f_{1,1} = \frac{6258}{\sqrt{2}} \approx 4424 \text{ Hz}$$

- **Silicon Carbide (SiC)**:

$$\sqrt{\frac{\sigma}{\rho}} = \sqrt{\frac{10^8}{2.83 \times 10^3}} \approx 187.97$$

$$\text{Normalized } f_{1,1} = \frac{6647}{\sqrt{2}} \approx 4701 \text{ Hz}$$

- **Kapton**:

$$\sqrt{\frac{\sigma}{\rho}} = \sqrt{\frac{10^8}{925}} \approx 328.81$$

$$\text{Normalized } f_{1,1} = \frac{11618}{\sqrt{2}} \approx 8216 \text{ Hz}$$

On plotting these values, the resulting linear equation is:

$$y = 24.954x + 10.696$$

This equation follows the standard form of a straight-line equation, confirming the linear relationship expected from the theoretical model.

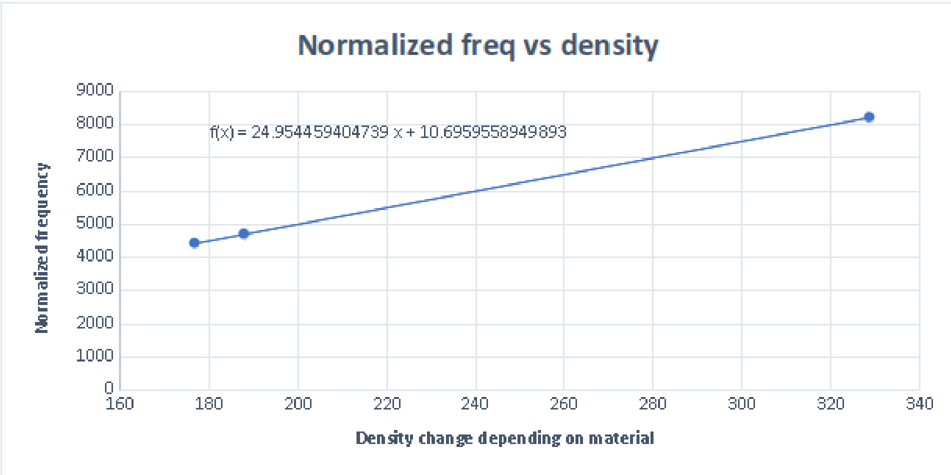

Figure F.1: Normalized resonance frequency $\frac{f_{i,j}}{\sqrt{i^2 \frac{b}{a} + j^2 \frac{a}{b}}}$ vs $\sqrt{\frac{\sigma}{\rho}}$

This outcome illustrates that the normalized resonance frequencies for different materials align with theoretical predictions.

F.1. Comparison with Solid Mechanics Model

44.067
45.467
45.946
47.690
49.676

Table F.1: The eigenfrequencies in the solid mechanics model

Since we have a lot of options within the COMSOL environment to try and simulate eigenfrequencies, we attempted to simulate the same membrane under similar boundary conditions using the solid mechanics module. However, the results were inconsistent with those obtained from the membrane module and did not adhere to the theoretical expectations of Eqn F.1. This discrepancy arises due to several complexities inherent in the solid mechanics model:

Complexities in Solid Mechanics Model

- **Density:** The solid mechanics model considers the material's full density which is significantly higher than that used in the membrane model. In this simplification, the model uses an effective density that only accounts for the mass per unit area (surface density in the membrane) rather than the mass per unit volume (volumetric density in solid mechanics).
- **Elastic Moduli:** Unlike the membrane model, the solid mechanics model incorporates the complete set of elastic properties, including Young's modulus and Poisson's ratio (in bending, twisting, and compressive forces), which influence the material's stiffness and its response to applied forces.
- **Geometry:** The eigenfrequencies in the solid mechanics model are influenced by the entire 3D geometry of the structure, not just its thickness. This includes the shape and size in all three dimensions. Also, boundary conditions are more complex, as they can include constraints on movement in all three dimensions and moments (torques), impacting the vibrational characteristics.
- **Bending Stiffness and Shear Deformation:** These are considered in the solid mechanics model but ignored in the membrane model, leading to differences in vibrational behaviour.
- **Higher Order Effects:** Solid mechanics captures more complex effects such as material anisotropy and inhomogeneities, which are not considered in the membrane model.

Mode Shape and Frequency Differences

- **Different Modes:** The membrane model uses a pre-stress parameter T_0 to adjust the stress to 100 [MPa] for 2D interfaces. However, for a 3D interface, the required stress is 100 [MPa], leading to a significant difference in the applied stress. COMSOL Multiphysics cannot convert this difference accurately, as there is no objective conversion from N/m to N/m^2. Instead, it gives us a warning, assumes we made a mistake with the units and just uses the value itself. This results in different mode shapes.
- **Different Frequencies:** The density of the material in the solid mechanics model is ten times higher than that in the membrane model (surface density vs volumetric density), which lowers the eigenfrequencies. This discrepancy can be adjusted in the model to achieve consistency between the physics interfaces.

Numerical Considerations In theory, the solid mechanics module should be able to model the same systems as the membrane module. However, due to computational limitations, certain simplifications are necessary to achieve practical results. For example, achieving a fine mesh in the z-direction for accurate results in solid mechanics is computationally intensive. The provided model, though quickly assembled, demonstrates that solid mechanics simulations take significantly longer (a couple of minutes) compared to the membrane model (less than 5 seconds).

Computational Complexity The complexity of this case arises from the thickness-to-length ratio thic$/L \ll 1$. For such cases, the membrane interface is designed to avoid meshing issues and reduce computational time. Ideally, in a 3D model, elements should consist of multiple equal-length lines. For instance, if five elements are required in the z-direction, the x- and y-direction meshes must accommodate $L/(\text{thic}/5)$ elements, increasing computational demand.

While solid mechanics provides a more comprehensive model by accounting for full 3D behaviour and complex material properties, the membrane model offers computational efficiency with acceptable simplifications for thin structures. The choice of model depends on the balance between accuracy and computational resources available.

F.2. Gold layer assumptions

The observed pattern in the eigenfrequency change in the graphs in section 4 as the system is cooled down can be attributed to several factors:

1. **Thermal Contraction and Stress Build-Up**: As the temperature decreases, both Si_3N_4 and gold undergo thermal contraction. However, they have different coefficients of thermal expansion (CTE). Si_3N_4 typically has a lower CTE compared to gold, meaning it contracts less than gold when cooled. This difference in contraction creates additional tensile stress in the membrane as the temperature decreases. Initially, this increase in tensile stress leads to an increase in the eigenfrequency, as seen in the upward trend in the plot.
2. **Stress Saturation**: At a certain point, the material may reach a state where the additional stress no longer contributes significantly to the increase in eigenfrequency. This could be due to the membrane reaching a stress limit or because the differential contraction between the two materials starts to stabilize. This would explain the plateau observed in the middle of the graph, where the eigenfrequency remains relatively constant over a range of temperatures.
3. **Interfacial Effects and Imperfections**: The interface between the Si_3N_4 membrane and the gold layer could also play a role. Any imperfections or mismatches in the bonding between the two layers could become more pronounced at lower temperatures, potentially leading to a decrease in the overall structural integrity and hence a decrease in eigenfrequency.
4. **Residual Stresses and Cracking**: If residual stresses or microcracks are introduced during cooling, particularly at the interface or within the gold layer due to its higher CTE, this could lead to a reduction in stiffness and hence a decrease in eigenfrequency at very low temperatures.